Solid State Amorphization Reactions In Thin Film Diffusion Couples

Thesis by

Wen Jin Meng

In Partial Fulfillment of the Requirements

for the Degree of

Doctor of Philosophy

California Institute of Technology

Pasadena, California

1988

Submitted January 7, 1988

© 1988

Wen Jin Meng

All Rights Reserved

To my grandfather

Acknowledgements

My foremost gratitude goes to Professor W. L. Johnson. Bill's keen physical insights and vivid imaginations have provided much inspiration for the work performed in this thesis. I have learned through Bill that good science, after all, can be fun.

I have learned a great deal through interactions with many people. Dr. K. M. Unruh's expertise has helped me tremendously during the construction of our sputter-deposition system. I am deeply indebted to Drs. C. W. Nieh and C. Ahn for initiating me into the science, and often art, of electron microscopy. Interactions with Dr. B. Fultz has been most fruitful, and my special thanks goes to him for a critical reading of my thesis. Dr. E. J. Cotts taught me much of what to do and what not to do.

I would like to thank the members of "the group", past and present, including Dr. D. V. Baxter, Dr. M. Atzmon, Dr. X. L. Yeh, Dr. Y. T. Cheng, Dr. S. M. Anlage, P. Askenazy, P. Yvon, D. S. Lee, C. Krill, Zezhong Fu and Dr. H. Fecht for making my years here a memorable experience.

I would like to thank C. Geremia and J. Ferrante for their help and friendship. Without them, the memories of our group would be incomplete. Technical assistance by C. Garland is gratefully acknowledged.

My love goes out to Mei. The many sleepless nights she shared with me formed an inseparable part of this thesis. My love goes out to my familly, their love has always been with me.

Financial support for this work has been provided by the Department of Energy and the National Science Foundation.

Abstract

Metastable materials including amorphous materials have traditionally been synthesized from either the vapor or the liquid state. Very recently, it has been demonstrated that an amorphous alloy can be obtained by interdiffusion reactions in crystalline binary thin-film diffusion couples. This thesis focuses its study on the formation of amorphous alloys and the subsequent formation of crystalline compounds in thin-film diffusion couples. Both the thermodynamics and kinetics of amorphous phase formation have been examined. The evolution of these diffusion couples has been followed in some detail. Relevant factors governing the evolution of diffusion couples in general will be discussed.

Table of Contents

Acknowledgements iv

Abstract v

List of Tables viii

List of Figures ix

Chapter 1 Introduction 1

1.1 Diffusion in the Solid State 2

1.2 Interdiffusion and Reactions in Thin Films 9

1.3 Metastable Phases 13

1.4 Solid State Amorphization 23

1.5 Introduction to the Thesis 25

1.6 References 28

Chapter 2 High Vacuum Sputter Deposition of Thin Films 34

2.1 Introduction to Sputter Deposition 35

2.2 Vacuum System 39

2.3 Sputter Deposition: Operation and Monitoring 45

2.4 Summary 54

2.5 References 55

Chapter 3 Solid-State Amorphization of Planar Binary Diffusion Couples: Thermodynamics and Growth Kinetics 57

3.1 Equilibrium Phase Diagrams and Free Energy Diagrams 57

3.2 Planar Growth Kinetics of a Single Compound Interlayer 58

3.3 Growth of the Amorphous Interlayer: X-ray and Resistivity Measurements 64

3.4 Differential Scanning Calorimetry 73

3.5 Summary 96

3.6 References 97

Chapter 4 Evolution of Planar Binary Diffusion Couples 100

4.1 Specimen Preparation 100

4.2 How Thick Can Amorphous Interlayers Grow 105

4.3 Is Nucleation Important 113

4.4 Models for Evolution of Diffusion Couples 121

4.5 Summary 127

4.6 References 129

Conclusion 130

List of Tables

Table 2.1 Residual gas content in the sputtering chamber as sampled by the residual gas analyzer. Residual gas contents after introducing Ar into the chamber are monitored both before and during sputtering of a pure Ti target at 6 mTorr of Ar.

Table 2.2 Low pressure properties of air. Particle density, n, mean-free path, λ; particle flux on a surface, Γ. $T = 22°C$. Taken from Ref. 14.

List of Figures

Fig. 1.1 Schematic illustration of the Kirkendall effect. Taken from Ref. 15.

Fig. 1.2 Hypothetical free energy diagram and the associated phase diagram of a binary system (A-B) with a positive enthalpy of mixing.

Fig. 1.3 Schematic Time-Temperature-Transformation (TTT) diagram for crystal growth in an undercooled melt. Taken from Ref. 54.

Fig. 2.1 Schematic representation of the plasma during planar diode sputtering. Taken from Ref. 11.

Fig. 2.2 Configuration of circular and rectangular planar magnetron sputtering guns. Taken from Ref. 11.

Fig. 2.3 Vacuum system block diagram: (1) N_2 flush inlet valve; (2) pressure relief valve; (3) gate valve; (4) throttle valve; (5) chamber vent valve; (6) piezoelectric leak valve; (7) ion gauge; (8) chamber isolation/differential leak valve; (9) residual gas analyzer; (10) ion gauge; (11) turbo-pump vent valve; (12) mechanical pump isolation valve; (13) thermocouple gauge; (14) mechanical pump.

Fig. 2.4 Cryogenic pump regeneration history as monitored by the low temperature sorption stage temperature during cooling.

Fig. 2.5 Typical current-voltage characteristics of planar magnetron sputter guns while sputtering Cu at 6 mTorr of Ar.

Fig. 2.6 Deposition rate of pure Cu at 9 mTorr of Ar vs. cathode current.

Fig. 2.7 X-ray small angle scattering from an Fe/V multilayer with nominal composition modulation wavelength of 40Å.

Fig. 3.1 Free energy functions of various phases and the A-B phase diagram derived from them. Taken from Ref. 1.

Fig. 3.2 Schematic illustration of growth of a single compound interlayer in a planar binary diffusion couple. Hypothetical free energy diagram and the concentration profile.

Fig. 3.3 X-ray diffraction patterns of as- deposited (top) and reacted (bottom) Ni/Zr multilayers (see text).

Fig. 3.4 Normalized Ni and Zr integrated Bragg peak intensities vs. $t^{1/2}$ at 250°C and 315°C (see text).

Fig. 3.5 Shift of Zr Bragg peaks as a function of reaction time at 250°C.

Fig. 3.6 d-spacings of Ni (111), Zr (002), and Zr (100) Bragg peaks as a function of reaction time at 250°C in reflection geometry. The insert shows the Zr (100) d-spacing as a function of reaction time in both reflection (R) and transmission (T) (see text).

Fig. 3.7 Resistance of a Ni/Zr multilayer (top) vs. reaction time at 225°C. Shown also is the resistance of a pure Ni film (bottom) vs. time under identical experimental settings (see text).

Fig. 3.8 Schematic illustrations of various thermal analysis systems. Taken from Ref. 21.

Fig. 3.9 Melting endotherm of pure Pb (4N+) at 10 K/min taken on a Perkin-Elmer DSC-4.

Fig. 3.10 Apparent melting temperature of pure Pb (4N+) vs. DSC heating rate.

Fig. 3.11 Geometry of Ni/Zr multilayered diffusion couples.

Fig. 3.12 Measured heat flow rate as a function of temperature for a sputtered Ni/Zr multilayer, $l_{Ni} = l_{Zr} = 300$Å, average stoichiometry $Ni_{68}Zr_{32}$.

Fig. 3.13 X-ray diffraction patterns for the thin film sample of Fig. 3.12, see text.

Fig. 3.14 Measured heat flow rate as a function of temperature for Ni/Zr multilayers with varying individual layer thicknesses. Dotted curve, $l = 300$Å; dashed

curve, l = 450Å; solid curve, l = 1000Å.

Fig. 3.15 Heat-flow rate as a function of temperature normalized to the total interfacial area of the respective Ni/Zr multilayers in Fig. 3.14.

Fig. 3.16 Heat-flow rate normalized by the total Ni/Zr interfacial area of multilayers of various individual layer thicknesses and average compositions. Dotted line, $l_{Ni} = 300\AA/l_{Zr} = 450\AA$; dashed line, $l_{Ni} = 500\AA/l_{Zr} = 800\AA$; solid line, $l_{Ni} = l_{Zr} = 1000\AA$.

Fig. 3.17 Arrhenius plot for the determination of the activation energy and pre-exponential factor of the interdiffusion constant (see text).

Fig. 3.18 Heat-flow rate vs. temperature for sputtered Ni/Zr multilayers of two different average compositions: (a) $Ni_{59}Zr_{41}$, (b) $Ni_{68}Zr_{32}$ (see text).

Fig. 3.19 Heat-flow rate vs. temperature of Ni/Zr multilayers with various Zr layer thicknesses: (a) $l_{Zr} = 800\AA$, (b) $l_{Zr} = 450\AA$, (c) $l_{Zr} = 240\AA$. Average composition $\sim Ni_{58}Zr_{42}$ for all three samples.

Fig. 4.1 Schematic of the morphology of bilayered elemental Ni/Zr diffusion couples where one element (Ni or Zr) is sputtered polycrystals and the other (Zr or Ni) consists of a mosaic of large single crystals on the order of 10 μm in size.

Fig. 4.2 XTEM bright-field micrograph of a Ni/Zr multilayered thin-film annealed briefly around 150°C (see text).

Fig. 4.3 XTEM bright-field micrograph of a Ni/Zr multilayered thin-film annealed at 320°C for 8 hours. Both amorphous and compound interlayers are clearly evident. Amorphous interlayers are close to 1000Å in thickness.

Fig. 4.4 XTEM of a Ni/Zr diffusion couple reacted at 300°C: (a) for 6 hours; (b) for 18 hours. This diffusion couple is of the bilayered s-Ni/poly-Zr type (see Section 4.3).

Fig. 4.5 XTEM bright-field micrographs of a sputtered Ni/Zr multilayered thin-

film annealed at 360°C: (a) for 10 min; (b) for 45 min. Backgrowth of the compound into the amorphous material at 45 min is clearly evident.

Fig. 4.6 Plot of the critical thickness of the amorphous NiZr interlayer vs. reaction temperature.

Fig. 4.7 Reaction of a poly-Ni/s-Zr bilayer diffusion couple: (a) typical microstructure of recrystallized Zr foil; (b) bright-field micrograph showing no reaction after annealing at 300°C for 6 hours; (c) high-resolution micrograph of the poly-Ni/s-Zr interface, showing the Ni (111) ande Zr (101) lattice fringes.

Fig. 4.8 Plane-view, bright-field micrograph showing a poly-Ni/s-Zr diffusion couple after annealing at around 250°C for 4 hours. No reaction is observed at Zr grain boundaries.

Fig. 4.9 XTEM bright-field micrograph of a s- Ni/poly-Zr bilayered diffusion couple annealed at 300° for 6 hours. An amorphous NiZr interlayer around 1000Å thick formed as a result of the reaction.

Fig. 4.10 Hypothetical concentration profile in a A-B diffusion couple during parallel growth of two compound interlayers β and γ (see text).

Chapter 1

Introduction

Thin films of solids were first obtained by either evaporation or cathode sputtering roughly around 1850[1,2]. Many more years passed during which thin solid films remained a mere laboratory curiosity. Early studies were primarily concerned with the physical mechanisms governing processes such as evaporation from liquid and solid surfaces[3,4] or sputtering of the cathode material in a glow discharge[5]. The science and technology of thin solid films have advanced together with vacuum technology, which enabled the preparation of thin films of controlled purity and microstructure. The use of thin films in magnetic or superconducting devices[6] and, perhaps most importantly, in very large-scale intergrated circuits (VLSI), and the technological demands associated with such usages, have been primarily responsible for the tremendus progress in both fields in the last thirty years.

This thesis focuses on the study of solid-state diffusive phase transformations in planar thin film diffusion couples. It will be demonstrated that, under suitable manipulation of thermodynamic and kinetic constraining factors, the interdiffusion reaction between two crystalline elemental layers may result in the formation of a metastable amorphous phase instead of equilibrium crystalline compounds. Through detailed examination of such solid-state interdiffusion reactions that lead to the formation of metastable phases, new insights into the fundamental processes governing solid-state diffusive phase transformations in thin films can

be gained. This chapter is organized as follows. In Section 1.1, a brief review of some basic notions on diffusion in the solid state will be given. In Section 1.2, we attempt to categorize the wealth of experimental results available on interdiffusion reactions in thin film diffusion couples, some unifying features of such interdiffusion reactions common to many systems will be delineated. In Section 1.3, we survey our knowledge of metastable phases in general, with emphasis placed on the various techniques for their synthesis. In Section 1.4, we give an introduction to solid-state amorphization reactions. Finally, in Section 1.5, some necessary background information together with a brief introduction to this thesis will be given.

1.1 Diffusion in the Solid State

Diffusion in the solid state was first analyzed quantitatively by Fick[7]. By noting the similarity between mass transfer by diffusion and heat transfer by conduction, Fick's first law was formulated analogous to Fourier's law of heat conduction

$$J = -D\frac{\partial C}{\partial x}, \tag{1}$$

where if the concentration C denotes the number of atoms per cm^3 and the current J the number of atoms per cm^2 per sec, then the diffusion constant D is given in the units of cm^2/sec. Equation (1) relates the mass flux to the gradient in concentration in one dimension. Combined with the condition for mass conservation, we arrive at Fick's second law

$$\frac{\partial C}{\partial t} = \frac{\partial}{\partial x}(D\frac{\partial C}{\partial x}). \tag{2}$$

In the special case when D is a constant, Equation (3) reduces to

$$\frac{\partial C}{\partial t} = D\frac{\partial^2 C}{\partial x^2}. \tag{3}$$

Many analytical and numerical solutions of Equation (3) subjected to different boundary and initial conditions exist and solutions C(x,t) are compared with experimentally determined concentration profiles to extract the diffusion constant D[8].

Diffusion in the solid state is a complex problem. Various diffusion constants can be defined according to different physical situations. *Self-diffusion* refers to mass transport in homogeneous materials without the influence of a concentration gradient. Experimentally, such situations are often realized by means of radioactive *tracer diffusion* in an otherwise homogeneous material[9]. Self-diffusion in pure metals is one of the most studied and best understood examples of diffusion in the solid state[10]. One often models the process of diffusion by assuming that the path followed by each atom during diffusion is adequately described as a random walk. Denote by $P_\tau(x)$ the normalized probability that an atom at the origin at time zero will be at position x at time τ. Then given an initial concentration profile $C(x,0)$ at time zero, the concentration profile at time τ will be obtained by

$$C(x',\tau) = \int_{-\infty}^{+\infty} C(x,0)P_\tau(x'-x)dx. \tag{4}$$

Expanding the left-hand side of Equation (4) in powers of τ and the right-hand side in powers of $X = x - x'$, and noting that for a true random walk $P_\tau(x) = P_\tau(-x)$, we then obtain

$$\frac{\partial C}{\partial t} = \frac{\langle x^2\rangle}{2\tau}\frac{\partial^2 C}{\partial x^2}, \tag{5}$$

where

$$\langle x^2\rangle = \int_{-\infty}^{+\infty} x^2 P_\tau(x)dx. \tag{6}$$

Compareing Equation (5) to (3), we obtain

$$D = \frac{\langle x^2 \rangle}{2\tau}. \tag{7}$$

In an isotropic crystal, $\langle x^2 \rangle = \langle y^2 \rangle = \langle z^2 \rangle$ and $\langle R^2 \rangle = 3\langle x^2 \rangle$. If a total of N jumps takes place in time τ, and each jump is of the same length r, then

$$\langle R^2 \rangle = \langle (\sum^{N} r_i)^2 \rangle = N r^2 f, \tag{8}$$

where $r^2 = \langle r_i^2 \rangle$ and $f = 1 + 2(\langle \cos\theta_1 \rangle + \langle \cos\theta_2 \rangle + \cdots)$. The average of the cosines expresses the correlation between the angle of successive diffusive jumps. Note that the total number of jumps N in time τ is τ times the jump frequency Γ; we can thus rewrite Equation (7) as

$$D = \frac{1}{6} r^2 f \Gamma. \tag{9}$$

It is important to inquire into the atomic mechanisms that lead to the diffusion. In a pure element, atoms can diffuse interstitially without the assistance of any particular type of defect. In this case, the diffusion process approximates a true random walk and the correlation factor f is one. If a particular type of defect, such as a vacancy in a crystal, is needed to assist a diffusive atomic jump, then correlation effects will always arise[11].

For diffusion by a single defect mechanism in a pure element, the diffusive jump frequency Γ is simply the coordination number Z times a product of the fractional defect concentration F and the defect jump frequency w. Simple thermodynamics predicts that the equilibrium concentration of a particular defect i is related to the enthalpy ΔH_i^f and excess entropy ΔS_i^f of formation of this defect by[12]

$$F_i = exp[-\frac{\Delta H_i^f - T\Delta S_i^f}{k_B T}]. \tag{10}$$

The defect jump frequency w is usually calculated by means of Eyring's reaction rate theory as

$$w = \nu exp[-\frac{\Delta H_i^m - T\Delta S_i^m}{k_B T}], \tag{11}$$

where ν is the atomic vibration frequency and $\Delta H_i^m - T\Delta S_i^m$ is the activation free energy of migration via this particular defect[13]. Thus, an expression for the self-diffusion coefficient for diffusion by a particular defect mechanism i can be written as

$$D = \frac{1}{6} Z r^2 \nu f exp[\frac{\Delta S_i^f + \Delta S_i^m}{k_B}] exp[-\frac{\Delta H_i^f + \Delta H_i^m}{k_B T}]. \tag{12}$$

The diffusion coefficient can therefore be expressed in an Arrhenius form

$$D = D_o exp[-\frac{Q}{K_B T}]. \tag{13}$$

When several defect mechanisms are contributing simultaneously to the diffusion process, the diffusion coefficient is then composed of a sum of several terms with similar form but with different activation energies. Because of the exponential dependence of the diffusion coefficient, one mechanism usually dominates the diffusion process at a given temperature. For diffusion in pure metals, it is the general consensus that the dominant mechanism of diffusion is by monovacancies, although higher order defects such as divacancies may have a minor contribution at higher temperatures[10].

It is worth noting that the concept of self-diffusion applies not only to pure elements, but also equally well to homogeneous binary or multicomponent alloys, either with some components in dilution or all components in concentrated proportions. An interesting example of this class of diffusion process in solids is that of the solute diffusion in dilute binary alloys[14]. By means of radioactive

tracer experiments, one can determine both the diffusion rate of solute at very low concentration in the solvent and the solvent self-diffusion rate. For vacancy-assisted diffusion, one generally finds that the solute *impurity diffusion* constant and the solvent self-diffusion constant are similar in magnitude. For another class of solutes in certain solvents, the impurity diffusion constant can be several orders of magnitude higher than that of the solvent self-diffusion. Experimental evidence suggests that a certain interstitial type of mechanism rather than the vacancy mechanism has to be evoked in order to explain this kind of *anomalous fast-diffusion* behavior[14].

The types of diffusion described above all refer to the random atomic motion (defects may be required to assist this motion) in chemically homogeneous materials. In contrast to heat flow where no motion of the medium is required, diffusion in chemically inhomogeneous materials may produce a motion of the medium itself in addition to homogenization of the medium. For diffusion in binary alloys, this situation can be readily visualized. Imagine a fictitious plane in a diffusion couple across which both components interdiffuse. If the respective diffusion rates are different, extra material will accumulate on the side of the slower diffusing component measured from the fictitious plane. This situation is schematically illustrated in Fig. 1. From the reference frame of this plane, the whole diffusion couple participates in a translatory motion in the direction of the faster diffuser. Equivalently, the fictitious plane is moving in the direction of the slower diffuser viewed in the reference frame attached to one end of the diffusion couple. This is the *Kirkendall effect*[15].

In terms of an observer stationary with respect to one end of the

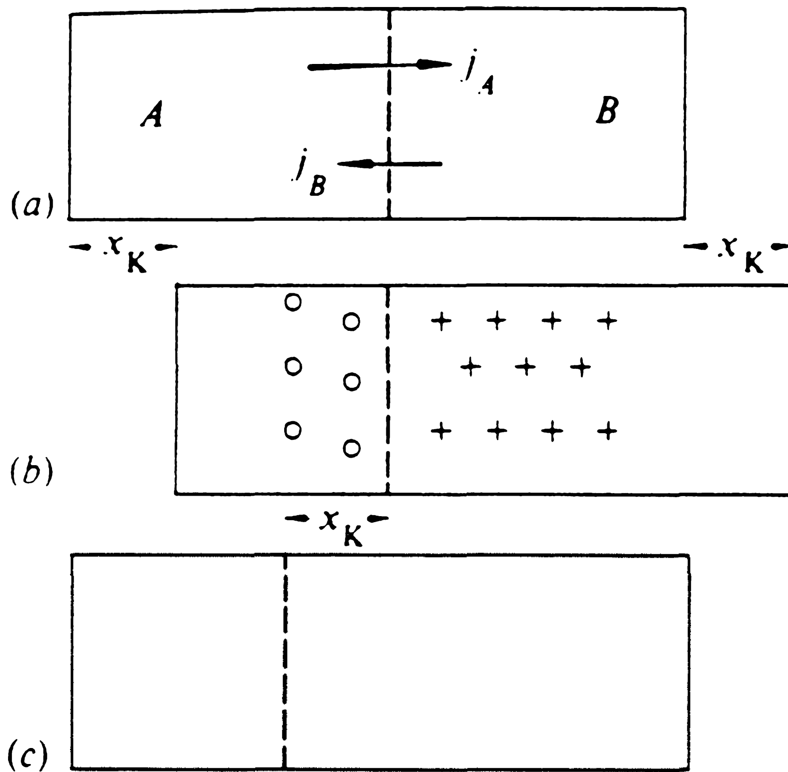

Fig. 1.1 Schematic illustration of the Kirkendall effect. Taken from Ref. 15.

diffusion couple, the flux of A and B atoms across the fictitious plane is according to the above discussion

$$J_A = -D_A \frac{\partial C_A}{\partial x} + vC_A \tag{14.1}$$

$$J_B = -D_B \frac{\partial C_B}{\partial x} + vC_B, \tag{14.2}$$

where v is the velocity of this plane. Combining Equation (14) with the condition of mass conservation for both A and B atoms, we arrive at

$$\frac{\partial(C_A + C_B)}{\partial t} = -\frac{\partial}{\partial x}[-D_A \frac{\partial C_A}{\partial x} - D_B \frac{\partial C_B}{\partial x} + v(C_A + C_B)]. \tag{15}$$

If we assume that the total density $C = C_A + C_B$ remains a constant throughout the diffusion process, then the quantity on the right-hand side of Equation (15) must be a constant throughout the whole diffusion couple. This constant must be zero since no mass transfer occurs at the end of the specimen. Thus, we must have

$$v = \frac{1}{C_A + C_B}[D_A - D_B]\frac{\partial C_A}{\partial x}. \tag{16}$$

Substituting Equation (16) into (14.1), we can then sidestep the problem of mass flow and write the A or B atom flux solely in terms of the concentration gradient of A or B atoms

$$J_{A(B)} = -[\frac{C_B}{C_A + C_B} D_A + \frac{C_A}{C_A + C_B} D_B]\frac{\partial C_{A(B)}}{\partial x}, \tag{17}$$

analogous to the original Fick's formulation of diffusion expressed by Equation (1). Diffusion process in binary alloys can thus be described either by the two *intrinsic diffusion constants* D_A and D_B, or completely equivalently by a single *interdiffusion* (or *chemical diffusion*) *constant* $\tilde{D}$ plus the associated equation for the velocity of mass flow (16). The interdiffusion constant $\tilde{D}$ is related to the two intrinsic diffusion constants by

$$\tilde{D} = N_B D_A + N_A D_B, \tag{18}$$

where N_A and N_B are the respective atomic compositions C_A/C and C_B/C. It is the interdiffusion constant that is determined in ordinary experiments.

In binary alloy systems, the general thermodynamic equilibrium condition is that the chemical potential for both components be constant throughout. Thus, in the spirit of irreversible thermodynamics, we expect that it is the gradient of chemical potential rather than that of concentration which constitutes the driving force for diffusion and produces mass currents[16]. If we assume that vacancies are in overall equilibrium, and further, that the cross correlations between the individual components are negligible (i.e., the chemical potential gradient for component B produces negligible current of component A), we can then write the respective atomic fluxes as

$$J_A = -C_A M_{AA} \frac{\partial \mu_A}{\partial x} \tag{19.1}$$

$$J_B = -C_B M_{BB} \frac{\partial \mu_B}{\partial x}, \tag{19.2}$$

where M_{AA} and M_{BB} are the mobilities of the individual components A and B[17]. Writing the gradient of chemical potential in terms of the gradient of concentration, we arrive at Darken's expression for the intrinsic diffusion coeficients

$$D_A = \frac{\partial \mu_A}{\partial ln N_A} M_{AA} \tag{20.1}$$

$$D_B = \frac{\partial \mu_B}{\partial ln N_B} M_{BB}. \tag{20.2}$$

1.2 Interdiffusion and Reactions in Thin Films

Although interdiffusion in multilayered metal-metal thin films was observed by Dumond et al. as early as 1940[18], a full-scale attack on the problem of diffusion and reactions in thin films began only with large-scale applications of thin films in integrated circuits[19]. Understanding interdiffusion and the formation of new phases at temperatures well below the elemental melting points is often imperative to assure satisfactory performance of circuit elements, as is evidenced by the problem of contact failure when a $AuAl_2$ compound forms at Al/Au junctions[20]. Advances in experimental techniques adequate to deal with variation of materials properties on the length scale of a few hundred angstroms, most noticeably the extensive usage of ion beam analysis techniques for probing composition profiles in thin films, and the use of transmission electron microscopy for characterizing the existence of various phases and their microstructures, have contributed enormously to the understanding of reactions in thin films[21,22]. A wealth of experimental results on the interdiffusion and reaction of binary diffusion couples now exists[23].

The simplest case of metal-metal interdiffusion occurring in a binary diffusion couple consists of single crystals of the individual components, which interdiffuse to form a continuous solid solution. The extrinsic diffusion mechanisms are well- known. For example, the rate of interdiffusion at low temperatures in a single crystal diffusion couple can be drastically different from that in a polycrystalline diffusion couple. In Ag-Au system, it has been demonstrated that diffusion via defects, e.g., grain boundaries, can be dominant at low temperatures[24]. In cases where interdiffusion leads to the formation of an intermetallic compound, the much faster diffusion via crystal defects, compared with diffusion in the bulk, may lead to irregular grain growth and island formation. Examples of such behavior

have been reported in the systems Al-Ni and Al- Hf[25,26]. Thus, the interdiffusion and reaction process may depend strongly on the morphology of the original diffusion couple. Reaction of metals with silicon has been extensively studied owing their importance in VLSI technology[27]. In contrast to metal-metal thin films, interdiffusion and reaction in metal-silicon systems generally begins with either single crystal or amorphous silicon. Although the bonding of metals and silicon is completely different, striking simplicities exhibit themselves in reaction of both bimetallic and metal-silicon thin films. In many systems, reaction of the two pure elements leads to a well-defined planar compound interlayer so that the growth process can be treated as one-dimensional.

Growth of any compound in a binary diffusion couple involves transport of one or of both types of atoms to one or both compound/element interphase interfaces and a subsequent reaction at these interfaces to form additional compound. Both diffusion across the compound layer and interfacial reaction kinetics can be rate-limiting. In the limit where the compound interlayer is extremely thin, the transport of atoms across it by diffusion will take little time and the rate-limiting step in compound formation is expected to be the interfacial reaction. In this case, the reaction is termed *interface-controlled.* If, on the other hand, the compound interlayer is very thick, the interdiffusion process will be rate-limiting and the reaction is termed *diffusion-controlled.*

The binary phase diagram will typically predict several compounds in a binary system, and according to early theories based on diffusion controlled growth of compound layers, all compounds that appear in the phase diagram should

appear simultaneously in an actual interdiffusion experiment[28]. Experimentally, however, the evolution of a diffusion couple consisting of two pure elements proceeds in a dramatically different way. For both metal-metal or metal-silicon systems, it is generally observed that only one compound forms and grows initially. The formation of the second compound does not occur until a certain critical thickness of the first compound interlayer has been reached. Examples of such behavior include Al-Au and Ni-Si[29,30]. The eventual outcome of such interdiffusion experiments agrees with that predicted by the equilibrium phase diagram, satisfying the thermodynamic equilibrium requirement. However, the process of reaching equlibrium seems to be one where *compounds form sequentially* instead of simultaneously.

In the course of compound formation in a diffusion couple, the process of interdiffusion is often dominated by the movement of one element, the so-called *dominant moving species.* Attempts to identify the dominant moving species in a binary diffusion couple date back to work by Kirkendall around 1940. An inert wire was embedded at the interface of a bulk diffusion couple; the dominant moving species was identified according to the direction of movement of the wire[31]. As discussed in Section 1.1, the role of the inert marker, in this case the inert wire, is to mark out the "fictitious plane." Modern marker experiments in thin films generally employ an extremely thin ($\sim$ 10Å) layer (or, in fact, isolated islands) of inert and immobile atoms, ideally buried inside the compound layer to avoid dragging of the marker by the original element/compound interface[27]. Most marker experiments in thin films have been carried out on metal-silicon systems where the motion of the marker, prepared either by evaporation or ion implantation, is detected by Rutherford backscattering spectrometry[27].

Although there is an abundance of experimental information about interdiffusion and reaction in thin films, to date, certain fundamental questions in this field remain unanswered. One of the most prominent problems is the prediction of the particular phase that forms first in a diffusion couple consisting of two pure elements. Walser and Bene have formulated a rule predicting the *first phase* in the case of reacting metals with silicon. The argument is heuristic in that it presupposes that a thin glassy interlayer forms at the metal/silicon interface during or post preparation, and the first silicide to nucleate upon annealing of the diffusion couple is basically the crystallization product from the glassy membrane[32]. Although this rule accounts, with some success, for the body of existing data on silicide formation, exceptions to this rule do exist. Gosele and Tu have shown that, contrary to early theories that assume diffusion-controlled growth of compound phases, the diffusional flux through a particular compound phase does not go to infinity in the limit of small compound interlayer thickness because of the presence of interfaces. Thus, it is possible that even though all compound phases could nucleate at the original elemental interface, some would not grow initially because of unfavorable interfacial kinetic parameters for growth[33]. Their theory predicts that the first phase to form is the one with the highest *interface mobility*. The parameters in this theory, being phenomenological, can be obtained from a combination of experiments, at least in principle, although to the author's knowledge, there have been no systematic experiments to test the validity of this theory. At present, there exists no satisfactory rule that predicts the first phase or accounts for the *sequence of phase formation* in general, including the successive phases.

1.3 Metastable Phases

Man's experience with metastable materials stems from his everyday life. Substances ranging from ordinary window glass to diamonds all belong to the class of material we call metastable, which by definition could have their free energy lowered by transforming into different phases. The transformation of some metastable materials into thermodynamic equlibrium states can be an extremely slow process, as exemplified by the common belief that diamonds exist "forever." On the other hand, at the extremities of metastability lies another class of material which we call unstable. How to distinguish between *metastability* and *instability*, and how to establish a measure of metastability are amongst the most fundamental questions relating to *nonequilibrium materials.*

Consider a homogeneous binary solid solution of A and B with its Gibbs free energy versus composition shown schematically in Fig. 2. A simple example of such behavior can be obtained in a model system of regular solution with a positive interaction parameter[34]. It is apparent that any homogeneous solution with composition N_A ranging between N_α and N_β is not in equilibrium since its free energy can be lowered by separating into a mixture of two components α and β. However, inside this nonequilibrium region, solutions with compositions $N_\alpha < N_A < N_{\alpha'}$ or $N_{\beta'} < N_A < N_\beta$ are qualitatively different from solutions with compositions $N_{\alpha'} < N_A < N_{\beta'}$. Composition fluctuations in the latter region, however small, result in a decrease in the free energy. Small fluctuations in composition in the former region cause the free energy to increase, and a decrease in free energy is obtained only for a sufficiently large concentration fluctuation. The difference in these two types of phase regions is a manifestation of the different curvature of the free energy of the solid solution with respect to its composition. The transition

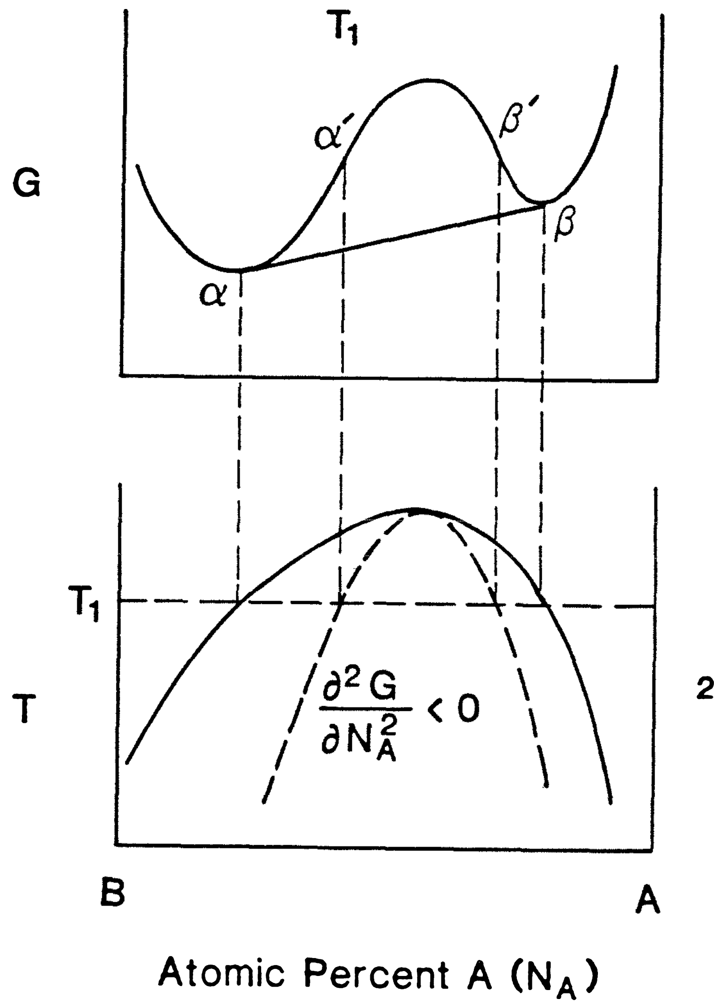

Fig. 1.2 Hypothetical free energy diagram and the associated phase diagram of a binary system (A-B) with a positive enthalpy of mixing.

points between these different regions are marked by α' and β', where the second derivative of the free energy with respect to composition is zero. The loci of $N_{\alpha'}$ and $N_{\beta'}$ as a function of temperature defines the *spinodal curve* in the corresponding phase diagram[34].

Thermal fluctuations are responsible for the eventual transformation of the nonequilibrium solid solution into its equilibrium counterpart. The nature of these fluctuations can be separated into two categories[35]. One is an infinitesimal composition fluctuation spread over a large volume; the other one is a large fluctuation localized in a very small volume within which the material resembles that of a different phase. The nature of a long wavelength composition fluctuation can be examined as follows. In general, one expects that the total free energy G of a solid solution is dependent not only on the composition, but also on the composition variation[36]. If we assume that this variation is small, then the total free energy can be expanded in terms of the composition gradient

$$G = \int_V [G_o(N_A) + K(\nabla N_A)^2] dV, \tag{22}$$

where G_o is the free energy per unit-volume and depends only on the local composition. The second term in the integrand expresses the dependence of the total free energy on spatial composition variation to lowest order[36]. The change in the total free energy of the system, initially homogeneous with composition N_A° when subjected to a sinusoidal fluctuation

$$N_A = N_A^\circ + A\cos\beta x, \tag{23}$$

can then be calculated from Equation (22) by expanding G_o in powers of $N_A - N_A^\circ$.

The result is

$$\Delta G = \frac{A^2 V}{4}\left[\frac{\partial^2 G_\circ}{\partial N_A^2} + 2K\beta^2\right], \tag{24}$$

where V is the total volume and K the positive gradient energy coefficient[37]. The second-order partial derivative of the free energy with respect to composition is evaluated at N_A°. Thus, if $\partial^2 G_\circ/\partial N_A^2$ is positive, then the total free energy of the system will be raised by composition fluctuations at all wavelengths. On the other hand, if $\partial^2 G_\circ/\partial N_A^2$ is negative, then a lowering of the total free energy will be obtained by all composition fluctuations with a wavelength larger than a critical value λ_c, where

$$\lambda_c = \left[\frac{8\pi^2 K}{\left(-\frac{\partial^2 G_\circ}{\partial N_A^2}\right)}\right]^{\frac{1}{2}}, \tag{25}$$

regardless of the amplitude of fluctuation. Such *spinodal decomposition* can continuously lower the total free energy of the system via rather long wavelength concentration fluctuations. The limit of metastability in a binary solid solution is defined by the spinodal curve. The requirement for chemical stability in binary solid solutions

$$\frac{\partial^2 G_\circ}{\partial N_A^2} > 0 \tag{26}$$

is but one of a set of general criteria for thermodynamic stability against various types of fluctuations. A particular material is unstable against certain fluctuations if the corresponding Gibb's stability criterion is violated[38].

In the case of localized fluctuations, the small region can be regarded as a *nucleus* of another phase and the well-known theory of *nucleation* describes such processes[39]. If we assume that we can describe the separation between a nucleus and the original matrix by an interface and associate with this interface an interfacial energy σ, then the interfacial energy dominates when the nucleus is small

so its surface-to- volume ratio high. The total change of free energy when a nucleus is formed (the nucleus is assumed to be spherical with radius r for simplicity) is given by the sum of a volume and a interface term

$$\Delta G = 4\pi r^2 \sigma + \frac{4}{3}\pi r^3 \Delta G_o, \tag{27}$$

where ΔG_o is the change in volume free energy associated with the transformation. In order for the nucleus to grow, we must have $d(\Delta G)/dr < 0$; thus, we obtain the critical free energy ΔG^* or the activation energy for nucleation

$$\Delta G^* = \frac{16\pi}{3} \frac{\sigma^3}{(\Delta G_o)^2}. \tag{28}$$

A finite energy barrier to such nucleation events therefore exists as long as the interfacial energy between the nucleus and the matrix is positive. Assuming that this is the case, we see that the solid solution depicted in Fig. 2 with its composition inside the two phase α and β coexistence region is truely metastable and not unstable against such localized fluctuations regardless of whether it is within the spinodal, in the sense that a finite energy barrier has to be overcome before the nucleus can grow. The instability of any solid solution with composition inside the spinodal region stems from the fact that its free energy can be continuously lowered by long wave length composition fluctuations where no well-defined interface exists. Since the activation energy for nucleation is critically dependent on the interfacial energy, oftentimes nucleation of one particular phase occurs because of its lower interfacial energy with the parent phase despite the fact that another phase may have still lower free energy. One example of such sequential precipitation of metastable and finally stable phases in supersaturated solid solutions is the case of Al-Cu[40]. The fact that many metastable phases, once formed, seem to be highly stable is due to the slow nucleation of the equilibrium phases. Since atomic mobility is dependent on

temperature exponentially, at low enough temperatures, even when the nucleation centers are present, negligible growth of these nuclei will result. Thus, the degree of metastability of a particular phase, i.e., its resistance against transformation to phases lower in free energy, is a combination of effects due to *nucleation and growth.*

Synthesis of metastable phases can be achieved by condensation of vapor on a substrate in the so-called *vapor-quenching* technique, pioneered by Buckel and Hilsch[41]. In this case, the vapor is converted into a solid, atom by atom, upon arrival at the substrate. This condensation process can be dictated to take place at any desired temperature, e.g., at cryogenic temperatures. In particular, since any two elements are completely soluble in the vapor phase, one might hope to obtain homogeneous solid solutions in systems with essentially no solid solubility. A wide variety of materials including alkali halides, heavy metal halides, pure metals, binary alloys and pseudobinary admixtures of different types of salts have been evaporated onto substrates with temperatures ranging from room temperature down to liquid helium temperature[42]. During early investigations, particular emphasis was on the conditions under which an amorphous substance could be obtained. It was discovered that pure metals and pure salts only rarely became amorphous even when evaporated onto liquid-helium temperature substrates. Exceptional cases such as pure Bi or pure Ga can be made amorphous by condensing onto liquid-helium temperature substrates but transform into the crystalline state below 20K[42]. Later, many works showed that by vapor quenching suitable binary and multicomponent alloys of a wide variety of metals, concentrated amorphous alloys could be obtained that do not transform to the crystalline state up to well above room temperature[43,44]. Among such studies, the early work of Mader et

al. has demonstrated some important features[45]. By coevaporation of pure Cu and pure Ag with control of individual evaporation rates onto amorphous substrates held at liquid nitrogen temperature, they were able to produce concentrated amorphous alloys with 35-65% Ag content, while evaporation of dilute alloys resulted in a metastable single phase f.c.c. solid solution. It is now generally believed that there exists a continuous range of composition in many binary alloy systems within which an amorphous phase can be obtained by vapor quenching[47]. In the case of Ag-Cu, if the substrate was kept at 200K instead of 80K, a solid solution rather than the amorphous phase was obtained at all compositions[45]. The latter fact led the above authors to conclude that the crystalline structure will be reached if some surface diffusion is permitted during vapor deposition. Such competition between the atomic arrival rate, in vapor quenching determined by the evaporation rate, and the rate of nucleation and growth of various phases, metastable or stable, constitutes a main theme in the synthesis of metastable materials. Early works suggest that atomic size mismatch between the two components is important and an amorphous alloy will be obtained if the atomic size difference is greater than 10%[46]. Recently, the effect of atomic size mismatch of the two elements on the *glass- forming range* in the binary alloy was reexamined by Egami et al.[48]. It is argued on the basis of elasticity theory that, when atomic size mismatch is sufficiently large, a critical concentration exists in the crystalline solid solution beyond which the solid solution is rendered topologically unstable by the atomic level stresses that arise from atomic size mismatch. This theoretically predicted critical concentration is used with good success to correlate with experimentally obtained glass forming range in vapor deposited binary thin films[47]. When two elements with virtually the same size, such as Fe and Cu, are codeposited onto a substrate, a metastable crystalline phase always results instead of an amorphous alloy[49].

Intense research effort on the synthesis of new metastable alloys, including amorphous alloys, from the liquid state was launched after the demonstration by Duwez et al., that a metastable extension of solid solubility in the system Cu-Ag was possible by rapidly cooling a binary liquid of Cu and Ag[50]. Shortly afterward, a metastable crystalline phase of Ag-Ge was obtained by such a *liquid quenching* technique[51], and then an amorphous alloy of Au-Si was also obtained for the first time by quenching from the liquid state[52]. Preparation of amorphous alloy by liquid quenching is unique in that, if formation of crystalline phases can be avoided, the undercooled liquid will eventually go through a kinetic freezing or *glass transition* at a temperature T_g[53]. Below the glass transition temperature, the undercooled liquid is no longer able to sample all available atomic configurations and the amorphous solid so obtained is said to retain a single frozen-in topological configuration of the liquid state. To achieve the amorphous state, fast cooling of the liquid is necessary in the undercooled regime down to T_g. According to classical nucleation theory, the rate of crystallization from the undercooled melt reaches a maximum at a specific temperature T_n below the melting temperature[54], as shown schematically in Fig. 3. Therefore, if the liquid can be cooled from above the melt point to well below T_n in time less than that required to nucleate crystalline phases, the undercooled liquid will reach T_g without crystal formation, thus forming a glass. Again, it is the competition between two kinetic processes, cooling of the liquid on one hand, and nucleation and growth of the crystalline phases on the other, which determines whether or not an amorphous alloy will be formed. Experimentally, fast cooling of the liquid is achieved by jetting a stream of liquid against a cold metal substrate. The resultant geometric configuration of the quenched specimen is necessarily a thin ribbon or foil so that heat can be conducted away effectively during quenching. Variations of such cooling schemes give rise to techniques referred to as

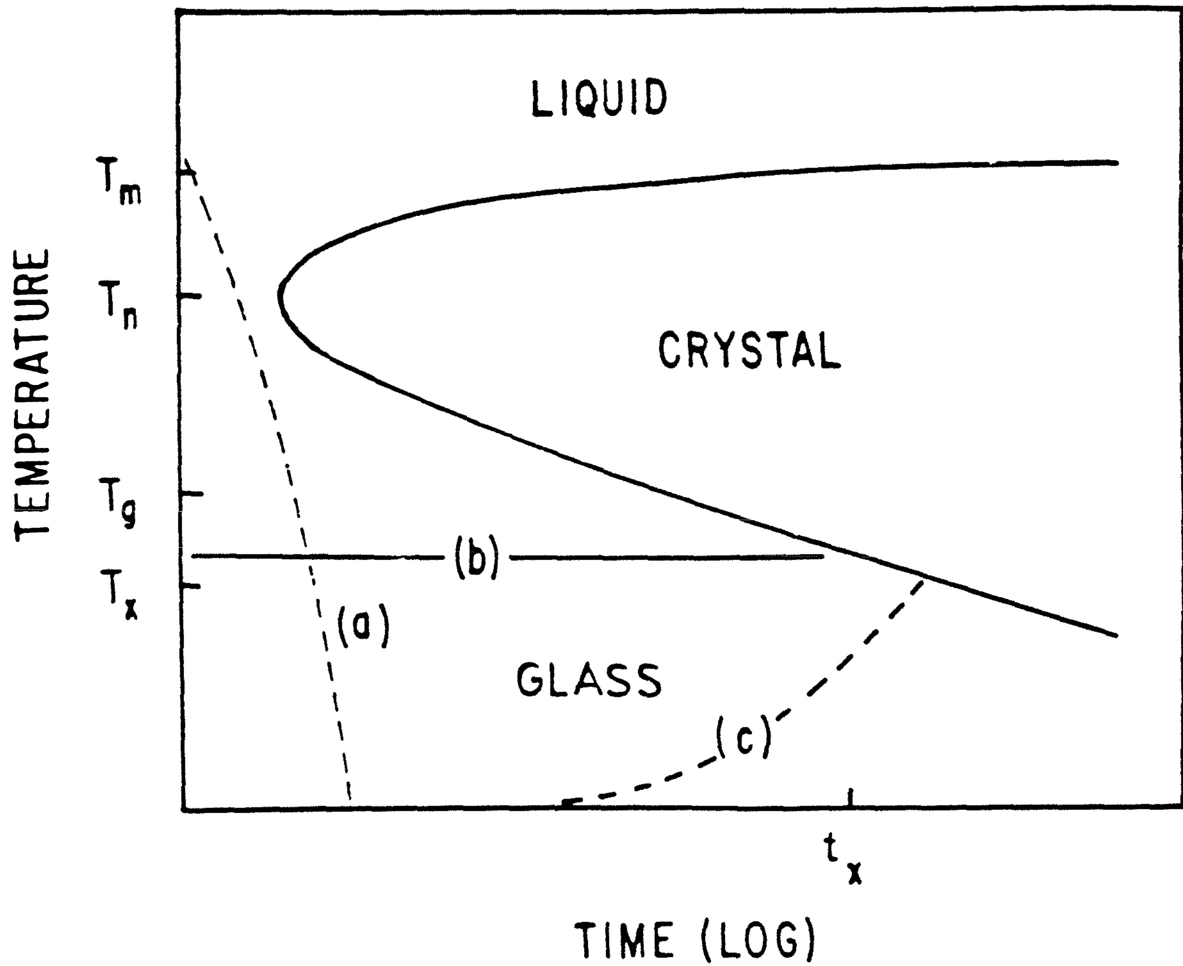

Fig. 1.3 Schematic Time-Temperature-Transformation (TTT) diagram for crystal growth in an undercooled melt. Taken from Ref. 54.

the *gun* technique, the *piston and anvil* and the *melt spinning* techniques, etc. The cooling rate achieved in such experiments ranges from 10^5 to 10^8 K/sec[55]. The term *glass* is traditionally associated with an amorphous solid obtained by cooling from the liquid state. In what follows, we will use the terms amorphous solid and glass without distinction. From the above discussion, we expect that by varying the cooling rate and depending on the specific alloy system, a wide variety of phases in addition to amorphous phases can be formed directly from the liquid state. Experimentally, supersaturated binary solid solutions in systems such as Cu-Ag, Cu-Rh, Pt-Ag, over 60 binary non-equilibrium crystalline phases and a large number of binary and ternary amorphous phases have all been obtained by rapid quenching from the melt[55]. Large- scale production of liquid quenched alloys is now yielding commercially important materials for a number of applications[56].

1.4 Solid State Amorphization

The first example of synthesis of an amorphous alloy from the solid state by Yeh et al. involved reaction of hydrogen gas with a metastable crystalline Zr_3Rh alloy[57]. It was quickly realized that certain thermodynamic and kinetic conditions are satisfied in such a reaction. Thermodynamically, the final amorphous Zr_3RhH_x hydrid has considerablly lower free energy than that of the initial state. Kinetically, the time scale for the system to reach the thermodynamic equilibrium state, which is a chemically segregated state of pure Rh plus ZrH_2, is much longer than that of reaching a chemically homogeneous metastable state, the amorphous state, by hydrogen diffusion[58]. These two conditions, one thermodynamic and one kinetic, were used as guide lines to search for other systems that may exhibit

similar *solid state amorphization* behavior. Subsequently, Schwarz and Johnson showed that multilayered diffusion couples consisting of crystalline La and Au individual layers can be transformed into an amorphous La-Au alloy by isothermal heat treatment at low enough temperatures[59]. Although the amorphous La-Au alloy is expected to have a large negative heat of mixing and thus furnishes the thermodynamic driving force for this reaction, the kinetic condition of the disparity between the time scales for reaching the amorphous state and the equilibrium crystalline state was originally justified in terms the anomalous solute diffusion of Au in the La matrix. It was later pointed out that fast diffusion of Au in the amorphous state also occurs but can be a few orders of magnitude slower than the corresponding solute diffusion in crystalline La[60]. The curious correlation between fast impurity diffusion in the crystalline matrix and substantial mobility of the fast diffuser in the amorphous alloy remains without a fundamental explanation at present. Presumably it is associated with the atomic size difference between Au and La. The synthesis of an amorphous alloy in diffusion couples consisting of crystalline elemental starting layers is accomplished solely by reaction in the solid state without the necessity of gaseous hydrogen acting as the fast-diffusing element. This method thus opens up a new route for synthesizing metastable amorphous materials. To date, solid state amorphization has been observed in numerous metal-metal systems including early-late transition metal, noble-rare earth metal systems, etc.[61]. More recently, a number of metal-silicon systems have been observed to form amorphous silicides by solid state reaction, including Rh-Si, Ti- Si, and Ni-Si[62,63,64]. Thus, the glassy membrane originally hypothesized by Walser and Bene[32] has taken on a new significance. It is to be emphasized that production of metastable phases by interdiffusion reaction in the solid state is not limited to that of amorphous phases. Experiments stimulated by the discovery that amorphous alloys can be produced

by reactions in the solid state have thus far shown that many metastable alloys, crystalline or non-crystalline, can be obtained via the same route under suitable conditions. Most recent examples include the formation of the Al-Mn quasi- crystalline phase in elemental Al/Mn diffusion couples and metastable bcc solid solution and subsequently the A15 phase in Nb-Al systems[65,66,67].

1.5 Introduction to the Thesis

This thesis will focus on the study of interdiffusion and reaction in planar thin film diffusion couples of pure Ni and Zr. As will be exemplified through-out this thesis, the ability of synthesizing planar thin film diffusion couples with high purity and well-characterized geometry and well-defined interfaces is crucial for being able to address and answer some key problems in such a study. In Chapter 2, we will describe the high vacuum sputter deposition system we have constructed for fabrication of thin-film diffusion couples used in this research. Formation of an amorphous NiZr alloy in vapor deposited polycrystalline Ni/Zr thin film diffusion couples was first demonstrated by Clemens et al.[68] and constitutes one of the earliest examples of solid state amorphization reactions in metal-metal systems. The process of interdiffusion and reaction in Ni/Zr diffusion couples is subsequently studied as a prototype case of solid-state reactions by many others, using a wide variety of experimental techniques. The use of the Rutherford backscattering spectrometry (RBS) technique has elucidated some important aspects of the growth kinetics of the amorphous NiZr interlayer. Barbour has shown, using RBS, that the growing amorphous NiZr interlayer possesses a linear concentration profile with constant interfacial compositions determined by equilibrium conditions[69]. Cheng et al. have

shown, using a marker technique together with RBS measurements, that Ni is the dominant moving species in the formation of amorphous NiZr in Ni/Zr diffusion couples during solid-state reaction[70]. The choice of Ni-Zr system was originally guided by the fact that a large negative heat of mixing exists in this system and Ni is known to be a fast diffuser in crystalline Zr[71,72]. In Chapter 3, we will describe our study of the growth kinetics and thermodynamics of amorphous NiZr formation in sputter-deposited polycrystalline Ni/Zr multilayered diffusion couples. With a combination of experimental techniques such as x-ray diffraction, differential scanning calorimetry, and resistivity measurements, the process of amorphous phase formation can be studied in some detail. We have directly measured the heat of mixing of amorphous NiZr alloys via calorimetric methods and confirmed that it constitutes the major thermodynamic driving force toward amorphization in this system[73,74]. The growth kinetics of the amorphous NiZr has also been measured. We have shown that, although substantial atomic transport through the amorphous NiZr occurs during reaction, the measured diffusion constant is still orders of magnitude below that of Ni impurity diffusion through crystalline Zr[74,75]. Vredenberg et al. have shown that, in contrast to the results obtained using vapor-deposited polycrystalline Ni/Zr diffusion couples, the use of a single crystal of Zr in a bilayered polycrystalline-Ni/single crystal-Zr diffusion couple prohibits the formation of the amorphous NiZr alloy[76]. Using the RBS technique, they showed that no reaction occurred in such a polycrystalline-Ni/single crystal-Zr diffusion couple at elevated temperatures for extended periods of time. Thus these authors concluded that the use of single crystal Zr creates a nucleation barrier against amorphous phase formation. In a related study, Pampus et al. have shown that the use of single crystal Ni in contact with polycrystalline Zr does not pose such a nucleation barrier for the amorphous NiZr formation[77]. We have since fabricated bilayered diffusion

couples of Ni and Zr in our vacuum deposition system where one layer consists of a mosaic of large single crystals with typical grain sizes in the 10 μm range. In addition to creating the above-mentioned polycrystal/single crystal interfaces, our sample configuration allows further examination of the role of grain boundaries on the reaction process[78]. In Chapter 4, the reaction process of such Ni/Zr diffusion couples is examined together with sputter- deposited polycrystalline Ni/Zr diffusion couples by the technique of transmission electron microscopy. Emphasis is placed not only on the process of amorphous phase formation but also on the observation of the formation of the Ni-Zr compound phase succeeding that of the amorphous phase[79]. Such a study provides a concrete example of the phase-sequencing behavior observed in many thin film diffusion couples. We will attempt to ellucidate the key ingredients for understanding the evolution of diffusion couples in general.

1.6 References

1. M. Faraday, Phil. Trans. Roy. Soc. London **147**, 145 (1857).
2. W. R. Grove, Phil. Trans. Roy. Soc. London **142**, 87 (1852).
3. H. Hertz, Ann. Physik **17**, 177 (1882).
4. M. Knudsen, Ann. Physik **47**, 697 (1915).
5. J. Plucker, Ann. Physik **103**, 88, 151 (1858).
6. K. L. Chopra, *Thin Film Phenomena*, Ch. 9 & 10 (McGraw-Hill, New York, 1969).
7. A. Fick, Annln Phys. **170**, 59 (1855).
8. J. Crank, *The Mathematics of Diffusion* (Oxford University Press, London, 1975).
9. See e.g., G. M. Hood, R. J. Schultz, Phil. Mag. **26**, 329 (1972).
10. N. L. Peterson, J. Nucl. Mater. **69** & **70**, 3 (1978).
11. A. D. Le Claire, in *Physical Chemistry - An Advanced Treatise*, Vol. 10, Ch. 5 (Academic Press, 1970).
12. R. A. Swalin, *Thermodynamics of Solids*, Ch. 11 (Wiley, New York, 1972).
13. H. Eyring, S. Glasstone, K. Laider, *Theory of Rate Processes* (McGraw-Hill, New York, 1941).
14. A. D. Le Claire, J. Nucl. Mater. **69** & **70**, 70 (1978).
15. P. Haasen, *Physical Metallurgy*, Ch. 8 (Cambridge University Press, London, 1978).
16. W. Yourgrau, A. van der Merwe, G. Raw, *Treatise on Irreversible and Statistical Thermophysics* (Dover, New York, 1982).

17. J. W. Christian, *The Theory of Transformations in Metals and Alloys*, Ch. 9 (Pergamon Press, Oxford, 1975).

18. J. Dumond, J. P. Youtz, J. Appl. Phys. **11**, 357 (1940).

19. S. M. Sze, *Physics of Semiconductor Devices* (Wiley, New York, 1981).

20. C. Weaver, *Physics of Thin Films*, edited by M. H. Francombe and R. W. Hoffman, Vol. 6, p. 301 (Academic Press, New York, 1971).

21. W. K. Chu, J. W. Mayer, M. A. Nicolet, *Backscattering Spectrometry* (Academic Press, New York, 1978).

22. L. Reimer, *Transmission Electron Microscopy* (Springer-Verlag, Berlin, 1984).

23. See, e.g., *Thin Film Phenomena - Interfaces and Interactions*, edited by J. E. E. Baglin and J. M. Poate, Proceedings Vol. 78-2, the Electrochemical Society, Atlanta, 1978.

24. R. G. Kirsch, J. M. Poate, M. Eibschutz, Appl. Phys. Lett. **29**, 772 (1976).

25. R. F. Lever, J. K. Howard, W. K. Chu, P. J. Smith, J. Vac. Sci. Tech. **1**, 158 (1977).

26. J. E. E. Baglin, F. M. d'Heurle, in *Ion Beam Surface Layer Analysis*, Vol. 1, edited by O. Meyer, G. Linker, F. Kappeler, p. 385 (Plenum Press, New York, 1976).

27. K. N. Tu, J. W. Mayer, in *Thin Films - Interdiffusion and Reactions*, edited by J. M. Poate, K. N. Tu, J. W. Mayer, Ch. 10 (Wiley, New York, 1978).

28. G. V. Kidson, J. Nucl. Mater. **3**, 21 (1961).

29. S. U. Campisano, G. Foti, E. Rimini, S. S. Lau, J. W. Mayer, Phil. Mag. **31**, 903 (1975).

30. K. N. Tu, E. I. Alessandrini, W. K. Chu, H. Krautle, J. W. Mayer, Jap. J. Appl. Phys. Suppl. **2**, Pt. 1, 669 (1974).

31. A. D. Smigelskas, E. O. Kirkendall. Trans. AIME **171**, 130 (1947).

32. R. M. Walser, R. W. Bene, Appl. Phys. Lett. **28**, 624 (1976).

33. U. Gosele, K. N. Tu, J. Appl. Phys. **53**, 3252 (1982).

34. L. E. Reichl, *A Modern Course in Statistical Physics*, Ch. 4 (University of Texas Press, Austin, 1980).

35. J. W. Cahn, Acta Met. **9**, 795 (1961).

36. J. W. Cahn, J. E. Jilliard, J. Chem. Phys. **28**, 258 (1958).

37. J. W. Cahn, Trans. Metallur. Soc. AIME **242**, 166 (1968).

38. L. E. Reichl, *A Modern Course in Statistical Physics*, Ch. 2 (University of Texas Press, Austin, 1980).

39. J. W. Christian, *The Theory of Transformations in Metals and Alloys*, Ch. 10 (Pergamon Press, Oxford, 1975).

40. P. Haasen, *Physical Metallurgy*, Ch. 9 (Cambridge University Press, London, 1978).

41. W. Buckel, R. Hilsch, Z. Physik **138**, 109 (1954).

42. R. Hilsch, *Non-Crystalline Solids*, edited by V. D. Frechette, Ch. 15 (Wiley, New York, 1960).

43. S. K. Khanna, A. P. Thakoor, R. F. Landel, M. Mehra, W. L. Johnson, Appl. Phys. Commun. **1**, 135 (1982).

44. C. L. Chien, K. M. Unruh, Phys. Rev. B **25**, 5790 (1982).

45. S. Mader, A. S. Nowick, H. Widmer, Acta Met. **15**, 203 (1967).

46. S. Mader, J. Vac. Sci. Tech. **2**, 35 (1965).

47. S. H. Liou, C. L. Chien, Mater. Res. Soc. Symp. Proc. **80**, 145 (1987).

48. T. Egami, Y. Waseda, J. Non-Cryst. Solids **64**, 113 (1984).

49. C. L. Chien, S. H. Liou, D. K. Kofalt, W. Yu, T. Egami, T. R. McGuire, Phys. Rev. B **33** 3247 (1986).

50. P. Duwez, R. H. Willens, W. Klement, J. Appl. Phys. **31**, 1136 (1960).

51. P. Duwez, R. H. Willens, W. Klement, J. Appl. Phys. **31**, 1137 (1960).

52. W. Klement, R. H. Willens, P. Duwez, Nature **187**, 869 (1960).

53. A. E. Owen, in *Amorphous Solids and the Liquid State*, edited by N. H. March, R. A. Street, M. Tosi, Ch. 12 (Plenum Press, New York, 1985).

54. M. G. Scott, *Amorphous Metallic Alloys*, edited by F. E. Luborsky, Ch. 10 (Butterworths, London, 1983).

55. T. R. Anantharaman, C. Suryanarayana, J. Mater. Sci. **6**, 1111 (1971).

56. D. Raskin, C. H. Smith, *Amorphous Metallic Alloys*, edited by F. E. Luborsky, Ch. 20 (Butterworths, London, 1983).

57. X. L. Yeh, K. Samwer, W. L. Johnson, Appl. Phys. Lett. **42**, 242 (1983).

58. X. L. Yeh, Ph. D. thesis (California Institute of Technology, Pasadena, California, 1987).

59. R. B. Schwarz, W. L. Johnson, Phys. Rev. Lett. **51**, 415 (1983).

60. W. L. Johnson, B. Dolgin, M. Van Rossum, in Proceedings of the NATO Advanced Study Institute, Tenerife (April, 1984).

61. W. L. Johnson, Prog. Mater. Sci. **30**, 81 (1986).

62. S. Herd, K. N. Tu, K. Y. Ahn, Appl. Phys. Lett. **42**, 597 (1983).

63. K. Holloway, R. Sinclair, J. Appl. Phys. **61**, 1359 (1987).

64. D. M. Vanderwalker, Appl. Phys. Lett. **48**, 707 (1986).

65. D. M. Follstaedt, J. A. Napp, Phys. Rev. Lett. **56**, 1827 (1986).

66. R. Bormann, H. U. Krebs, A. D. Kent, in *Advances in Cryogenic Engineering*, edited by A. F. Clark and R. P. Reed, p. 1041 (Plenum Press, New York, 1986).

67. J. R. Gavaler, A. I. Braginski, J. Greggi, K. Schulze, J. Appl. Phys. **61**, 659 (1987).

68. B. M. Clemens, W. L. Johnson, R. B. Schwarz, J. Non- Cryst. Solids **61** & **62**, 817 (1984).

69. J. C. Barbour, Phys. Rev. Lett. **55**, 2872 (1985).

70. Y. T. Cheng, W. L. Johnson, M. A. Nicolet, Appl. Phys. Lett. **47**, 800 (1985).

71. A. R. Miedema, R. Boom, F. R. De Boer, J. Less Common Met. **41**, 283 (1975).

72. G. M. Hood, R. J. Schultz, Acta Met. **22**, 459 (1974).

73. E. J. Cotts, W. J. Meng, W. L. Johnson, Phys. Rev. Lett. **57**, 2295 (1986).

74. W. J. Meng, E. J. Cotts, W. L. Johnson, Mater. Res. Soc. Symp. Proc. Vol. 77, 223 (1987).

75. K. M. Unruh, W. J. Meng, W. L. Johnson, Mater. Res. Soc. Symp. Proc. Vol. 37, 551 (1985).

76. A. M. Vredenberg, J. F. M. Westendorp, F. W. Saris, N. M. van der Pers, Th. H. de Keijser, J. Mater. Res. **1**, 774 (1986).

77. K. Pampus, K. Samwer, J. Bottiger, Europhys. Lett. **3**, 581 (1987).

78. W. J. Meng, C. W. Nieh, E. Ma, B. Fultz, W. L. Johnson, in Pro-

ceedings of the Sixth International Conference on Rapidly Quenched Metals, Montreal, August 3-7, 1987.

79. W. J. Meng, C. W. Nieh, W. L. Johnson, Appl. Phys. Lett. **51**, 1693 (1987).

Chapter 2

High Vacuum Sputter Deposition of Thin Films

Techniques for fabrication of thin solid films include thermal evaporation, electron beam evaporation and various sputter deposition methods[1]. Thermal evaporation of some pure elements, e.g., refractory metals, by resistive heating can be rather difficult, and it has been increasingly replaced by the method of electron beam evaporation. Electron beam (e-beam) evaporation occurs in vacuum without the need of a carrier gas and is thus compatible with ultra-high-vacuum (UHV) requirements. For this reason, it has been extensively used in vapor-phase synthesis of thin films where the UHV condition is required, such as in Molecular Beam Epitaxial (MBE) growth of semiconductor devices[2]. However, control and stabilization of the e-beam evaporation rate is difficult and real time feedback control is often necessary to ensure stability of deposition. Furthermore, since the constituents present in a binary liquid usually differ in their vapor pressures, the composition of the vapor and consequently that of the condensed thin binary film is often different from the composition of the binary alloy used as the evaporation source. Thus, compound thin films are usually prepared by simultaneous co-evaporation of elemental constituents from separate sources with individual rate control, making the overall process quite complex. We have chosen, in this project, to utilize instead the technique of planar magnetron sputter deposition for the preparation of thin-film diffusion couples. This chapter serves as an introduction to the sputter-deposition technique itself as well as a more detailed account of some specific features particular to the sputter-deposition system contructed for use in

this research.

2.1 Introduction to Sputter Deposition

Sputtering refers to the erosion of solid surfaces under particle bombardment[3]. In particular, energetic ions are slowed when impinging onto solid surfaces and deposit energy into the solid, some near-surface atoms are ejected as a result of this energy deposition. In addition, many other effects are created by incoming ions such as radiation damage and ion-beam mixing if the initial solid is inhomogeneous[4]. Although observation of cathode erosion in discharge tubes has been observed over one hundred years ago, reliable experimental information on sputtering was obtained mainly during the last thirty years because of the advances in particle accelerators and high-vacuum technology. The sputtering process is largely characterized by the sputtering yield Y, defined as the average number of solid atoms ejected per incident particle. For bombardment of metal targets by noble gas ions in the 100 eV to 1 KeV range, Y usually ranges from 10^{-2} to 10[5].

Energetic ions incident upon a solid dissipate their energy by elastic collisions with the target atoms and by the creation of electronic excitations. Binary collisions between incident ions and target atoms can displace the target atoms, and these primary recoil target atoms undergo further collisions with more target atoms to generate higher order recoils, thus generating a *collision cascade.* Some of the recoil target atoms may reach the surface and may be ejected if they are energetic enough to overcome the surface binding forces. The theory of collision cascade

sputtering is most developed in the *linear cascade* region where it is assumed that the spatial density of moving atoms is small, and binary collisions happen mainly between one moving atom and another at rest. In this case, the sputtering yield Y is given by the expression[6]

$$Y(E, \Theta, x) = \frac{0.042 F_D(E, \Theta, x)}{N U_\circ}, \quad (1)$$

where E and Θ are the energy of the incident ion and the incidence angle with respect to the target surface normal respectively; N and $U_\circ$ are the target density and average surface binding energy and x is the distance between the atom ejection surface and the entrance point of the ion, for backsputtering $x = 0$. $F_D(E, \Theta, x)$ is the depth distribution of ion energy deposition in the target, the energy dependence of which follows that of the *nuclear stopping power* when inelastic energy loss to electronic processes can be neglected[6].

Fabrication of thin films by sputter deposition utilizes the sputter-ejected target atoms as the deposition source. Direct ion beam bombardment of target surfaces can be used, giving rise to the *ion beam deposition* technique[7]. The majority of the sputtering-deposition techniques, however, use plasma discharge in various configurations to provide the ion source. Thus, some carrier gas is necessary for the various *glow-discharge sputtering* techniques. Noble gases are usually used as the carrier gas because of their chemical inertness, although chemically active gases can also be deliberately introduced if compound thin films between the pure elements and these gases are desired, leading to the technique of *reactive sputtering*[8].

When two conducting electrodes are placed in a low-pressure gas and subjected to a DC bias, electrons in the gas drift towards the anode. The presence of electrons in a neutral gas can be due to spontaneous ionization, ionization by cosmic rays, etc. During their course from the cathode to the anode, these electrons will further ionize the neutral gas atoms, provided that the external bias exceeds the ionization potential. In addition to these extra electrons, positive ions so generated drift toward the cathode and upon strike generate secondary electrons. The situation is schematically shown in Fig. 1. The total current is controlled by the combined effect of electron ionization and secondary electron generation at the cathode by positive ions. If we suppose that a fixed number I_0 of primary electrons are generated per unit time, further that α and γ denote the number of ions produced per unit length of electron travel and the number of secondary electrons generated per incident ion onto the cathode, then the total current I is given approximately by[9]

$$I = I_0 \frac{e^{\alpha d}}{1 - \gamma e^{\alpha d}}, \tag{2}$$

where d is the anode cathode separation distance. As the external bias is increased, both α and γ increase[9], and the total current predicted by Equation (2) tends to infinity when $\gamma e^{\alpha d}$ approaches unity. Equation (2) is no longer valid under such conditions and a breakdown is said to have occurred in the gas. Physically, the number of secondary electrons generated at the cathode is sufficient to maintain the discharge and a *self-sustained glow discharge* is obtained. Positive ions strike the cathode surface in a self-sustained glow discharge and cause sputtering of the cathode material. This is usually referred to as the *planar diode sputtering*[8]. Ionization efficiency of a planar diode plasma discharge is low, and relatively high bias (few kilovolts) and high gas pressures (100 mTorr or higher) are required to

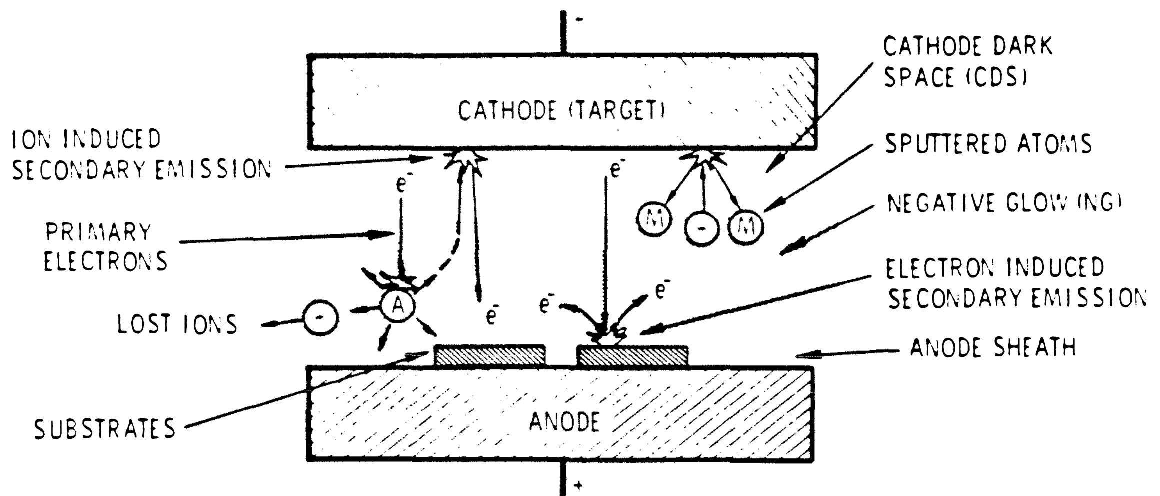

Fig. 2.1 Schematic representation of the plasma during planar diode sputtering. Taken from Ref. 11.

maintain the glow discharge. In order to sputter at lower gas pressures and external bias, various methods have been used to increase the ionization efficiency. The *triode sputtering* technique supplies the plasma region with additional electrons by introducing another electrode, which emits electrons thermionically[8]. Instead of providing more electrons, a more frequently used method to increase ionization efficiency utilizes an added magnetic field to influence the motion of the electrons so that they execute helical instead of straight paths, thus making more ionizing collisions before reaching the anode. Since the electrons drift in the direction of $E \times B$ in the presence of both an electric and a magnetic field[10], axially symmetric magnetic fields are often used such as to allow the $E \times B$ drift current to close on themselves, resulting in various *magnetron sputtering* arrangements[11]. Both the circular and rectangular planar magnetron configurations are shown in Fig. 2. Planar magnetron sputtering is the most frequently used research technique bacause of the simplicity of target construction. The sputtering system we have constructed consists of two circular planar magnetron sputter guns housed in a vacuum chamber capable of reaching a base pressure below 4×10^{-9} Torr. As will be demonstrated, very clean deposition conditions can be achieved with such a setup. In what follows, analysis of each component of this sputter deposition system will be given.

2.2 Vacuum System

A block diagram of the vacuum system is given in Fig. 3. The whole vacuum chamber (Perkin-Elmer Inc.) is metal-sealed with the exception of the top flange, which can either be sealed by a Viton O-ring or a Cu wire-seal. The major pumping system consists of an eight-inch intake cryogenic pump, with two

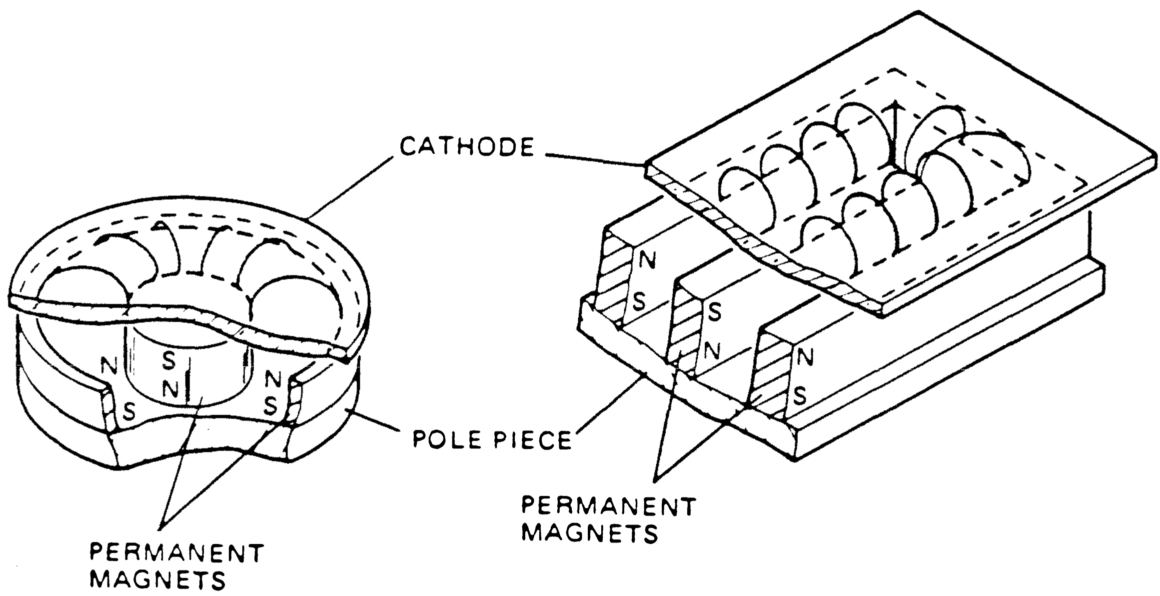

Fig. 2.2 Configuration of circular and rectangular planar magnetron sputtering guns. Taken from Ref. 11.

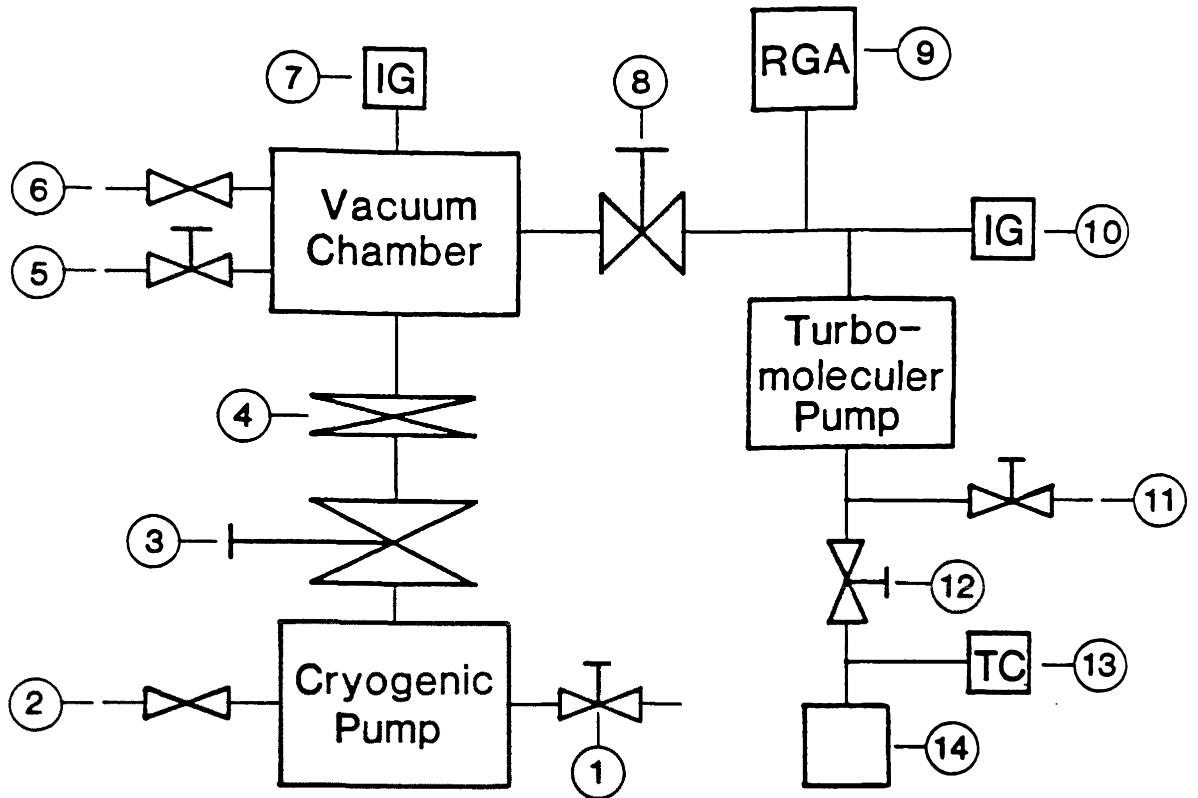

Fig. 2.3 Vacuum system block diagram: (1) N_2 flush inlet valve; (2) pressure relief valve; (3) gate valve; (4) throttle valve; (5) chamber vent valve; (6) piezoelectric leak valve; (7) ion gauge; (8) chamber isolation/differential leak valve; (9) residual gas analyzer; (10) ion gauge; (11) turbo-pump vent valve; (12) mechanical pump isolation valve; (13) thermocouple gauge; (14) mechanical pump.

cryopanels maintained at 77K and 15K, respectively (air-pumping speed 1500 liters/second, Perkin-Elmer Inc.). The cryogenic pump is assisted by an independent turbomolecular pump (air-pumping speed 150 liters/second, Leybold-Heraeus Inc.) backed up by a mechanical pump (Edwards High Vacuum Inc.). This pumping scheme eliminates oil backstreaming from the mechanical pump into the main chamber. During regeneration, the cryogenic pump is isolated from the main chamber by a gate valve and purged by purified N_2 gas through the pressure relief valve until the cryopanels reach room temperature. The whole cryopump system is then pumped by the turbomolecular pump through the chamber to $\sim 10^{-5}$ Torr to achieve thorough desorption of adsorbed molecules on the cryosorption surface. The cryogenic pump system is re-isolated by the gate valve and cooled down; a typical cooling process as monitored by the second cryopanel temperature is shown in Fig. 4. Baking of the main chamber is crucial for obtaining the lowest ultimate base pressure[12]. Baking temperature when all metal seals of the main chamber including the top flange are in place can be as high as 250°C. In actual operation, the chamber surface temperature can be made to range from 100 to 150°C with electrical heating tape when all metal seals are in place. A base pressure below 4×10^{-9} Torr can be reached in this case. When the top flange is sealed with a Viton O-ring, the baking temperature near the top flange should be maintained lower than 100°C and a base pressure of 1 to 4×10^{-8} Torr can be routinely achieved in this case with a total of 24 to 30 hours of pumping time. Ar is used as the carrier gas for sputtering. During the actual deposition process, the main chamber is backfilled with Ar to pressures ranging from 5×10^{-4} to 1.5×10^{-2} Torr. The resultant gas throughput would overload the cryogenic pump, and a throttle valve has to be placed in between the main chamber and the cryopump system to cut down the gas flow. We have designed and built a magnetically coupled butterfly

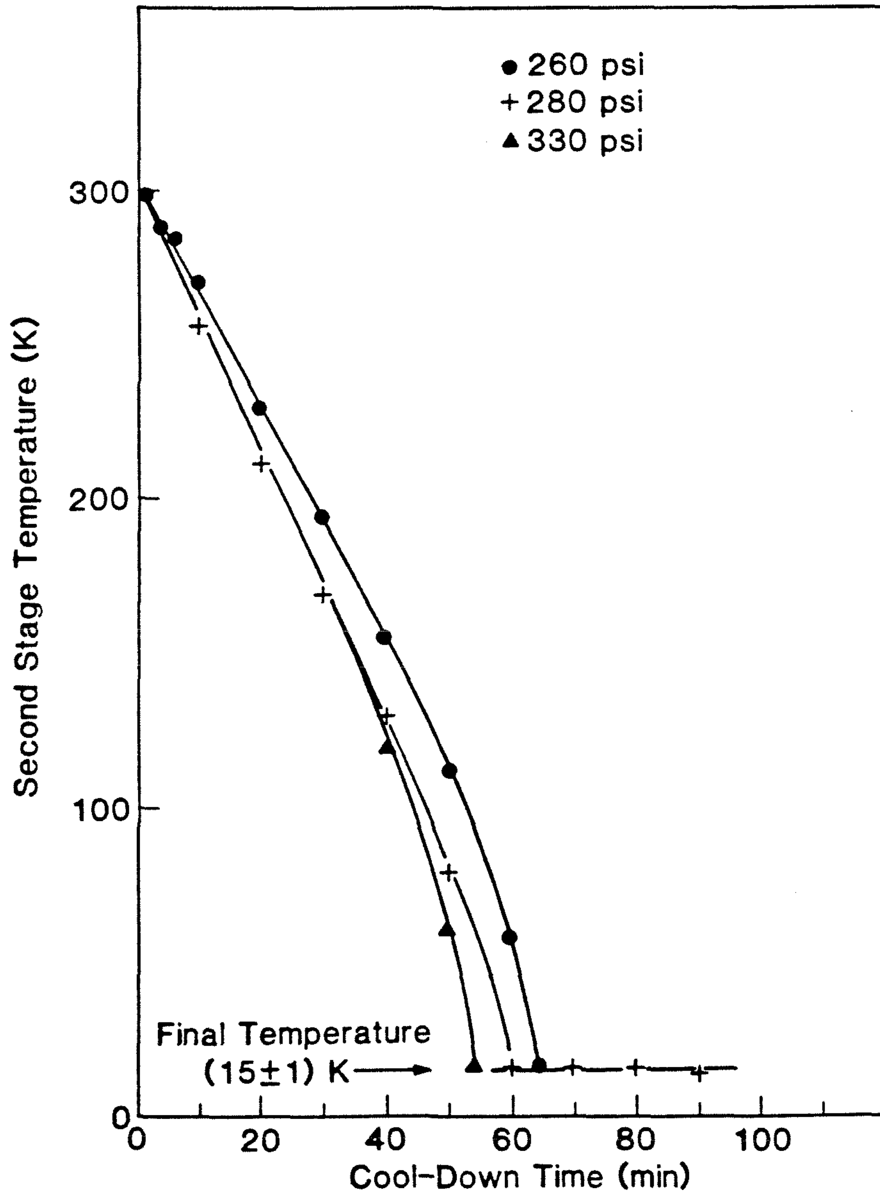

Fig. 2.4 Cryogenic pump regeneration history as monitored by the low temperature sorption stage temperature during cooling.

valve that cuts down the gas throughput during sputtering to an acceptable value when set to the closed position and offers no reduction in conductance from the chamber to the cryopump when placed in the fully open position. In order to achieve a stable deposition during sputtering, the Ar pressure has to be stabilized. The Ar pressure stabilization scheme we have chosen uses a hot cathode ionization gauge, which is able to operate at pressures below 10^{-2} Torr to monitor the Ar pressure while a piezoelectric leak valve interfaced to the ion gauge controller allows more or less Ar into the main chamber according to the ion gauge reading (this whole pressure control package manufactured by Perkin-Elmer Inc.). The Ar pressure in the main chamber can be so maintained to ± 0.2 mTorr. An rf quadrupole mass spectrometer[13] is used to analyze the gas content in the main chamber. Both the residual gas content when the chamber has reached its base pressure and the impurity content during sputtering when Ar is introduced into the main chamber can be analyzed. Since the upper pressure limit for the mass spectrometer to function is 1×10^{-5} Torr, a differential pumping scheme is needed to reduce the pressure in the spectrometer chamber in order to sample the impurity content in the main chamber during sputtering. This is accomplished by the introduction of a multipurpose valve between the main chamber and the spectrometer chamber. This valve has three positions, fully closed to isolate the mass spectrometer and the turbo pump from the main chamber; fully open to allow sampling of the main chamber at its base pressure; and the differential leak position to allow sampling of the main chamber (upper limit of the main chamber total pressure ~ 40 mTorr) during sputtering (the quadrupole mass spectrometer along with all accessories for differential pumping manufactured by Inficon Inc.). The main chamber gas content is reduced in proportion in the spectrometer chamber as long as the conductance between the turbo pump and the spectrometer chamber is throttled down[13], thus

achieving a reliable monitor of the sputter deposition process.

2.3 Sputter Deposition: Operation and Monitoring

Sputter depositions were carried out from two planar magnetron sputter guns installed in the vacuum system (US Gun Inc.). Conducting materials to be sputtered such as metals or alloys are placed on top of the sputter guns biased negatively with respect to the substrate platform, which is grounded. These two guns were biased externally from two DC power supplies (1.7 kilowatt, Sputtered Films Inc.). Typical Ar pressures in the sputtering chamber are 3 to 15 mTorr. Typical voltage-current characteristics of both sputtering sources are shown in Fig. 5. The maximum power input into the sputtering sources is limited by the effectiveness of the target cooling, which, because of the poor thermal link between the water-cooled gun top and the actual target is limited to below 500 watts. The minimum currents and voltages required to maintain a stable plasma discharge range from 0.05 to 0.1 amperes and 50 to 100 volts, which increases with decreasing Ar pressure, although very little material is sputtered at this lower limit, and actual depositions are always carried out at much higher power. Since the $E \times B$ electron drift current is shaped like a ring over the target in a circular planar magnetron gun, the plasma density over the target surface is consequently nonuniform. Sputtered material originates from the regions of high plasma density and the sputter erosion of the target also posseses a ring shape. Thickness distribution of the resultant thin film condensed on the substrate agrees with calculated results, assuming a superposition of cosine emission from the whole erosion area[3]. The substrate platform is placed 12 to 15 centimeters away from the targets. This distance is found to be

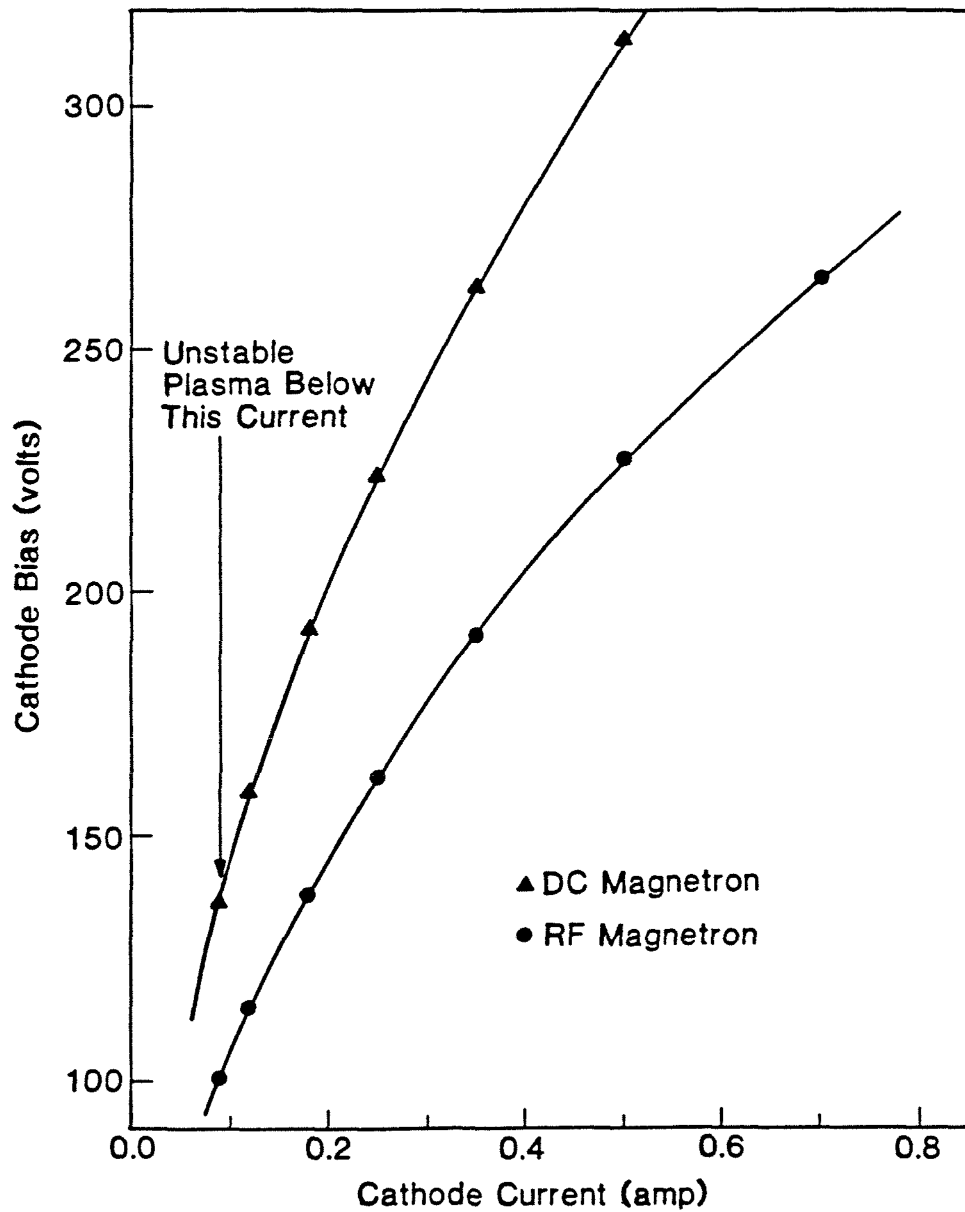

Fig. 2.5 Typical current-voltage characteristics of planar magnetron sputter guns while sputtering Cu at 6 mTorr of Ar.

a good compromise between reasonable deposition rates and minimal influence of the cathode plasma region on the condensing film such as substrate heating during deposition. The actual deposition rates are measured in real time by two separate quartz crystal oscillators (Inficon Inc.), each mounted directly on top of the substrate overlooking the sputter guns through a hole in the substrate. Calibration of the crystal oscillators is necessary since their positions do not coincide with the actual substrates. The calibration can be accomplished by several methods such as Rutherford backscattering spectrometry, direct massing of a deposited film, or a direct measurement of the film thickness (in the range of a few thousand angstroms) by means of a mechanical stylus. Results from calibrations via these different methods can be used to check their consistency. In using the backscattering method, the actual film thickness (~ 500 Å) is measured directly and compared to the registered value from the thickness monitor. Direct massing of the film (thickness $\sim 1\mu$m) deposited on a prescribed area of a substrate can also be used to determine the actual film thickness. Both methods have been used for the calibration of our crystal oscillators with consistent results obtained. Over a 5- centimeter distance from the center of the sputter guns, the film thickness has been found not to vary by more than 5%. The sputtering yield for most metals is effectively a constant in the usual gun operating range; thus, the target erosion rate or the deposition rate is proportional to the cathode current, as shown in Fig. 6. The deposition rate versus power is consequently nonlinear. Multilayered thin film diffusion couples consisting of alternating layers of two pure elements are made by simultaneously sputtering two elemental targets from two separate sputter guns while alternating the sample substrate over each individual sputter gun. Fig. 7. shows the result of x-ray small angle scattering from the artificial composition modulations of an Fe/V multilayer fabricated in our deposition system with nominal individual elemental layer thick-

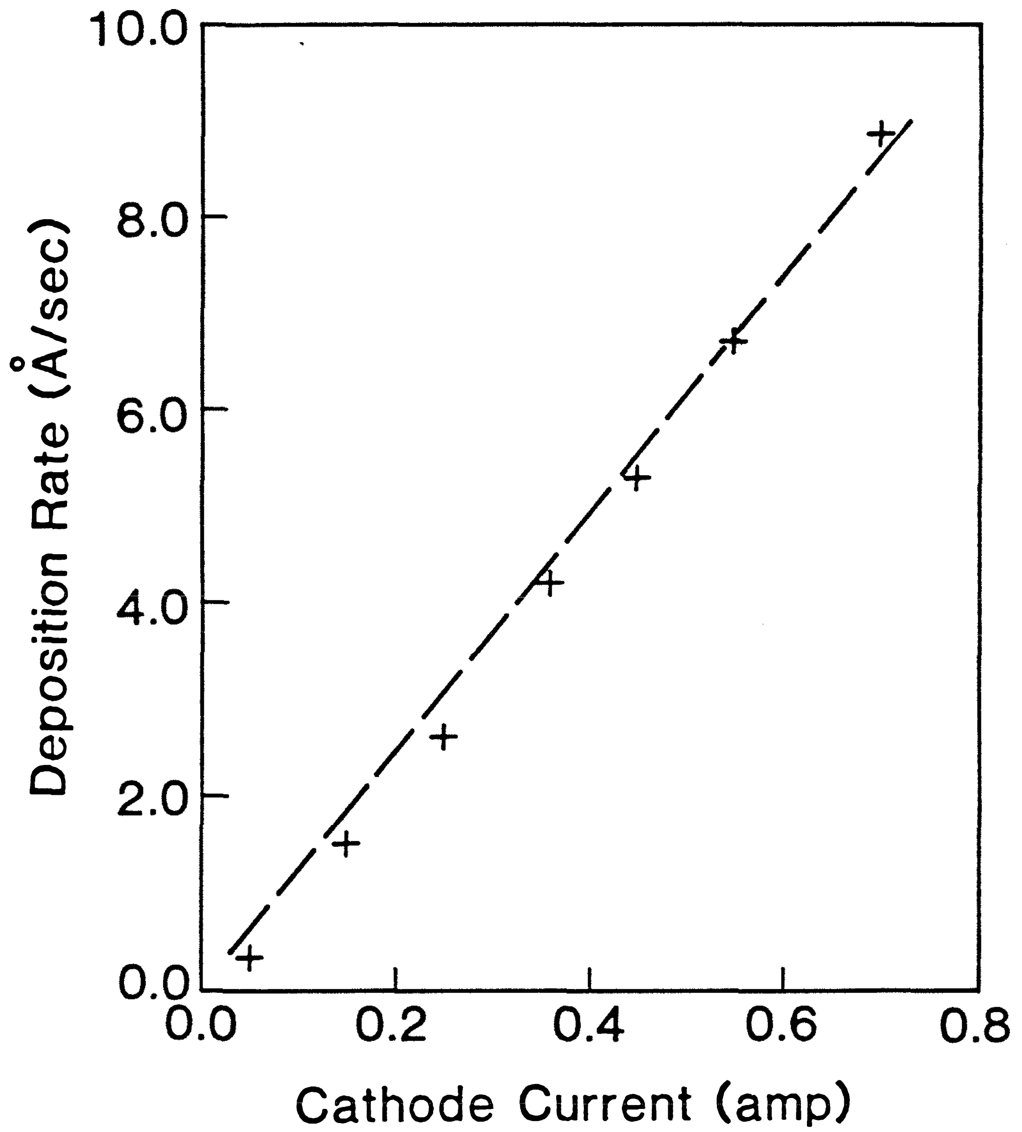

Fig. 2.6 Deposition rate of pure Cu at 9 mTorr of Ar vs. cathode current.

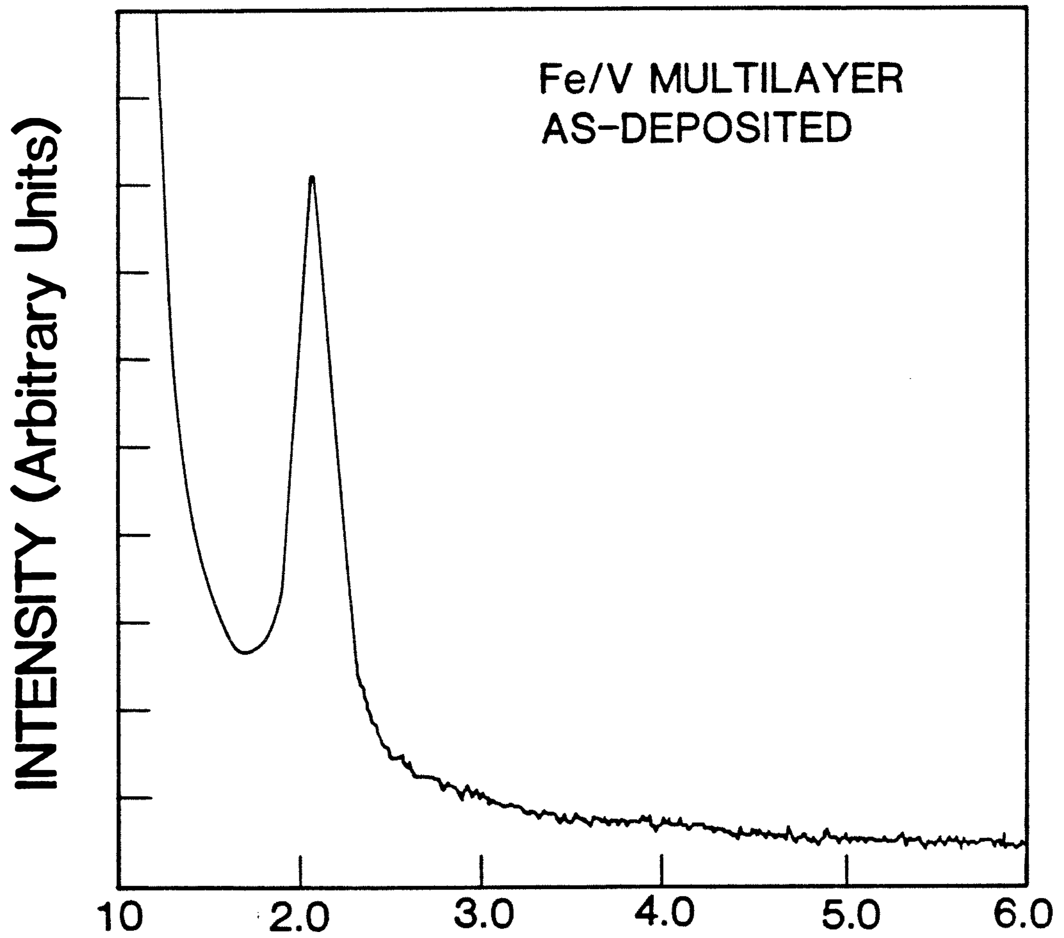

Fig. 2.7 X-ray small angle scattering from an Fe/V multilayer with nominal composition modulation wavelength of 40Å.

nesses of 20 Å as determined by the crystal oscillators after calibration, in excellent agreement with the measured modulation wavelength from x-ray diffraction of 42Å, indicating the ability of our sputtering system for synthesizing very accurately tailored compositionally modulated thin films. The absence of higher order diffraction satellites in Fig. 7, however, signals some interfacial roughness or interlayer mixing between the elemental layers of Fe and V.

Impurity incorporation into the sputter-deposited thin films is of major concern. It is the common impression that sputter- depostion is a "dirty" process. However, the precise meaning of "dirty" requires a more careful analysis. The introduction of Ar carrier gas into the main chamber during sputtering introduces along with it reactive gas impurities such as O_2 and H_2. In order to keep the impurity level in the Ar gas to a minimum, ultrahigh purity ($99.999+\%$) Ar is made to pass through a pure Ti metal sponge heated to and maintained at 800°C (Centorr Inc.) before entering the main chamber. Table 1 shows typical main chamber residual gas contents as measured by the mass spectrometer when the system has reached its base pressure. Table 1 shows also the typical residual gas contents in the main chamber during sputtering deposition at an Ar pressure of 6 mTorr. It is to be emphasized that the residual gas contents in the main chamber during sputtering is obtained by converting the sampled gas contents in the differentially pumped spectrometer chamber without subtracting the background contribution (i.e., the residual gas content measured when the system is at its base pressure). Thus, the impurity gas level so measured represents an upper limit to the actual gas content in the main chamber during sputtering. The results indicate that while the Ar pressure during sputtering is in the mTorr range, the partial pressures of the

TABLE 2.1 Sputtering chamber residual gas content.

	Background (Torr)	Background with Ar (Torr)	Background (sputtering Ti) (Torr)
H_2O	2×10^{-8}	6×10^{-6}	4×10^{-7}
N_2	2×10^{-9}	3×10^{-6}	1×10^{-7}
H_2	7×10^{-10}	4×10^{-6}	3×10^{-7}
O_2	7×10^{-10}	unreadable	unreadable
Ar	2×10^{-10}	6×10^{-3}	6×10^{-3}

Table 2.1 Residual gas content in the sputtering chamber as sampled by the residual gas analyzer. Residual gas contents after introducing Ar into the chamber are monitored both before and during sputtering of a pure Ti target at 6 mTorr of Ar.

TABLE 2.2 Low pressure properties of air.

Pressure (Torr)	n (m^{-3})	λ (m)	Γ (m^2/sec)
760	2.5×10^{25}	6.5×10^{-8}	2.8×10^{27}
7.5×10^{-3}	2.5×10^{20}	6.6×10^{-3}	2.8×10^{22}
7.5×10^{-6}	2.5×10^{17}	6.64	2.8×10^{19}
7.5×10^{-8}	2.5×10^{15}	664	2.8×10^{17}
7.5×10^{-10}	2.5×10^{13}	6.6×10^{4}	2.8×10^{15}

Table 2.2 Particle density, n; mean-free path, λ; particle flux on a surface, Γ. $T = 22°$C. Taken from Ref. 14.

predominant impurity gases such as H_2, O_2, and N_2 are generally in the 10^{-6} Torr range or below. Table 2 lists the mean-free path and expected number of molecules incident upon unit-area per unit-time calculated for air at room temperature[14]. At a pressure of 10^{-3} Torr, the incident molecules upon the condensing film surface amount to about one thousand monolayers per second (assuming one monolayer amounts to $\sim 10^{15}$ molecules per square centimeter). Thus, our first conclusion is that carrier gas incoporation into the resulting thin film is an unavoidable side effect inherent to all glow- discharge sputtering technique. The actual Ar incoporation is usually in the 1% level or lower due to the chemical inertness of Ar, hence the low sticking probability[15]. At a pressure of 10^{-6} Torr, the incident molecules upon the condensing film still amount to about one monolayer per second. Thus, at first sight, contamination of the condensing thin films by reactive gas impurities in the 10^{-6} Torr level would reach 10 to 50% (assuming a sticking coefficient of unity) with typical deposition rate of pure metals ranges from one to five monolayers per second (3 to 15 Å/sec). However, the rate of incidence of the reactive impurity gases onto the substrate surface is greatly reduced by the presence of the Ar gas. Since the mean-free path of gas molecules is inversely proportional to pressure, assuming equal scattering cross sections for all gas species in the main chamber, the rate of impurity gas i incident upon the substrate is, roughly speaking, reduced in the presence of Ar by a factor of P_i/P_{Ar} where P_i and P_{Ar} are the partial pressures of gas i and Ar, respectively. Thus, the effective impurity level during sputtering as measured by the rate of impurity gas incident onto the substrate can be as low as 10^{-9} Torr! Such impurity levels rival those found in conventional e-beam evaporation, although it is still inferior to techniques such as semiconductor or metal MBE depositions.

2.4 Summary

It has been only until relatively recently that synthesis of thin films by sputter deposition has become competitive with the more established vapor deposition techniques such as the various evaporation techniques. The principal shortcoming, which is the commonly perceived "dirtiness" associated with sputter deposition, has been increasingly overcome by better vacuum practice and better gas-handling capabilities. The inherent easier control and versatility of the sputter deposition technique will probably warrant more usage and further developement of this technique. We hope the succesful construction of our rather simple sputter deposition system will serve as one such example.

2.5 References

1. *Handbook of Thin Film Technology*, edited by L. I. Maissel and R. Glang (McGraw-Hill, New York, 1970).
2. *Molecular Beam Epitaxy*, edited by B. R. Pamplin (Pergamon Press, Oxford, 1980).
3. G. K. Wehner and G. S. Anderson, in *Handbook of Thin Film Technology*, edited by L. I. Maissel and R. Glang, Ch. 3 (McGraw-Hill, New York, 1970).
4. P. D. Townsend, J. C. Kelly, and N. E. W. Hartley, *Ion Implantation, Sputtering and Their Applications* (Academic Press, London, 1976).
5. H. H. Anderson and H. L. Bay, in *Sputtering by Particle Bombardment I*, edited by R. Behrisch, Ch. 4 (Springer- Verlag, Berlin, 1981).
6. P. Sigmund, Ch. 2, *ibid.*
7. J. M. E. Harper, in *Thin Film Processes*, edited by J. L. Vossen and W. Kern, Ch. 2.5 (Academic Press, Orlando, 1978).
8. J. L. Vossen and J. J. Cuomo, Ch. 2.1, *ibid.*
9. L. Maissel, in *Handbook of Thin Film Technology*, edited by L. I. Maissel and R. Glang, Ch. 4 (McGraw-Hill, New York, 1970).
10. F. F. Chen, *Introduction to Plasma Physics and Controlled Fusion*, Ch. 2 (Plenum Press, New York, 1974).
11. R. K. Waits, in *Thin Film Processes*, edited by J. L. Vossen and W. Kern, Ch. 2.4 (Academic Press, Orlando, 1978).
12. J. F. O'Hanlon, *A User's Guide to Vacuum Technology*, Ch. 6 (Wiley, New York, 1980).

13. J. F. O'Hanlon, Ch. 4, *ibid.*

14. J. F. O'Hanlon, Ch. 2, *ibid.*

15. H. F. Winters, E. Kay, J. Appl. Phys. **38**, 3928 (1967).

Chapter 3

Solid-State Amorphization of Planar Binary Diffusion Couples: Thermodynamics and Growth Kinetics

A bilayer or multilayer planar, binary, thin film diffusion couple consisting of two pure elements is, by construction, not in thermodynamic equilibrium. The overall free energy of the system can be decreased by interdiffusion of the pure elements until the system consists of a single equilibrium crystalline phase or a combination of such phases according to equilibrium thermodynamics. The process of reaching the global thermodynamic equilibrium, however, often involves intermediate steps where metastable phases, because of their competitive kinetics, are produced. The present chapter concentrates on the thermodynamics and kinetics of the formation of amorphous NiZr alloys by solid- state interdiffusion of sputter-deposited polycrystalline binary diffusion couples consisting of pure Ni and Zr.

3.1 Equilibrium phase diagrams and free energy diagrams

Equilibrium thermodynamic information for a binary system are summarized in the corresponding equilibrium binary phase diagram[1]. The final state reached by a binary diffusion couple consisting of two pure elements is always given by the equlibrium phase diagram. In a binary system where multiple compounds exist, the phase diagram does not, however, predict the *sequence of formation* of

these various compounds. A binary phase diagram can be derived if the dependence of the free energies of the terminal solid solutions and various compounds on temperature and composition is known. A schematic example is given in Fig. 1, where the derived phase diagram contains a congruently melting compound together with two terminal solid solutions. Strictly speaking, free energy functions are defined only for equilibrium phases. However, oftentimes free energies can also be defined for various metastable phases[2]. A knowledge of the free energy functions of all phases, stable or metastable, determines whether the formation of a particular phase is thermodynamically possible. Thermodynamic data of pure elements are available from which the free energies of pure elements can be calculated[3]. Experimentally determined equilibrium phase diagrams together with some thermodynamic modeling are often used to determine the free energy functions of equilibrium phases[4]. Amorphous alloys are usually modeled as an extension of the liquid state down to the undercooled regime. Various extrapolation schemes are used to estimate the free energy of an amorphous alloy[5]. Direct measurement of thermodynamic data on metastable alloys including amorphous alloys is at best scarce.

3.2 Planar Growth Kinetics of a Single Compound Interlayer

Growth of a particular phase is partially characterized by the morphology, i.e., whether the growth is three-dimensional (spherelike), two-dimensional (island growth) or one-dimensional (layered growth). Phase formation in planar binary elemental diffusion couples often proceeds by planar one-dimensional growth starting at the original elemental interface[6]. In this case, analysis of the growth kinetics of a particular compound is equivalent to knowing the compound interlayer

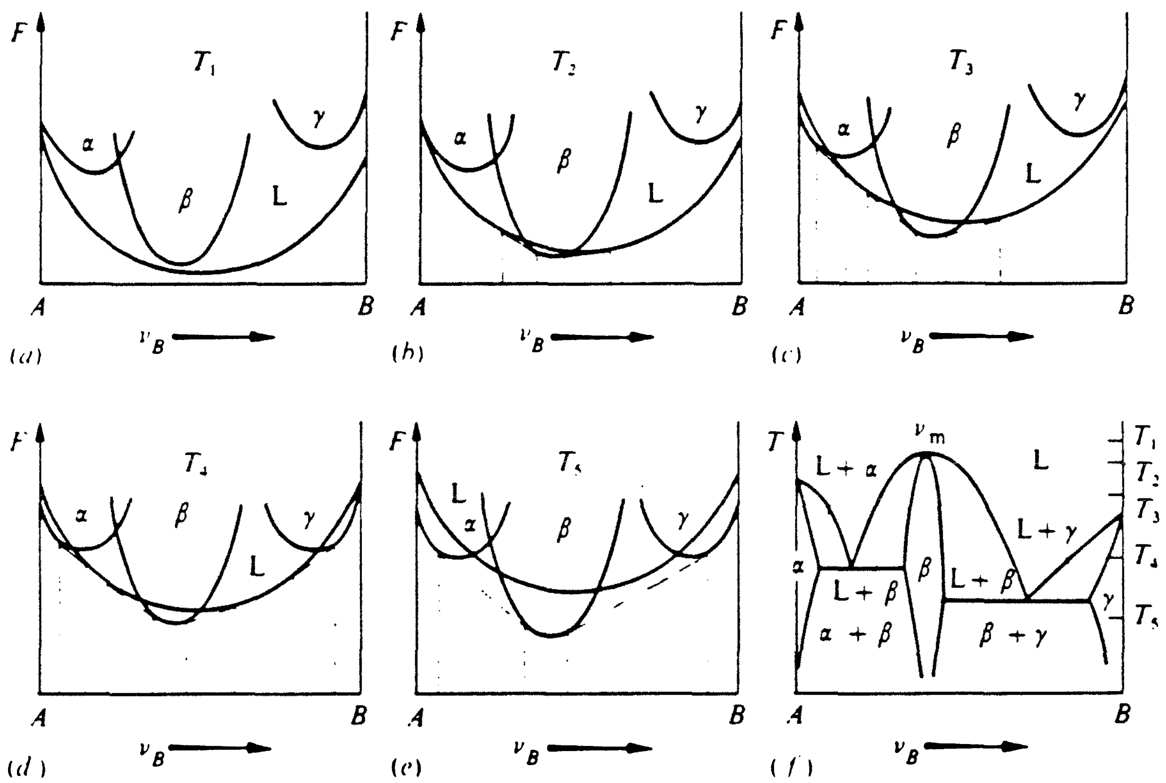

Fig. 3.1 Free energy functions of various phases and the A-B phase diagram derived from them. Taken from Ref. 1.

thickness as a function of time. Several general models of planar growth kinetics exist in the literature[7,8,9]. In our treatment below, we present a steady-state single compound layer growth model, which follows in essence the treatment due to Gosele and Tu[9]. This model, although simplified, offers the essential physical picture necessary to understand such growth processes.

It is assumed that compound β forms and grows between two saturated phases α and γ (e.g., the two saturated terminal solid solutions). The hypothetical free energy diagram together with the schematic concentration profile through the diffusion couple is shown in Fig. 2. The α/β and β/γ interfaces move because of interdiffusion and the thickness of the β phase grows with time. In general, a set of coupled differential equations are needed to solve this moving boundary diffusion problem[10]. Analytical solutions can be obtained with the following simplifying assumptions. The *steady-state assumption* approximates the concentration profile in the β layer at any instant as the steady-state concentration profile with the moving α/β and β/γ boundaries fixed in their positions at that instant[11]. Thus, the A atom diffusional flux should be a constant through the β compound layer. The steady-state approximation therefore dictates that

$$\tilde{D}_\beta \frac{\partial C_A}{\partial x} = constant, \tag{1}$$

where $\tilde{D}_\beta$ is the interdiffusion constant through the β compound layer. If we further assume that the variation of this interdiffusion constant with concentration in the β concentration range can be neglected, then Equation (1) is equivalent to the condition that the concentration profile through the β layer is linear. Such a condition is implied in the concentration profile depicted in Fig. 2 and the A atom

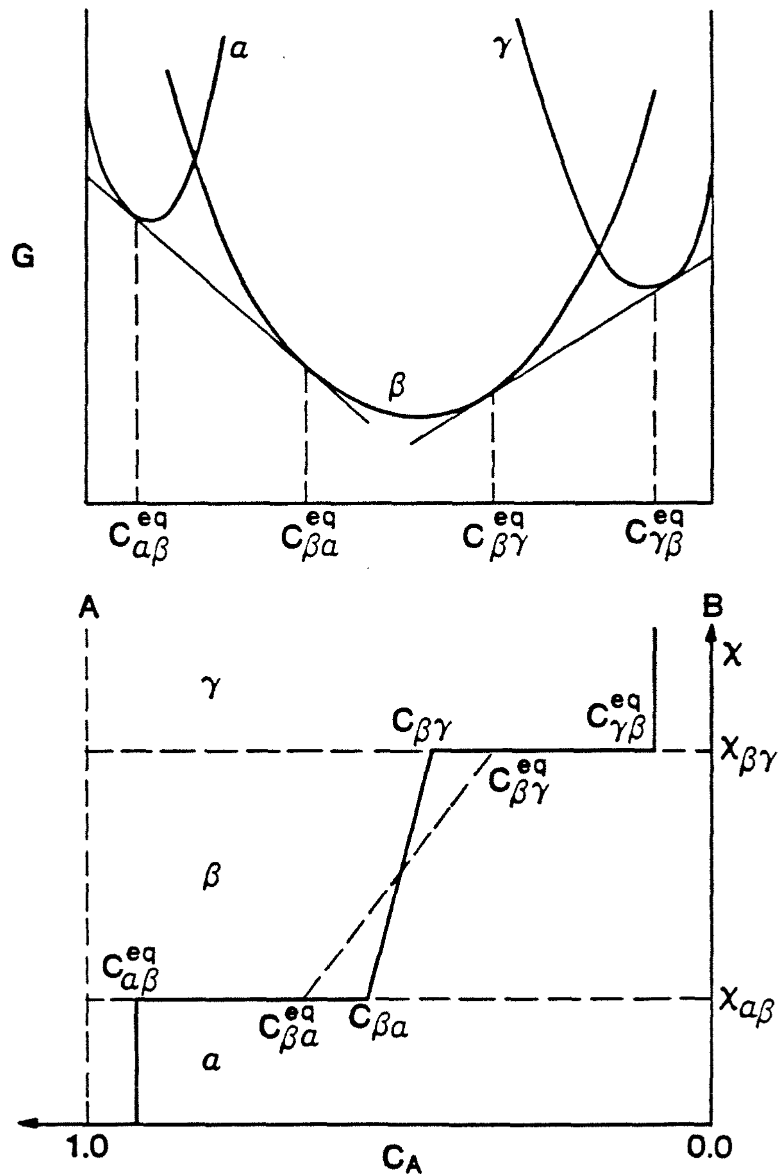

Fig. 3.2 Schematic illustration of growth of a single compound interlayer in a planar binary diffusion couple. Hypothetical free energy diagram and the concentration profile.

diffusional flux through the β interlayer can be written in this case as

$$J_\beta^A = -\tilde{D}_\beta \frac{C_{\beta\gamma} - C_{\beta\alpha}}{x_\beta}. \tag{2}$$

The *interface motion* is assumed to be driven by diffusional fluxes into and leaving this interface. For the two interfaces depicted in Fig. 2, we have

$$(C_{\alpha\beta}^{eq} - C_{\beta\alpha})\frac{dx_{\alpha\beta}}{dt} = J_{\alpha\beta} - J_{\beta\alpha} \tag{3.1}$$

$$(C_{\beta\gamma} - C_{\gamma\beta}^{eq})\frac{dx_{\beta\gamma}}{dt} = J_{\beta\gamma} - J_{\gamma\beta}, \tag{3.2}$$

where all concentrations and fluxes refer to those of the A atom. $J_{\alpha\beta}$ and $J_{\beta\alpha}$ denote the flux from the α side into the α/β interface and the flux into the β phase from the α/β interface, respectively; similar interpretations hold for the fluxes $J_{\beta\gamma}$ and $J_{\gamma\beta}$. Since we have assumed that the terminal phases α and γ are saturated (i.e., with constant compositions determined by the equilibrium conditions), $J_{\alpha\beta}$ and $J_{\gamma\beta}$ are consequently zero. The steady-state condition can be used to further simplify the situation since under this assumption

$$J_{\beta\alpha} = J_{\beta\gamma} = J_\beta^A, \tag{4}$$

where J_β^A is given by Equation (2). Thus, Equation (3) can be rewritten as

$$(C_{\alpha\beta}^{eq} - C_{\beta\alpha})\frac{dx_{\alpha\beta}}{dt} = -J_\beta^A \tag{5.1}$$

$$(C_{\beta\gamma} - C_{\gamma\beta}^{eq})\frac{dx_{\beta\gamma}}{dt} = J_\beta^A. \tag{5.2}$$

The condition of *interface quasi-equilibrium* is implicitly assumed; i.e., the deviation from thermodynamic equlibrium at the interfaces is assumed to be small enough to justify a linear response of the interfaces to the degree of deviation from equilibrium. Specifically, the notion of *interfacial reaction barrier* is introduced to relate the

A atom flux at the interfaces to the interface concentration deviations from the equilibrium values

$$J_{\beta\alpha} = \kappa_{\beta\alpha}(C^{eq}_{\beta\alpha} - C_{\beta\alpha}) \tag{6.1}$$

$$J_{\beta\gamma} = \kappa_{\beta\gamma}(C_{\beta\gamma} - C^{eq}_{\beta\gamma}), \tag{6.2}$$

where $\kappa_{\beta\alpha}$ and $\kappa_{\beta\gamma}$ are the mobilities for the two interfaces in the diffusion couple. Combining Equations (6) with (4) and (2), it can easily be derived that

$$J^A_\beta = \Delta C^{eq}_\beta \tilde{D}_\beta \frac{1}{x_\beta + \tilde{D}_\beta / \kappa^{eff}_\beta}, \tag{7}$$

where $\Delta C^{eq}_\beta = C^{eq}_{\beta\alpha} - C^{eq}_{\beta\gamma}$ is the equilibrium concentration difference accross the β compound layer, and κ^{eff}_β is the *effective interfacial reaction barrier* for the β compound layer given by $1/\kappa^{eff}_\beta = 1/\kappa_{\beta\alpha} + 1/\kappa_{\beta\gamma}$. Since $x_\beta = x_{\beta\gamma} - x_{\alpha\beta}$, Equation (5) can then be used to give the desired growth kinetics

$$\frac{dx_\beta}{dt} = G_\beta J^A_\beta, \tag{8}$$

where G_β is a constant determined by the concentrations of the three phases involved[9]. It is clear from Equation (7) that there exists a characteristic length $x^*_\beta = \tilde{D}_\beta / \kappa^{eff}_\beta$ in the growth of the β compound interlayer such that the β interlayer thickness is proportional either to time t, or to the square root of time $t^{1/2}$, depending on whether the interlayer thickness is substantially below or above this characteristic length; i.e.,

$$\frac{dx_\beta}{dt} = G_\beta \Delta C^{eq}_\beta \kappa^{eff}_\beta, \quad x_\beta \ll x^*_\beta \tag{9.1}$$

$$\frac{dx_\beta}{dt} = G_\beta \Delta C^{eq}_\beta \frac{\tilde{D}_\beta}{x_\beta}, \quad x_\beta \gg x^*_\beta. \tag{9.2}$$

Experimental determination of the growth kinetics of a single compound layer most often involves the determination of the compound interlayer thickness as a function

of annealing time. The interdiffusion constant or the interfacial barrier constant can then be extracted from experimental data using kinetic models such as Equation (9). Such a phenomenological description of the interdiffusion process may break down in the limit of very small interlayer thicknesses[12].

3.3 Growth of the amorphous interlayer: X-ray and Resistivity Measurements

X-ray diffraction is commonly used to detect the presence of various solid phases. We have used x-ray diffraction in the Bragg-Brentano geometry to follow the process of amorphous phase formation in Ni-Zr system[13]. Samples studied in this work were prepared by a dc magnetron sputtering technique described previously[14]. Each sample contained a total of about 25 layers with individual layer thicknesses around 500Å. Samples were prepared on both glass and Be substrates. Sample heat treatments were carried out in a flowing He gas furnace. A liquid nitrogen trap and a Ti gettering furnace for He assured minimal oxygen contamination. Similar results were also obtained when the annealing was carried out in a vacuum furnace with pressure kept below 5×10^{-7} Torr. The x-ray measurements were performed on a Philips vertical diffractometer using Cu $K\alpha$ radiation.

The x-ray diffraction pattern of an as-deposited Ni/Zr multilayer is shown at the top of Fig. 3. This sample was prepared under an Ar sputtering pressure of 15 mTorr. It is clear that the Ni and Zr layers are both highly textured with the film growth normal to close-packed planes, i.e., (002) in Zr and (111) in

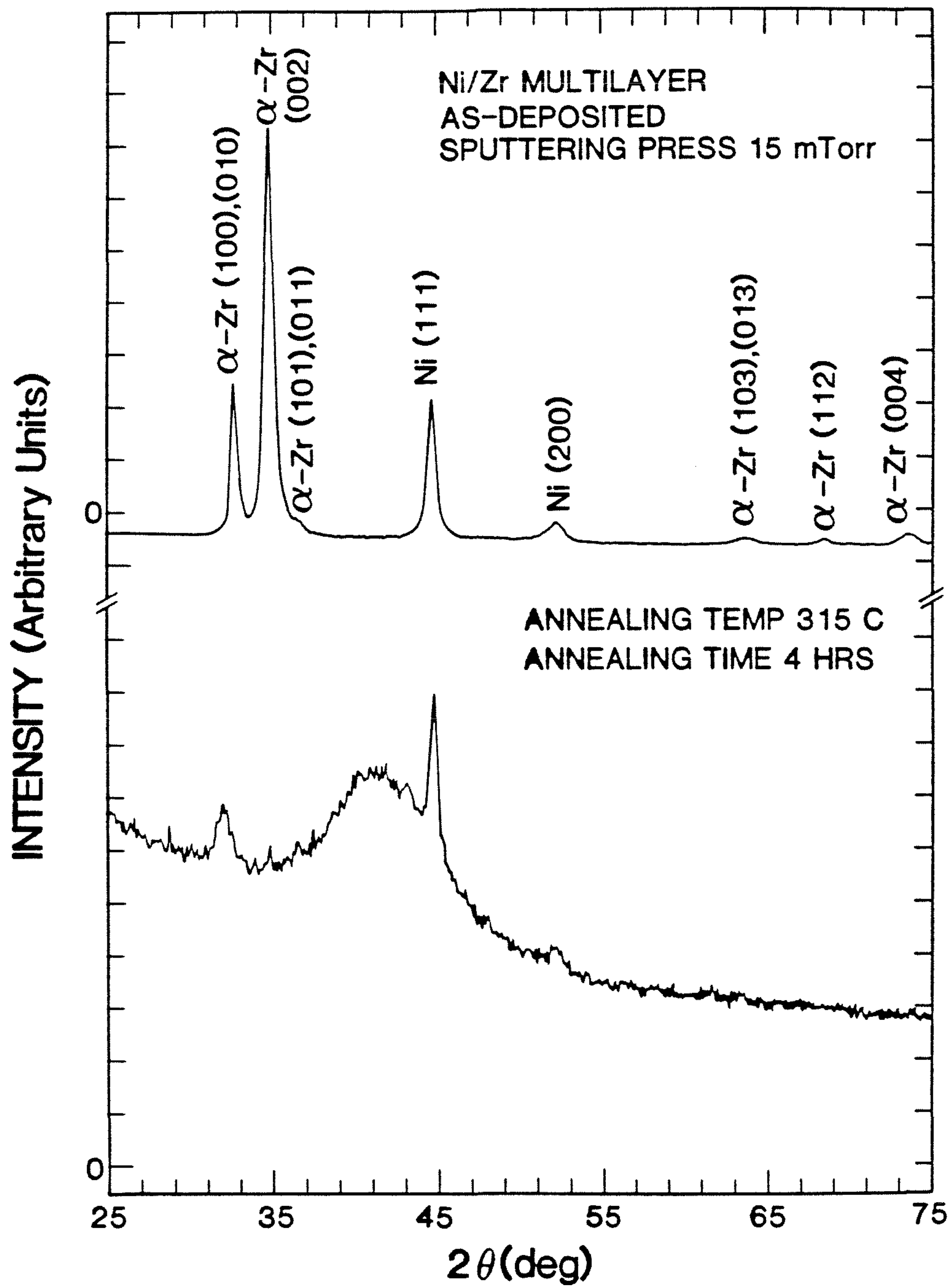

Fig. 3.3 X-ray diffraction patterns of as- deposited (top) and reacted (bottom) Ni/Zr multilayers (see text).

Ni. This texturing effect is commonly observed in sputtered-deposited thin films[15]. The bottom half of Fig. 3 shows the result of a four-hour anneal at 315°C. It can be seen that the sharp Bragg peaks of the as-deposited films have been greatly reduced in intensity and a broad band has appeared indicating the presence of an amorphous phase. It should be noted that the initially very strong $\alpha-$Zr (002) peak has essentially disappeared, while the initially weaker $\alpha-$Zr (100) peak has become the dominant Zr peak. While the as- deposited films are smooth and flat, the reacted films often buckle from the substrate. This effect will be discussed later. A rough measure of the growth kinetics of the amorphous NiZr alloy can be obtained by a detailed examination of the x-ray diffraction data. We have focussed on one set of identically prepared films. Because the amorphous NiZr alloy is the only new phase observed throughout the annealing process, its growth can be monitored by the consumption of elemental Ni and Zr, which in turn is proportional to the decrease in the Ni and Zr integrated x-ray Bragg peak intensities, assuming that no change in film texture occurs during the course of annealing[16]. The results of these measurements are shown in Fig. 4 for two films, one annealed at 250°C and the other at 315°C. In both cases the total Bragg peak intensities of Ni and Zr have been normalized to their initial as-deposited values. The slight increase in the Ni total peak intensities following the first 30- minute anneal at 250°C is most likely due to recrystallization of some Ni crystallites. There is no evidence for further recrystallization during subsequent anneals. At both temperatures an initial decrease in the Ni and Zr total peak intensities is followed by a region of less rapid decrease. In addition, the 250°C annealing data exhibit a break in the peak intensity curve between these two regions. This break is the result of a smaller total scattering area due to the buckling of the film from the substrate. A similar effect is not observed in the case of the 315°C anneal because the film buckling has already

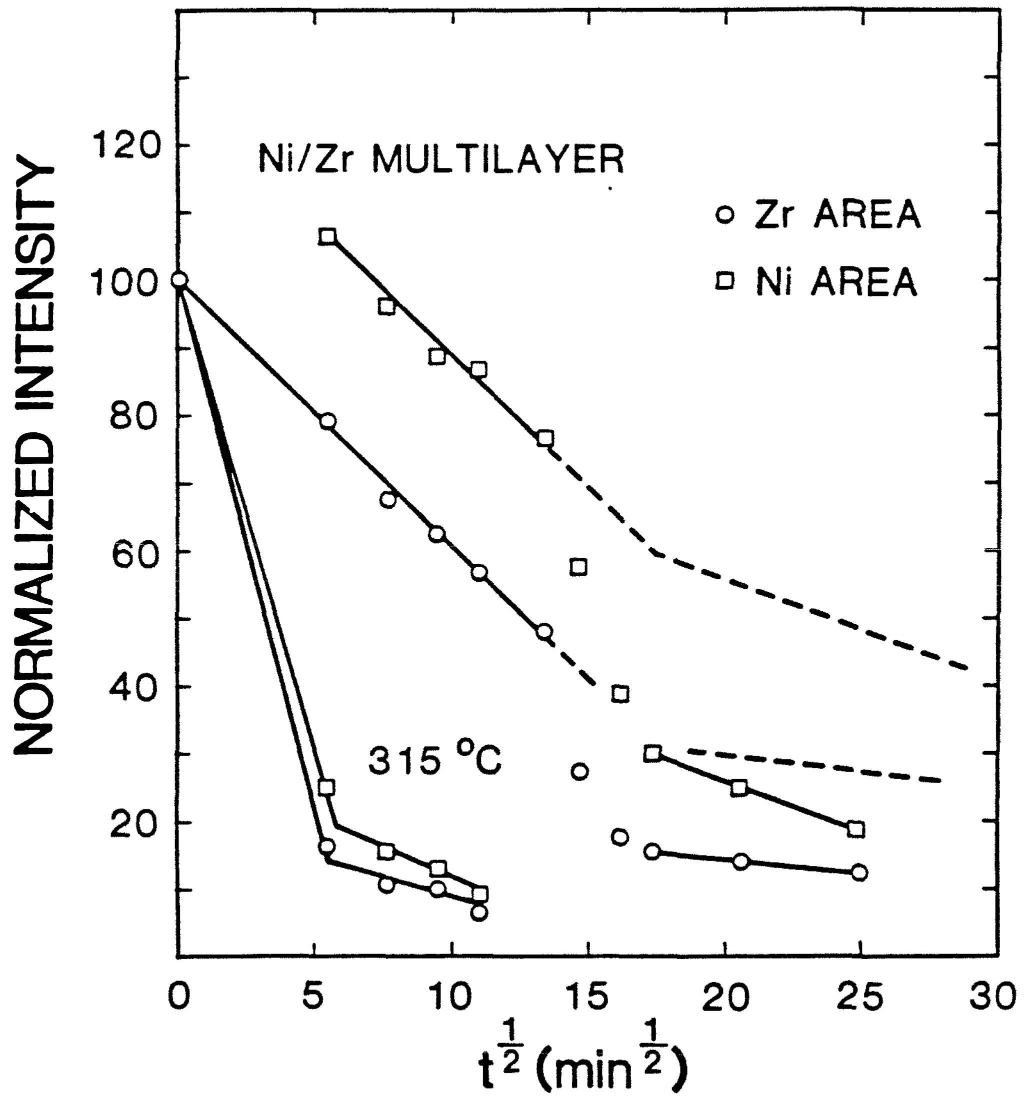

Fig. 3.4 Normalized Ni and Zr integrated Bragg peak intensities vs. $t^{1/2}$ at 250°C and 315°C (see text).

occurred during the first 30-minute annealing period. The fact that the consumption rate of the crystalline Ni and Zr follows a $t^{1/2}$ time dependence, as evidenced in Fig. 4, implies a diffusion rather than an interface-limited growth process of the amorphous phase. The rate of consumption of the elemental materials can be related to the interdiffusion constant of the amorphous phase $\tilde{D}_{am}$. Based on the respective slopes of the data shown in Fig. 4, we estimate $\tilde{D}_{am}(250°C) = 2 \times 10^{-19} m^2/sec$ and $\tilde{D}_{am}(315°C) = 4 \times 10^{-18} m^2/sec$ before the buckling of the film occurred. The activation energy for this interdiffusion constant is thus estimated to be 1.2eV. Ni is a fast diffuser in crystalline $\alpha-$Zr[17]. It is important to note that our estimated interdiffusion constant is at least two orders of magnitude less than that of Ni tracer diffusion in $\alpha-$Zr extrapolated to the reaction temperature[17]. Corresponding to the decrease in the Ni and Zr integrated peak intensities shown in Fig. 4, there is also a shift in the Bragg peak positions from their as-deposited values, which can be seen clearly in Fig. 5. The measured shift in d-spacings as a function of time is displayed in Fig. 6. The d-spacings measured in reflection correspond to lattice planes parallel to the sample surface. Both the Zr (100) and (002) lines exhibit a rapid initial increase in their d-spacings, followed by a decrease. The Ni (111) line position, on the other hand, remains essentially unchanged throughout the entire annealing period. The dilation of the Zr unit cell in a direction perpendicular to the film surface can arise because of an in-plane compressive stress at the Zr/amorphous interfaces. Such an interpretation will require a contraction of in-plane Zr lattice spacings and can be verified by transmission x-ray measurements. We have chosen to use Be substrates for this purpose due to their low x-ray absorption. The results of these measurements are shown in the insert of Fig. 6. It can be seen that the Zr cell dilation perpendicular to the sample surface is accompanied by a contraction parallel to the film surface. The effect of amorphous interlayer growth is therefore

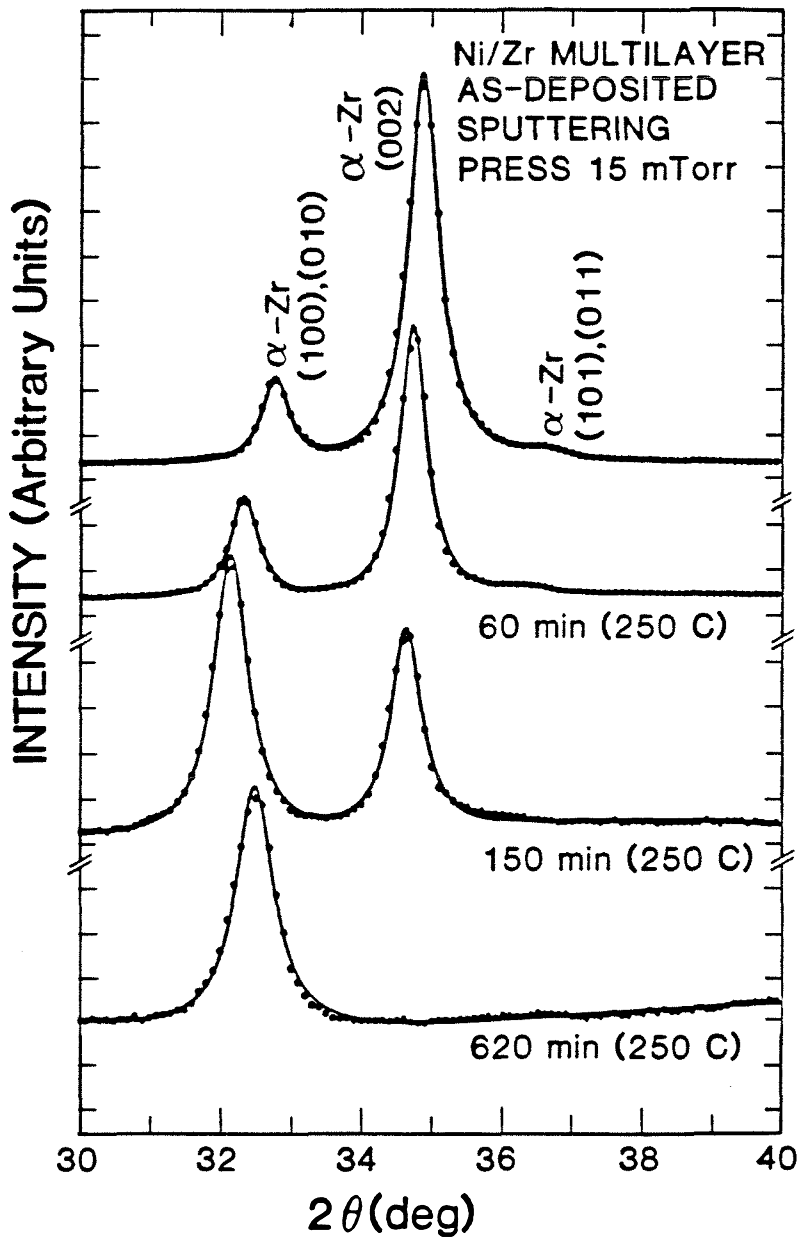

Fig. 3.5 Shift of Zr Bragg peaks as a function of reaction time at 250°C.

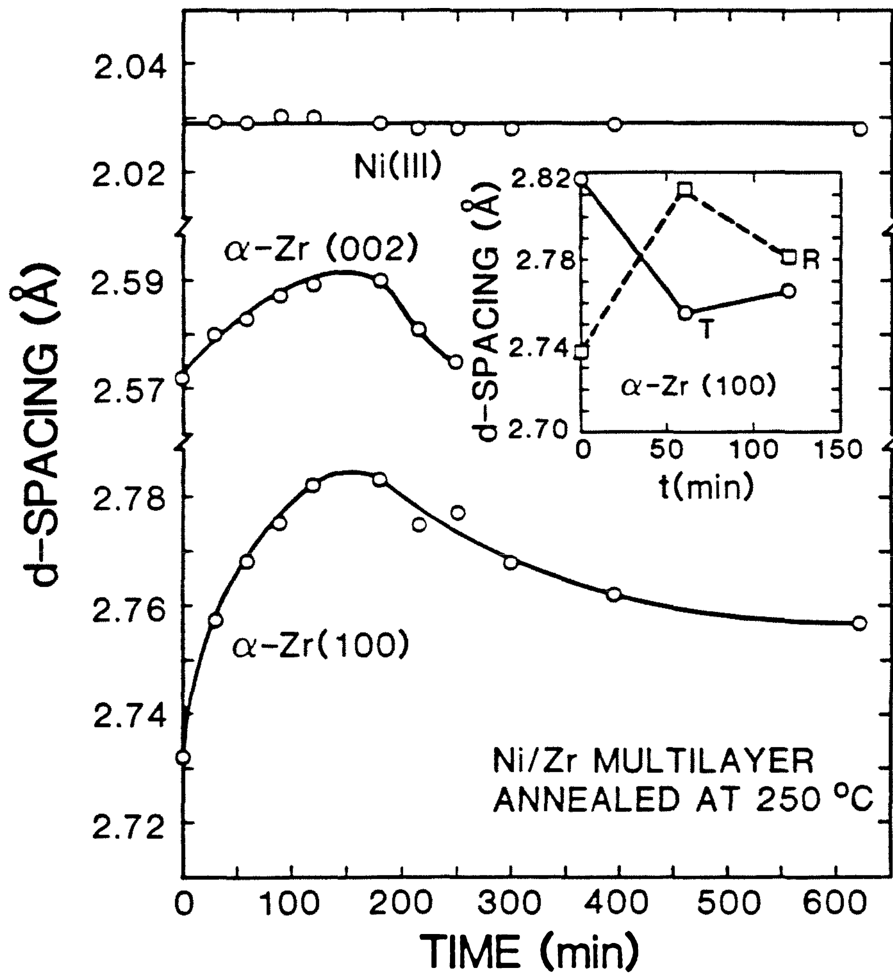

Fig. 3.6 d-spacings of Ni (111), Zr (002), and Zr (100) Bragg peaks as a function of reaction time at 250°C in reflection geometry. The insert shows the Zr (100) d-spacing as a function of reaction time in both reflection (R) and transmission (T) (see text).

seen to result in a compressive stress on the unreacted Zr layers. It should also be noted that even though the amorphous layer also stresses the Ni layers, little relative strain results because of the substantially greater bulk modulus of Ni[18]. It is this building up of in-plane compressive stress that eventually results in the buckling of the film from the substrate. The slower rate of consumption of the elemental Ni and Zr after the film buckles away from the substrate, as shown in Fig. 4, may be a result of the relief of this in-plane stress.

The changing resistivity during growth of the amorphous NiZr interlayer can also be used to monitor the growth kinetics. It can shown that, under the assumption that secondary effects such as recrystallization are negligible, the reduced conductivity of a Ni/Zr bilayer or multilayer diffusion couple, the average composition of which equals that of the growing amorphous interlayer, is related directly to the growth of the amorphous interlayer by

$$\frac{\sigma(t) - \sigma(0)}{-\sigma(0)} = \frac{l_{am}(t)}{l_{Ni}(0) + l_{Zr}(0)}, \tag{10}$$

where $\sigma(t)$ and $\sigma(0)$ denote the conductivity at time t and the intitial conductivity, $l_{Ni}(0)$, $l_{Zr}(0)$, and $l_{am}(t)$ are the initial Ni and Zr individual layer thickness and the amorphous interlayer thickness, respectively. A term on the order of the ratio of conductivities for the amorphous phase and the elements has been neglected because of the substantially higher resistivity of the amorphous phase. Resistivity measurements were carried out with a standard four-point probe method[19] in real time as the amorphization reaction is in progress. A typical resistance-versus-time curve taken during reaction of a Ni/Zr multilayer at a furnace temperature of 225°C is shown in Fig. 7. The reduced conductivity exhibits linear dependence on the square root of time at long times, in agreement with a diffusion-controlled

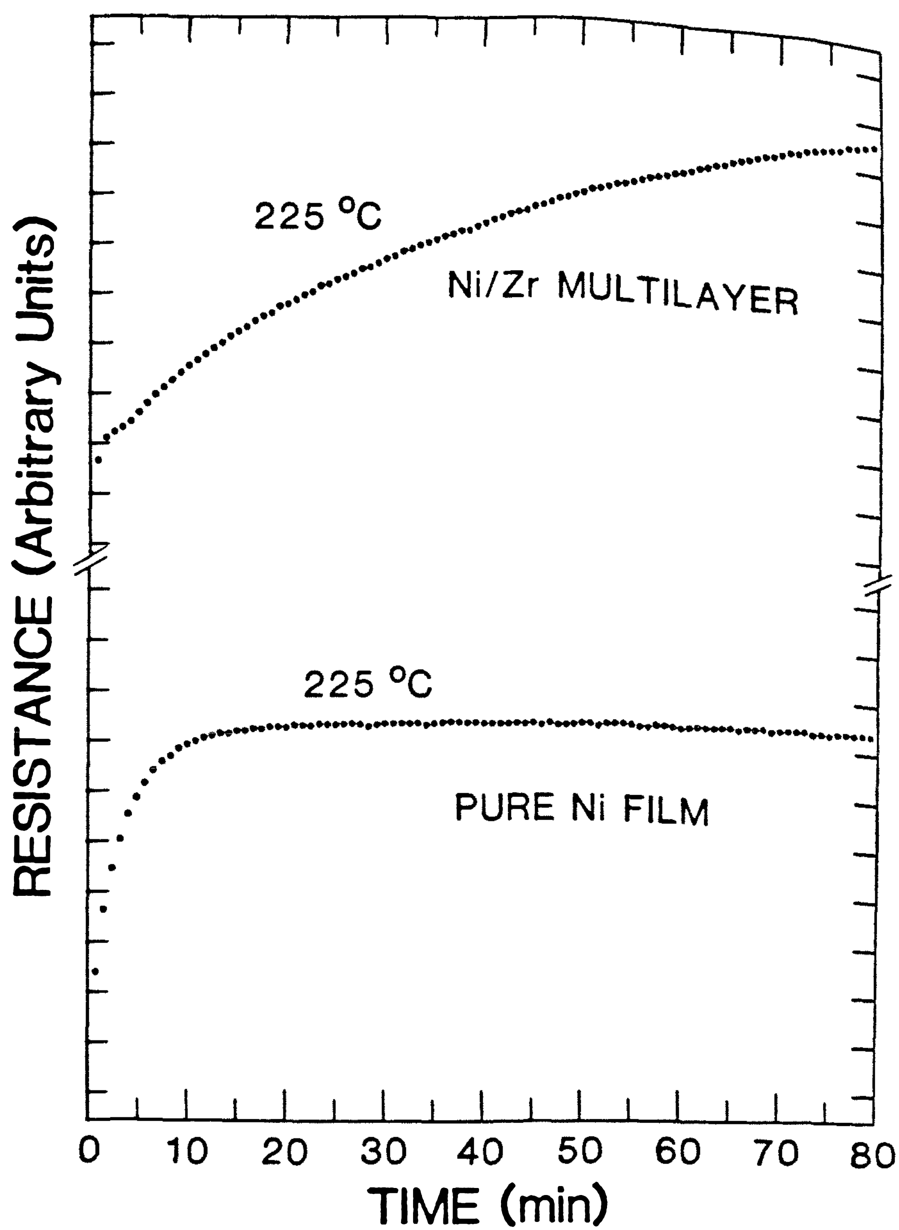

Fig. 3.7 Resistance of a Ni/Zr multilayer (top) vs. reaction time at 225°C. Shown also is the resistance of a pure Ni film (bottom) vs. time under identical experimental settings (see text).

growth of the amorphous interlayer[20]. Shown also in Fig. 7 is the measured resistance versus time for a pure Ni film prepared in the same way as the Ni/Zr multilayer on the same type of substrate. The initial increase in the resistance of the pure Ni film is due to the sample temperature equilibration, the time constant of which is about 10 minutes. The measured resistance curve of the Ni/Zr multilayer displays a kink as a result of the changing temperature in the early stage of the reaction. Thus, any attempt to extract the early stage growth kinetics of the amorphous interlayer is rendered unreliable by the effect of changing temperature during measurement[20]. Our result does, however, indicate that the diffusion-controlled growth of the amorphous interlayer sets in rather early.

3.4 Differential Scanning Calorimetry

Phase transformations such as the melting of a solid to a liquid or transition from one solid phase to another are first order, and such transformations are accompanied by the absorption or release of heat. The effects of this heat absorption or release are experimentally detected by various calorimetric techniques, which are used in turn to elucidate the original process of phase transformation in the sample. Two major high-temperature calorimetric techniques are differential thermal analysis (DTA) and differential scanning calorimetry (DSC). Although some contemporary DSC instruments are capable of performing calorimetric work down to liquid nitrogen temperature, commercially available thermal analysis instruments are used most often in the temperature range from room temperature up to 1500°C. Fig. 8(a) and 8(b) show schematic illustrations of a DTA system. A furnace block contains two symmetrically located and identical chambers, each

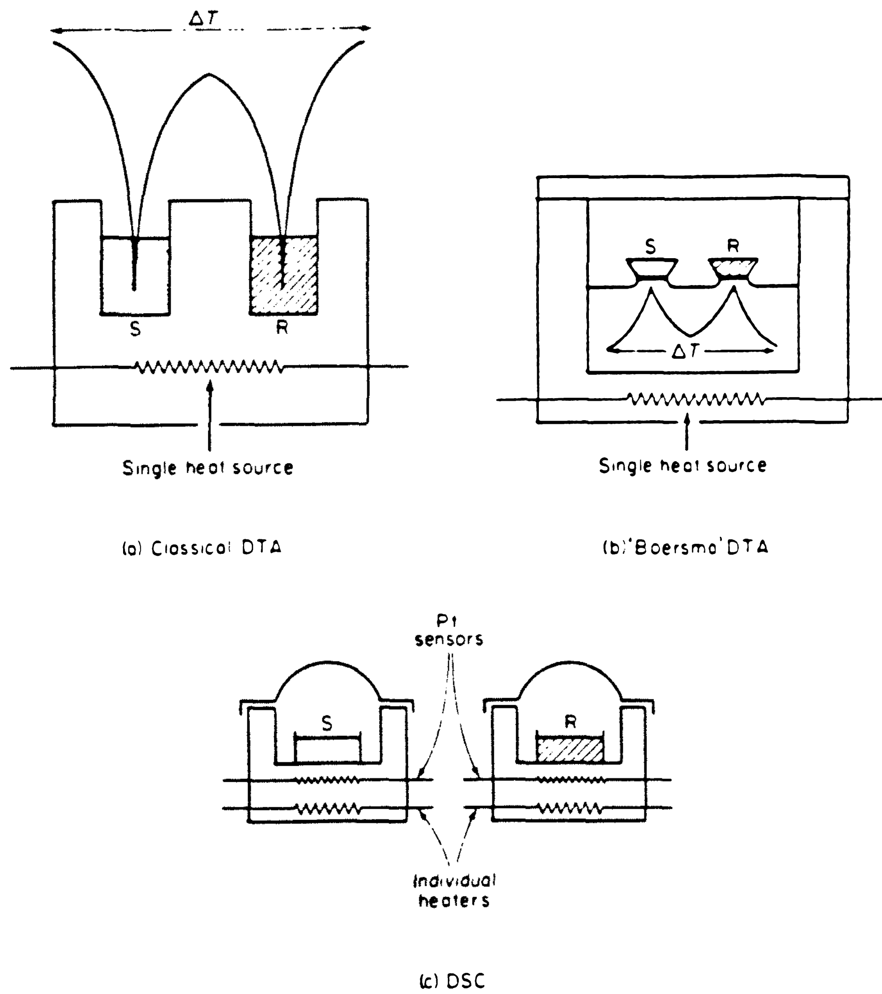

Fig. 3.8 Schematic illustrations of various thermal analysis systems. Taken from Ref. 21.

containing an identical temperature detection device. The sample to be investigated is placed in one chamber, and a thermally inert reference material (such as Al_2O_3) with similar heat capacity as the sample is placed in the other chamber. Both chambers are then heated in an identical manner by the furnace at a constant heating rate, and the *temperature difference* between the sample and reference material is detected by the temperature detection devices located in each chamber and recorded as a function of furnace temperature. Endothermic or exothermic reactions occurring in the sample are manifested as a negative or positive temperature difference although quantitative evaluation of the total heat evolution is difficult, since instrumental factors have to be taken into account[21].

Fig. 8(c) shows a schematic of a DSC system. A sample and reference material are placed in two separate furnaces each equipped with its own temperature detection-device and heater. An average electronic control loop controls both the temperature of the sample and the reference material to follow a predetermined thermal history, and an additional control loop adjusts the power inputs to remove any detected temperature difference between the sample and the reference material. The sample temperature is thus always kept the same as the reference temperature and a signal proportional to the *power difference* between power input into the sample and reference material is recorded as a function of temperature. The recorded signal at any instant is proportional to the instantaneous rate of heat absorbed or released by the sample in the limit of small thermal resistance between the sample and the furnace[21]. Thus, the DSC technique is well suited for the study of kinetics of phase transformations, since it is capable of subjecting samples to be investigated to a precisely controlled thermal history as well as of monitoring the rate of reac-

tion by directly measuring the rate of heat evolution from the sample. Calibration of temperature (abscissa) and energy (ordinate) on a DSC instrument is usually accomplished by observing melting of high-purity metals[22]. Fig. 9 shows the melting endotherm of pure lead. A flat lead sheet (99.99%+) was encapsulated in between two Al pans that are hermetically sealed together. The melting endotherm rises linearly on the leading edge because of the finite thermal resistance between the sample pan and furnace[21]. Melting points of several pure metals (e.g., In, Sn, Pb) can be determined and the instrument adjusted so that the measured melting points do not differ from tabulated values by more than $\pm 2°C$ in the temperature range $50 - 600°C$. Since the apparent transition temperature is slightly dependent on the heating rate, as shown in Fig. 10, the final adjustments are made at the heat rate used for real measurements. The energy calibration constant can also be obtained from such melting endotherms, since the total heat release associated with the melting endotherm should be the heat of fusion which for pure metals is known very accurately. After determination of the calibration constant, the ordinate is read directly in units of millicalories per second.

We have utilized differential scanning calorimetry to monitor the solid-state amorphization reaction in multilayered thin-film diffusion couples of elemental Ni and Zr. DSC measurements were carried out on a Perkin-Elmer DSC-4 interfaced to an Apple IIE computer for data collection. Ni/Zr multilayered thin films were fabricated consisting of alternating layers of elemental Ni and Zr with every Ni (Zr) layer being the same thickness. The total number of Ni and Zr layers is equal. A schematic of the geometry of such multilayered diffusion couples is shown in Fig. 11. The average atomic composition of the multilayer $Ni_{x_{Ni}}Zr_{x_{Zr}}$ is determined by

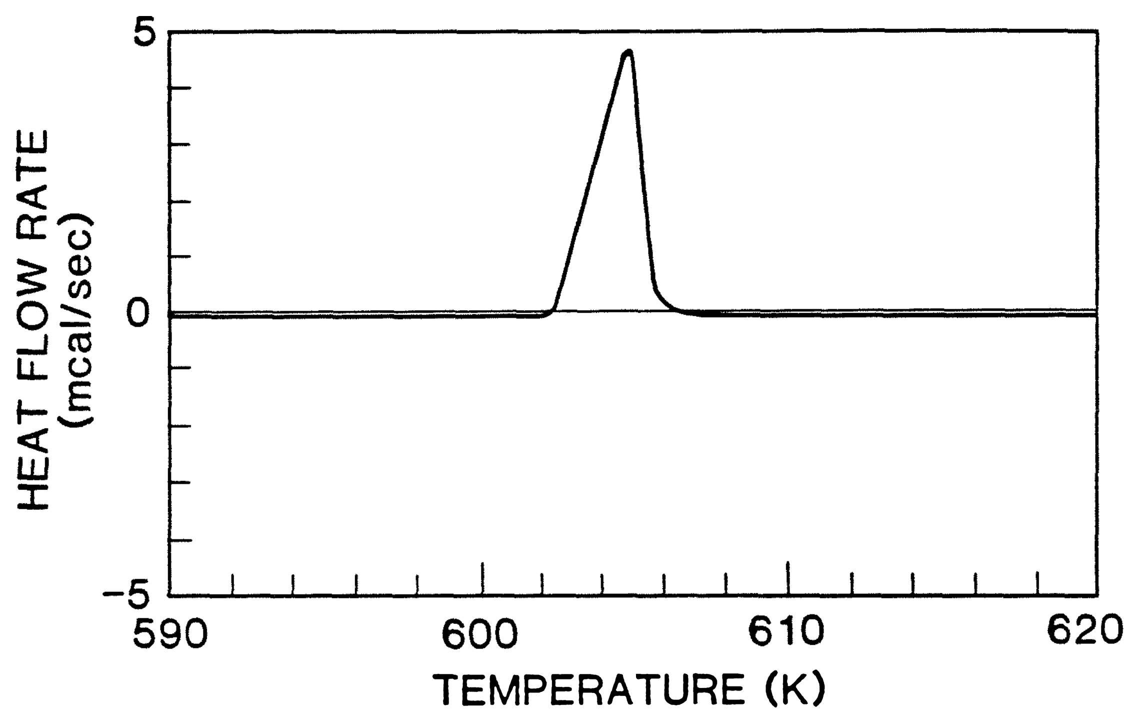

Fig. 3.9 Melting endotherm of pure Pb (4N+) at 10 K/min taken on a Perkin-Elmer DSC-4.

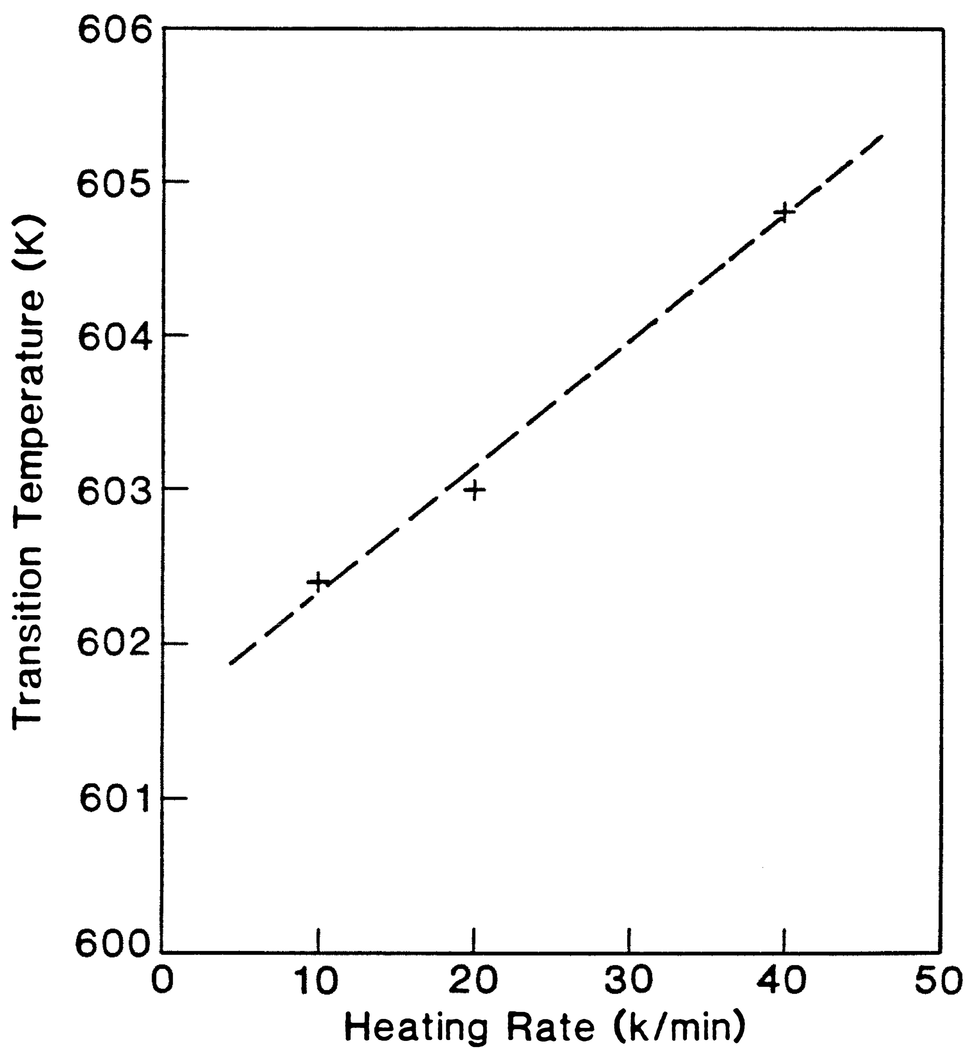

Fig. 3.10 Apparent melting temperature of pure Pb (4N+) vs. DSC heating rate.

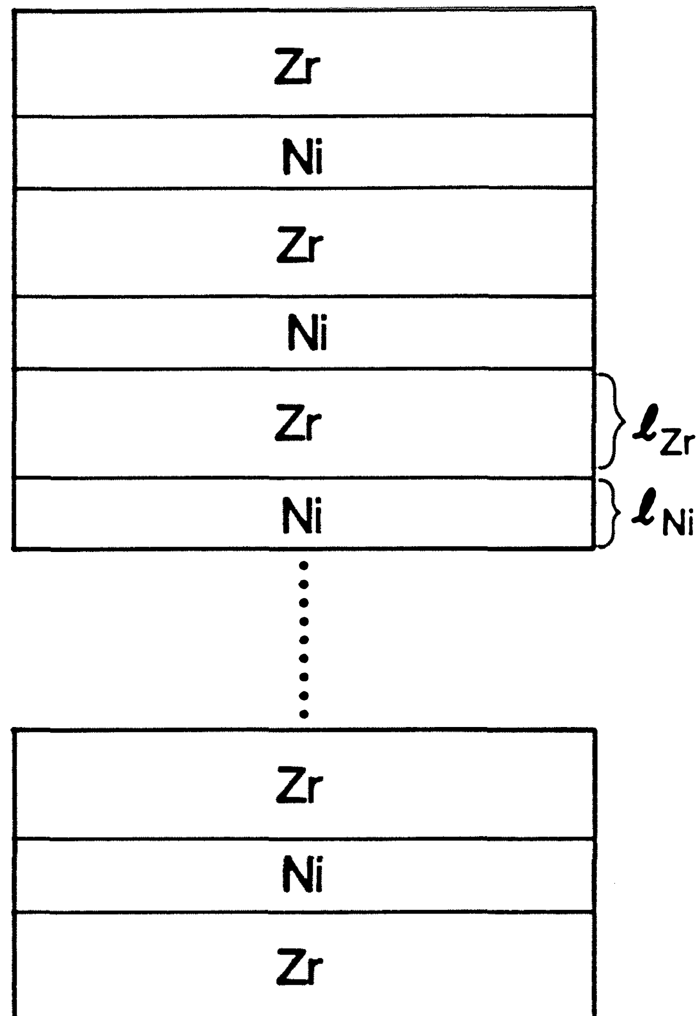

Fig. 3.11 Geometry of Ni/Zr multilayered diffusion couples.

the ratio of the individual Ni and Zr layer thicknesses l_{Ni} and l_{Zr}. For the geometry shown in Fig. 11, we have

$$x_{Zr}/x_{Ni} = (\frac{l_{Zr}\rho_{Zr}}{M_{Zr}})/(\frac{l_{Ni}\rho_{Ni}}{M_{Ni}}) \tag{10.1}$$

$$x_{Zr} + x_{Ni} = 1, \tag{10.2}$$

where ρ and M refer to the densities and molar masses of the pure Zr and Ni, respectively. Equation (10) can be simplified to

$$x_{Ni} = \frac{1}{1 + 0.47(l_{Zr}/l_{Ni})}. \tag{11}$$

The very top and bottom two layers of such Ni/Zr multilayers are always made of Zr. The thickness of the top and bottom Zr layers should be one-half of a full Zr layer to insure the symmetry of the whole diffusion couple. In practice, the extra half-thickness layers of Zr on both the top and the bottom of the samples serve as protective caps against oxidation[23]. Multilayered thin films were deposited onto cleaved NaCl substrates. After deposition, samples were immersed in distilled water, and the Ni/Zr films floated off the substrate. They were captured and rinsed in ethanol. These freestanding films were dried and immediately hermetically sealed in aluminum pans by cold welding in an inert gas atmosphere (Ar or He) with a minimal volume of gas sealed in each sample pan. The sample configuration, a flat metal sample in intimate contact with a flat metal pan, is optimal for DSC measurements. Actual measurements were carried out at a constant heating rate of 10K/min in the temperature range 320 to 870K with sealed Au pans as reference. Sample scans were followed immediately by a second scan of identical thermal history. If we assume that all phase transformations were completed at the end of the first scan, then the DSC signal from these two consecutive scans can be summarized

as follows:

$$signal(1) = \frac{dH}{dt} + (C_p^s(1) - C_p^r)R + d \quad (12.1)$$

$$signal(2) = (C_p^s(2) - C_p^r)R + d, \quad (12.2)$$

where dH/dt denotes the rate of heat release due to the phase transformation undergone by the sample, C_p^r denotes the heat capacity of the reference material and $C_p^s(1)$ and $C_p^s(2)$ denotes the heat capacity of the sample before and after the phase transformation. R is the heating rate and d denotes any instrumental drifts. Thus, the difference spectrum between these two spectra

$$signal(1-2) = \frac{dH}{dt} + \Delta C_p^s R \quad (13)$$

eliminates instrumental drift and better elucidates phase transformations undergone by the sample. All subsequent DSC data shown are, in fact, such difference spectra where no attempt was made to compensate for changes in the heat capacity of the sample upon transformation. After a DSC run, the cold-welded flanges of the sample pan were cut off and the samples were removed for x-ray diffraction study. A Norelco x-ray diffractometer with Ni- filtered Cu $K\alpha$ radiation was used for obtaining x-ray diffraction patterns of the materials.

The rate of heat release upon amorphization of a Ni/Zr multilayer, as well as upon crystallization, is displayed in Fig. 12. This DSC scan was conducted at 10K/min with a 5.06 milligram sample consisting of 45 Ni and 45 Zr layers each; all layers were 300Å in thickness. The scan reveals two separate reactions: the first reaction (centered at temperature $T = 580$K), which we identify with the amorphization of the original crystalline multilayers and the second reaction (centered at temperature $T = 830$K), which we identify with the subsequent

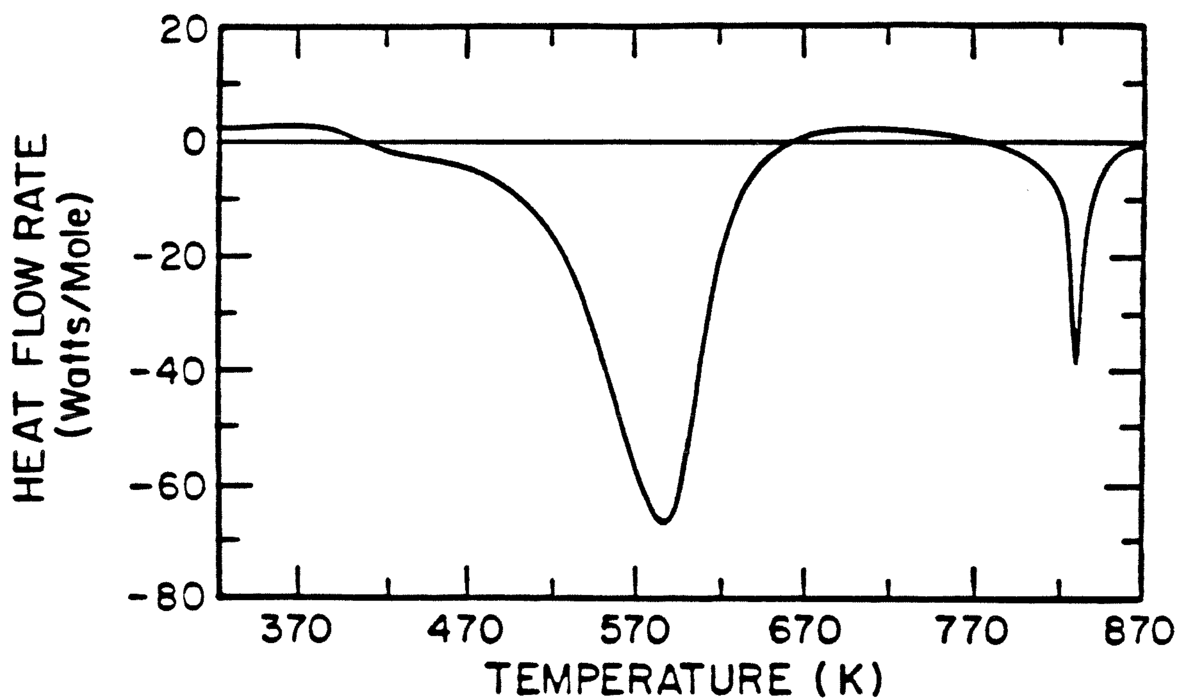

Fig. 3.12 Measured heat flow rate as a function of temperature for a sputtered Ni/Zr multilayer, $l_{Ni} = l_{Zr} = 300$Å, average stoichiometry $Ni_{68}Zr_{32}$.

crystallization of the amorphous phase. An x-ray diffraction pattern of the as- deposited sample (a control sample from the same deposition) is shown in Fig. 13(a). Fig. 13(b) shows the diffraction pattern for a sample heated up to 670K and then cooled quickly to room temperature. Finally, Fig. 13(c) shows the diffraction pattern for a sample heated up to 870K and then cooled quickly to room temperature. Diffraction of the as-deposited sample reveals Bragg peaks corresponding to elemental Ni and Zr. After the sample has been heated to 670K at 10K/min, the elemental peaks have vanished and a broad diffuse maximum characteristic of an amorphous phase centered at $2\theta = 41.4°$ has appeared, with a secondary maximum visible at a higher angle. The residual (002) reflection of Zr corresponds to the thicker external Zr layers on the sample, which we do not expect to react fully[23]. By examining the correlation between the position of the first diffraction maxima of various liquid-quenched amorphous NiZr alloys and their compositions[24], we interpolate the average composition of the amorphous NiZr alloy formed during this *in situ* reaction to be 68 ± 2 atomic percent Ni. This agrees with the nominal average composition of the as-deposited multilayer, which is $Ni_{68}Zr_{32}$. The nearly constant heat-flow rate observed at temperatures in the range up to 350K and the range near 720K is interpreted as corresponding to the rate of reaction being zero. The growth rate of the amorphous interlayers first becomes observable at $T \sim 370$K and finally falls to zero at $T \sim 720$K. At the latter temperature, the amorphization process is apparently completed. The total heat release of the crystalline- to- amorphous transformation seen in Fig. 12 can be calculated via integration between these two temperatures. We find for this sample a heat release upon amorphization of 510 J/g, or 35 kJ/mole. The peak observed at 830K, corresponding to crystallization of the already formed amorphous material, falls between the previously measured crystallization temperatures (with the same heating

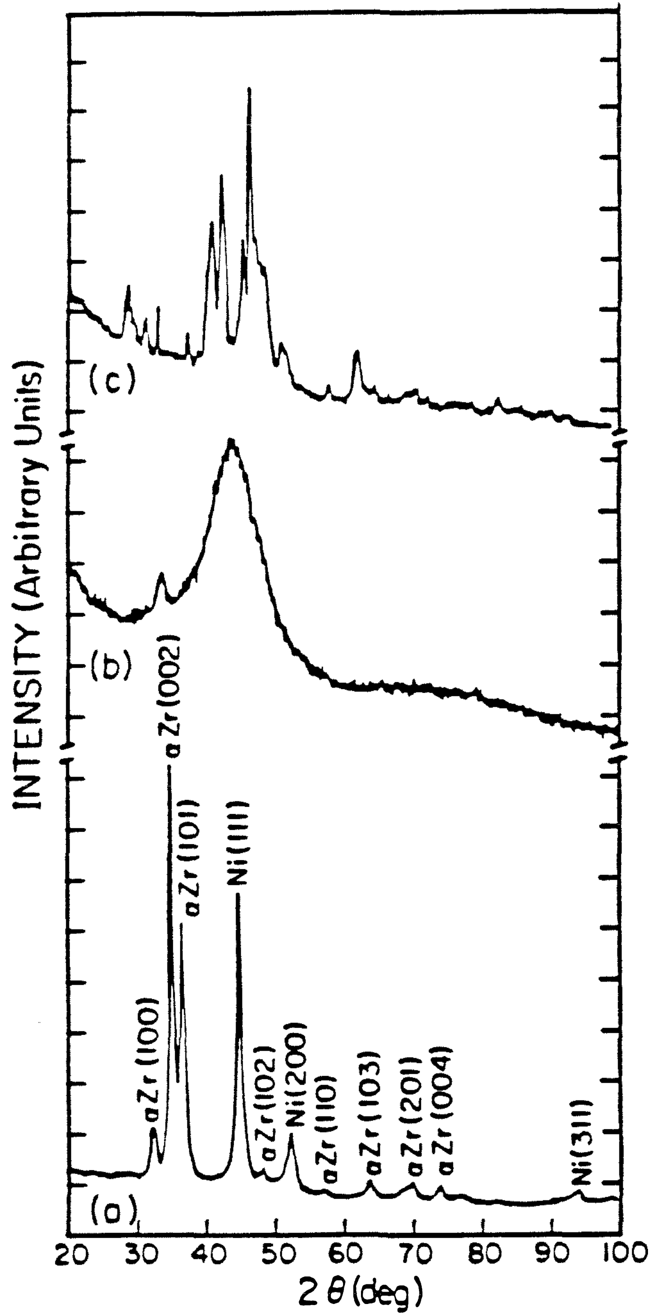

Fig. 3.13 X-ray diffraction patterns for the thin film sample of Fig. 3.12, see text.

rate of 10K/min) of liquid quenched amorphous $Ni_{67}Zr_{33}$ and $Ni_{68.8}Zr_{31.2}$[25]. The integrated enthalpy release for this crystallization peak is 4.2 ± 0.2 kJ/mole, which compares well with an enthalpy release of 3.9 kJ/mole previously observed for liquid-quenched $Ni_{67}Zr_{33}$[25]. This is viewed as further evidence that upon heating of the Ni/Zr multilayer to 670K at 10K/min, a completed solid-state amorphization reaction to a relatively homogeneous amorphous state has occurred. We have further examined these solid-state amorphization reactions in Ni/Zr multilayered samples of varying individual layer thicknesses. In Fig. 14, one observes that the basic shape of the DSC scans is repeated for multilayers with individual layer thicknesses of 300, 450, and 1000Å , respectively. For the samples with increasing individual layer thickness, the maximum rate of heat release is observed to occur at higher temperatures. Nevertheless, the total amount of heat release per mole, obtained upon integration of a DSC curve, remains constant, independent of the individual layer thicknesses in a multilayered sample. The enthalpy release of the amorphization transformation displayed in Figs. 12 and 14 should correspond closely to that of the formation enthalpy of the amorphous phase. Evaluation of the reaction product by use of x-ray and DSC analysis indicates an amorphous alloy with a high degree of homogeneity, similar to that obtained in liquid- quenched samples. X-ray analysis of the initial, multilayered sample indicates that it is composed of polycrystalline layers of pure elements, although there may be some initial intermixing at the original Ni/Zr interfaces during film deposition[26]. We note that examination of samples with thicker individual layers showed no marked dependence of the measured enthalpy release on layer thickness, an indication that any prior intermixing does not significantly influence the measured heat of formation within the precision of the measurement. Internal stresses are also known to accompany the formation of amorphous interlayers in these multilayered diffusion

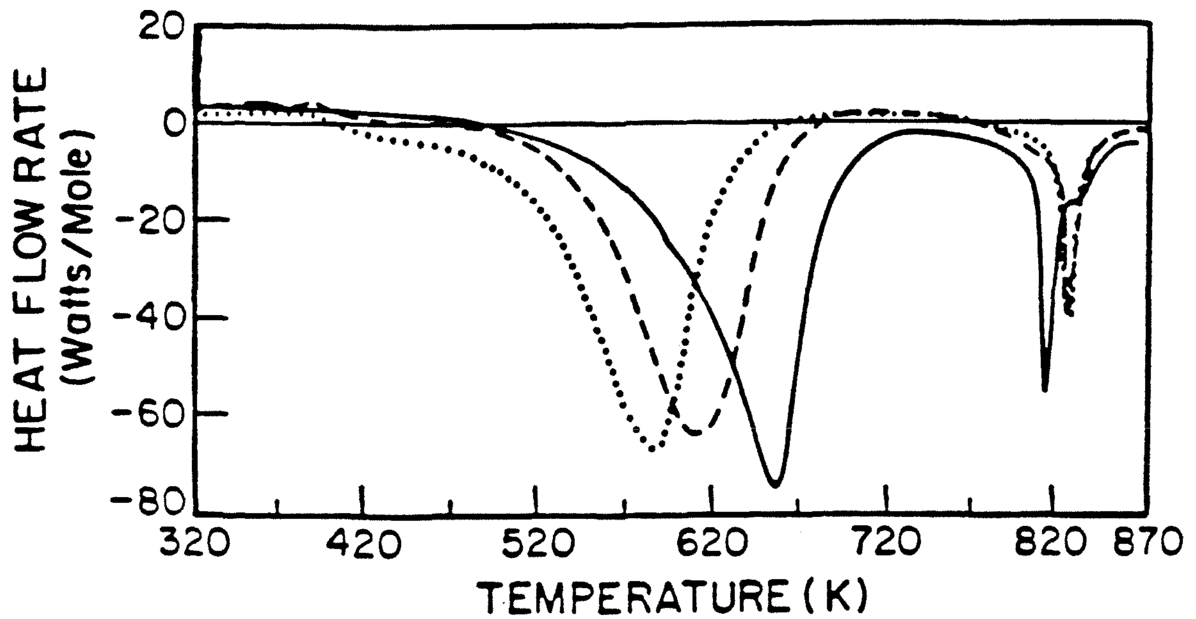

Fig. 3.14 Measured heat flow rate as a function of temperature for Ni/Zr multilayers with varying individual layer thicknesses. Dotted curve, l = 300Å; dashed curve, l = 450Å; solid curve, l = 1000Å.

couples (see Section 3.3), but any resultant strain energy should be 1 to 2 orders of magnitude less than the relevant chemical energy[27]. We therefore conclude that the present measurement yields an accurate determination of the heat of formation of the amorphous phase. Including the experimental precision, we thus arrive at $35\pm$ 5 kJ/mole for the heat of formation of amorphous $Ni_{68}Zr_{32}$ alloy from the elemental metals. Our measurement is slightly lower compared with previous measurements via dissociation calorimetry on liquid-quenched amorphous NiZr alloys of similar concentrations[28]. The heat of mixing for amorphous $Ni_{65}Zr_{35}$ alloy reported by these authors is 45 kJ/mole.

From the data shown above, we see that the heat release from the amorphization reaction and crystallization can be separated. The rate of heat release upon amorphization of a planar multilayered sample is directly related to the amorphous interlayer growth kinetics. Growth of amorphous NiZr interlayers has been observed to be planar. Previous RBS measurements showed that the growing amorphous interlayer possesses a linear concentration profile and constant interfacial concentrations fixed by thermodynamic equilibrium conditions[29]. The average concentration of the growing amorphous interlayer remains constant in time[29]. Therefore, a proportionality exists between the measured heat release rate dH/dt and the rate of amorphous interlayer growth dX/dt, where X is the interlayer thickness. An approximate relationship can be written as

$$\frac{dH}{dt} = A\frac{\rho(\bar{c})}{M(\bar{c})}H(\bar{c})\frac{dX}{dt}, \qquad (14)$$

where A is the total Ni/Zr interfacial area of the original multilayers. $\rho(\bar{c})$, $M(\bar{c})$, and $H(\bar{c})$ are the density, molar mass, and enthalpy of formation of amorphous NiZr alloy at the average concentration $\bar{c}$ of the growing amorphous interlayer. The total

Ni/Zr interfacial area is given by

$$A = \frac{2M}{l_{Ni}\rho_{Ni} + l_{Zr}\rho_{Zr}}, \quad (15)$$

where ρ_{Ni} and ρ_{Zr} are densities of pure Ni and Zr, and M is the mass of the multilayered sample. Therefore, the rate of heat release normalized by the total Ni/Zr interfacial area of the sample is a direct reflection of the growth kinetics involved. The data shown in Fig. 14 between 320K and 720K are redrawn in Fig. 15 after normalizing each curve by the total interfacial area of the corresponding Ni/Zr multilayer. All normalized DSC curves show qualitatively the same form, indicating that the growth law is independent of layer thicknesses. Fig. 16 shows a set of such normalized data taken from samples of different average compositions (i.e., different Ni-to-Zr layer thickness ratios). All data again show similar growth behavior with increasing temperature up to the point where deviations are caused by the exhaustion of the supply of one or both elemental components. This implies that the average composition of the amorphous interlayer formed is the same, independent of the starting elemental layer thicknesses up to the point where the supply of one or both of the elements is consumed. If the growth of the amorphous interlayer is diffusion-limited, according to Section 3.2, an average interdiffusion constant $\tilde{D}_{am}$ of the amorphous alloy can then be directly related to the growth velocity dX/dt by

$$\frac{dX}{dt} = G_{am} \Delta C_{am}^{eq} \frac{\tilde{D}_{am}}{X}, \quad (16)$$

where ΔC_{am}^{eq} is the equilibrium concentration difference across the growing amorphous interlayer, G_{am} is a constant of order unity and X is the thickness of the amorphous interlayer. If the interdiffusion process is assumed to be thermally activated with a single activation energy Q', i.e., $\tilde{D}_{am} = D_o exp(Q'/k_B T)$, then

$$ln(X\frac{dX}{dt}) = ln(G_{am} \Delta C_{am}^{eq} D_o) - \frac{Q'}{k_B T}. \quad (17)$$

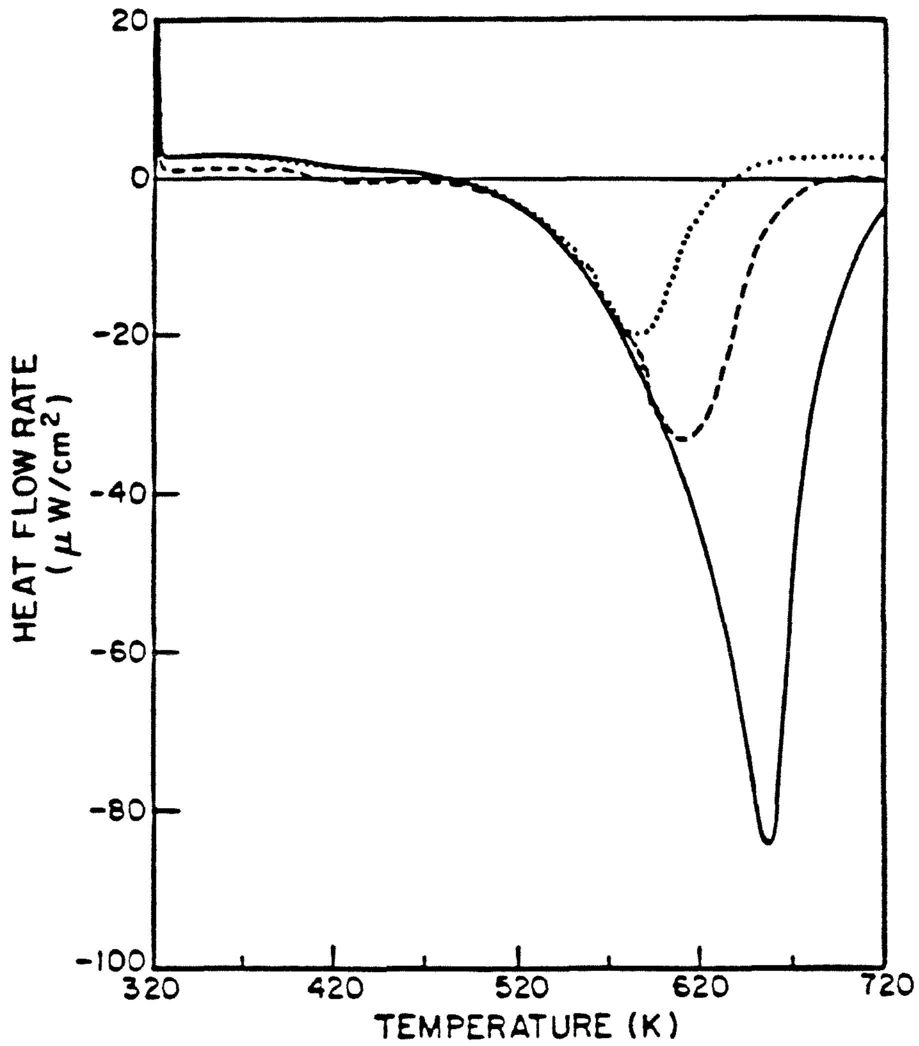

Fig. 3.15 Heat-flow rate as a function of temperature normalized to the total interfacial area of the respective Ni/Zr multilayers in Fig. 3.14.

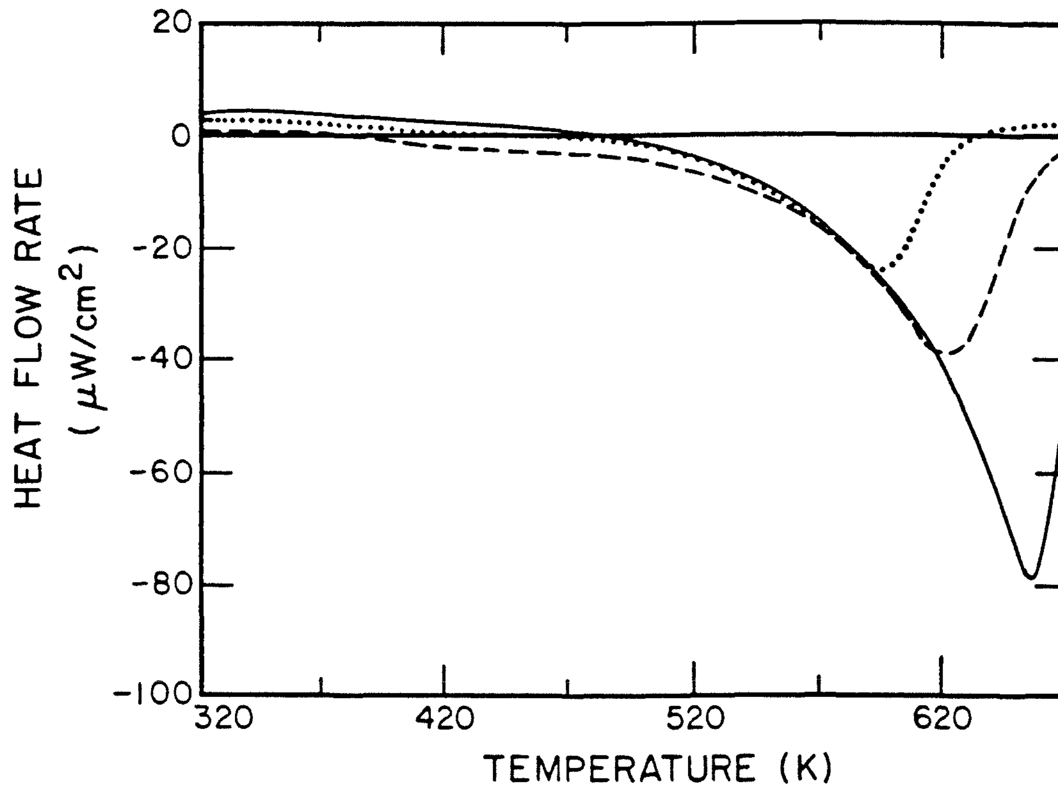

Fig. 3.16 Heat-flow rate normalized by the total Ni/Zr interfacial area of multilayers of various individual layer thicknesses and average compositions. Dotted line, $l_{Ni} = 300Å/l_{Zr} = 450Å$; dashed line, $l_{Ni} = 500Å/l_{Zr} = 800Å$; solid line, $l_{Ni} = l_{Zr} = 1000Å$.

Analysis of typical DSC scan accordingly is plotted in Fig. 17 with $H(\bar{c})$ assumed to be 40kJ/mole in the analysis. A linear fit to the data shown in Fig. 17 yields both the activation energy Q' and the pre-exponential factor D_o for interdiffusion through the amorphous NiZr interlayer. The activation energy Q' is determined to be 1.05eV, and $D_o = 4 \times 10^{-9} m^2/sec$ if ΔC^{eq}_{am} is taken to be 0.21[29], and G_{am} to be 1.0[9]. Both the activation energy and pre-exponential factor for interdiffusion through the amorphous NiZr interlayer so determined agree well with previous measurements[30], demonstrating that the interdiffusion process through the amorphous NiZr interlayer is indeed diffusion- controlled. The advantage of such DSC measurement on the growth kinetics lies in the capability of precisely controlled thermal history and continuous measurement over a large temperature interval ($\sim$ 100K); such features can not be easily reproduced by other commonly used techniques such as Rutherford backscatterng measurements. Linearity of such plots persists to rather early stages of the amorphization reaction, in agreement with the previous suggestion that the amorphous interlayer growth switches from interface to diffusion-controlled fairly early on in the reaction.

A DSC measurement yields information not only on the amorphization of the original crystalline Ni/Zr multilayers, but also on the subsequent homogenization and crystallization of the amorphous phase. Depending on the average concentration of the multilayer, the formation of the amorphous phase exhausts either the supply of one element first or both elements at the same time. Any subsequent compositional homogenization processes compete with the crystallization of the amorphous reaction product. Since the crystallization temperature of amorphous NiZr alloys has been reported to have a strong dependence on composi-

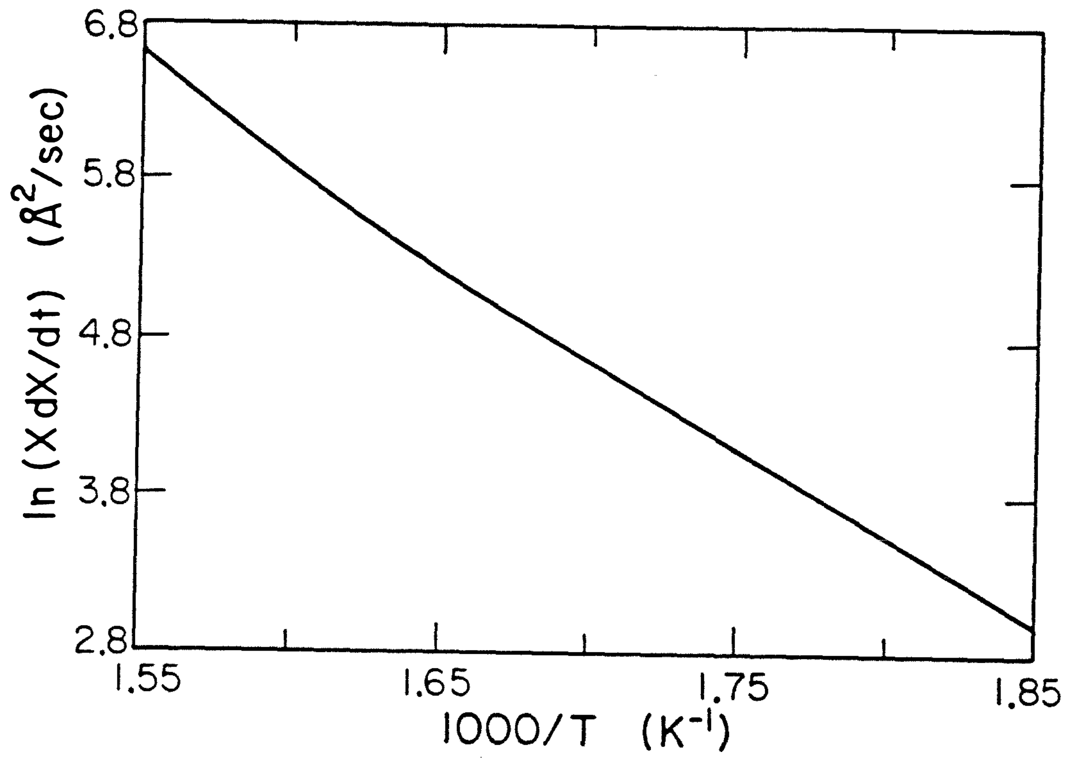

Fig. 3.17 Arrhenius plot for the determination of the activation energy and pre-exponential factor of the interdiffusion constant (see text).

tion[25], the subsequent crystallization of the amorphous phase should consequently be a sensitive function of its degree of compositional homogeneity. Shown in Fig. 18 are the DSC data obtained by reacting two Ni/Zr multilayers, both with individual Zr layer thicknesses of 450Å. However, the individual Ni layer thickness of one sample is 300Å with its corresponding DSC scan shown in Fig. 18(a). The average concentration of this sample is $Ni_{59}Zr_{41}$. The individual Ni layer thickness of the other sample is 450Å with its corresponding DSC scan shown in Fig. 18(b). The average concentration of this sample is $Ni_{68}Zr_{32}$. Amorphization of these two samples proceeds similarly, as is evident from Fig. 18, although there are significant differences between their crystallization behaviors. In the reaction of a sample of average stoichiometry $Ni_{68}Zr_{32}$ as shown in Fig. 18(b), the amorphization process is essentially complete by $T \sim 700K$. Crystallization of the amorphous phase manifests itself in a single exothermic peak at $T \sim 830K$. Both the temperature and enthalpy of crystallization agree with previous DSC measurements on liquid- quenched amorphous $Ni_{67}Zr_{33}$ alloy[25]. This suggests that the amorphous reaction product is relatively homogeneous when crystallization occurred. On the contrary, in the reaction of an average $Ni_{59}Zr_{41}$ sample as shown in Fig. 18(a), the process of crystallization starts at $T \sim 700K$, and heat is continuously released until $T \sim 830K$. A homogeneous liquid- quenched amorphous $Ni_{60}Zr_{40}$ alloy is observed to crystallize at 750K in a single step[25]. Therefore, the data indicate that crystallization in this case occurred when the amorphous reaction product is still compositionally inhomogeneous. Fig. 19 shows a set of DSC data from samples with average compositions near $Ni_{58}Zr_{42}$ but with different individual layer thicknesses. This average composition corresponds to the case where both elemental Ni and Zr layers will be consumed by the amorphous phase simultaneously[29]. The DSC scans in Fig. 19(a), 19(b), and 19(c) were obtained from samples with

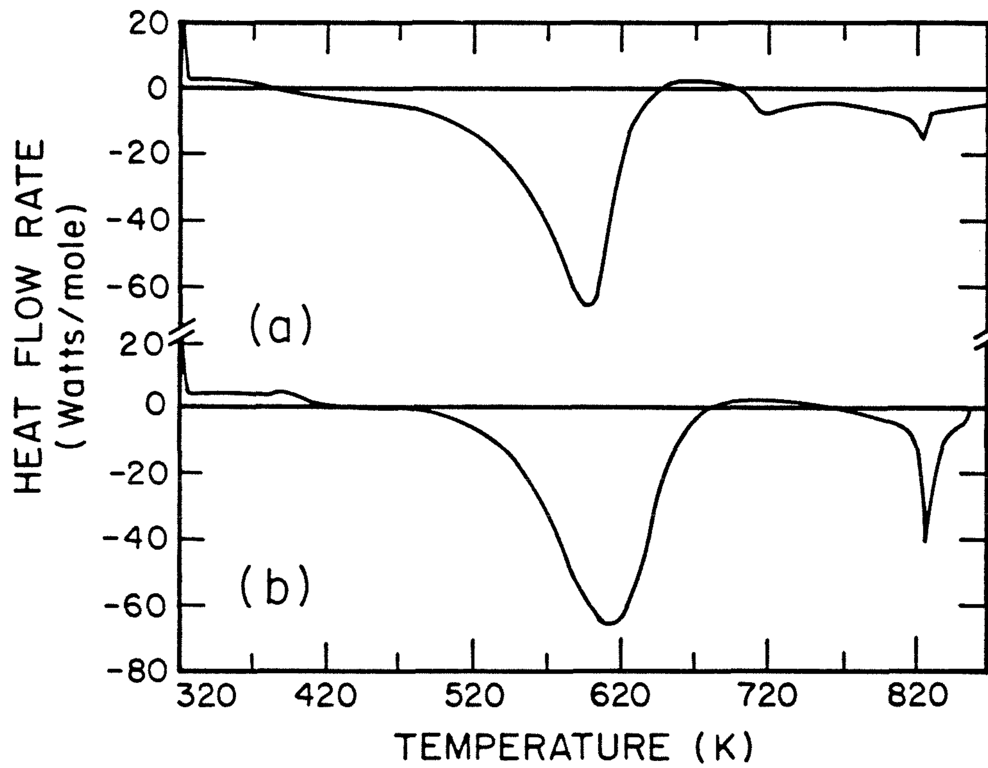

Fig. 3.18 Heat-flow rate vs. temperature for sputtered Ni/Zr multilayers of two different average compositions: (a) $Ni_{59}Zr_{41}$, (b) $Ni_{68}Zr_{32}$ (see text).

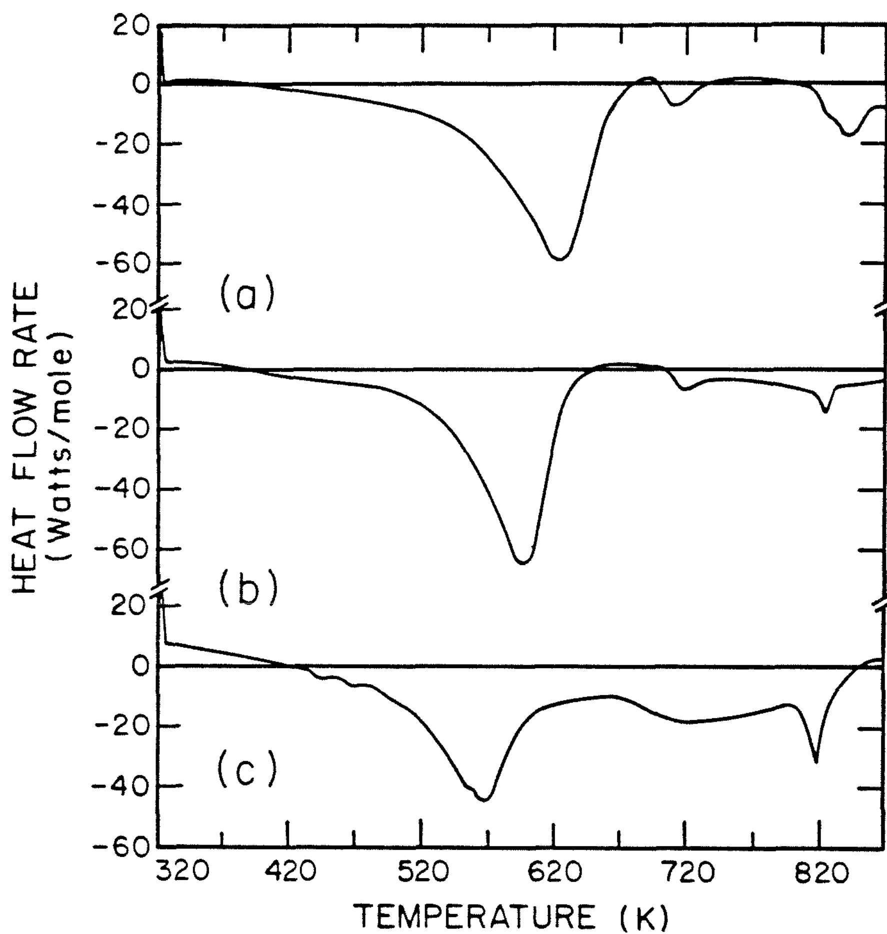

Fig. 3.19 Heat-flow rate vs. temperature of Ni/Zr multilayers with various Zr layer thicknesses: (a) $l_{Zr} = 800\AA$, (b) $l_{Zr} = 450\AA$, (c) $l_{Zr} = 240\AA$. Average composition $\sim Ni_{58}Zr_{42}$ for all three samples.

individual Zr layer thicknesses of 800, 450, and 240Å , respectively. Similar crystallization behavior is observed in all data shown in Fig. 19, indicating in all cases that crystallization occurred before the composition homogenization of the amorphous interlayer is complete. Data shown in Fig. 19 suggest that composition homogenization within the amorphous interlayer is a very slow process. This serves as a warning against too loosely regarding measured total heat release during amorphization as the heat of mixing for the amorphous phase, since it is clear from the above discussion that obtaining a homogeneous amorphous phase can be difficult at certain compositions. Integration of the DSC scan shown in Fig. 19(c) from 330K to 670K yields a total heat release of 38kJ/mole. Since the reaction product at 670K is still inhomogeneous, this value can be regarded only as a lower bound for the enthalpy of mixing of an amorphous $Ni_{59}Zr_{41}$ alloy.

3.5 Summary

It has been shown in this chapter that the process of formation of amorphous alloys in thin film diffusion couples, both the growth kinetics and thermodynamics, can be studied in some detail by a combination of x-ray, resistivity, and thermal measurement techniques. The growth of an amorphous NiZr interlayer has been determined to be diffusion-controlled. The lowering of free energy upon amorphization is demonstrated to be chemical in nature, arising mainly from a large negative heat of the mixing of the elements to form the amorphous phase.

3.6 References

1. P. Haasen, *Physical Metallurgy*, Ch. 5 (Cambridge University Press, London, 1978).
2. W. L. Johnson, Prog. Mater. Sci. **30**, 81 (1986).
3. *CRC Handbook of Chemistry and Physics*, edited by R. C. Weast, section D-43 (CRC press, Florida, 1986).
4. L. Kaufman and H. Bernstein, *Computer Calculation of Phase Diagrams* (Academic Press, 1970).
5. D. Turnbull, J. Chem. Phys. **20**, 411 (1952); J. D. Hoffman, J. Chem. Phys. **29**, 1192 (1958); C. V. Thompson, F. Spaepen, Acta Met. **27**, 1855 (1979); H. B. Singh, A. Holz, Solid State Comm. **45**, 985 (1983).
6. *Thin Films-Interdiffusion and Reactions*, edited by J. M. Poate, K. N. Tu, and J. W. Mayer (Wiley-Interscience, New York, 1978).
7. G. V. Kidson, J. Nucl. Mater. **3**, 21 (1961).
8. B. E. Deal, A. S. Grove, J. Appl. Phys. **36**, 3770 (1965).
9. U. Gosele, K. N. Tu, J. Appl. Phys. **53**, 3252 (1982).
10. B. P. Dolgin, Ph.D. thesis (California Institute of Technology, Pasadena, California, 1985).
11. J. Crank, *The Mathematics of Diffusion* (Oxford University Press, London, 1975).
12. F. M. d'Heurle, P. Gas, J. Mater. Res. **1**, 205 (1986).
13. H. P. Klug and L. E. Alexander, *X-ray Diffraction Procedures* (Wiley, New York, 1974).
14. A. P. Thakoor, S. K. Khanna, R. M. Williams, R. F. Landel, J. Vac.

Sci. Tech. **A1**, 520 (1983).

15. K. L. Chopra, *Thin Film Phenomena*, Ch. 4 (McGraw-Hill, New York, 1969).
16. A. Guinier, *X-ray Diffraction* (W. H. Freeman and Company, San Francisco, 1963).
17. G. M. Hood, R. J. Schultz, Phil. Mag. **26**, 329 (1972).
18. C. Kittel, *Solid State Physics* (Wiley, New York, 1976).
19. L. B. Valdes, Proc. I. R. E. **42**, 420 (1954).
20. W. J. Meng, K. M. Unruh, W. L. Johnson, unpublished.
21. A. P. Gray, in Proc. Amer. Chem. Soc. Symp. Analytical Calorimetry, edited by R. S. Porter and J. F. Johnson (Plenum Press, New York, 1968) p.209.
22. E. S. Watson, M. J. O'Neill, J. Justin, N. Brenner, Anal. Chem. **36**, 1233 (1964).
23. M. Van Rossum, M. A. Nicolet, W. L. Johnson, Phys. Rev. B **29**, 5498 (1984).
24. K. H. J. Buschow, N. M. Beekmans, Phys. Rev. B **19**, 3843 (1979).
25. Z. Altounian, Tu Guo-hua, J. O. Strom-Olsen, J. Appl. Phys. **54**, 3111 (1983).
26. B. M. Clemens, Phys. Rev. B **33**, 7615 (1986).
27. M. Atzmon, Ph.D. thesis (California Institute of Technology, Pasadena, California, 1986).
28. M. P. Henaff, C. Colinet, A. Pasturel, K. H. J. Buschow, J. Appl. Phys. **56**, 307 (1984).
29. J. C. Barbour, Phys. Rev. Lett. **55**, 2872 (1985).
30. H. Hahn, R. S. Averback, S. J. Rothman, Phys. Rev. B **33**, 8825

(1986).

Chapter 4

Evolution of Planar Binary Diffusion Couples

We have shown in Chapter 3 that the growth of an amorphous phase as well as the stability of the amorphous interlayer formed can be studied in some detail by a combination of structural and thermal measurements. In this chapter, we use primarily the technique of transmission electron microscopy (TEM) to further examine the process of amorphous phase formation in planar binary diffusion couples. Again, we have concentrated our efforts on the Ni-Zr system. Emphasis of this study will be placed on ellucidating key factors that limit the initial formation of the amorphous NiZr as well as those that limit the extent of amorphous NiZr formation. Specifically, we will show that a critical thickness of amorphous NiZr interlayer exists beyond which growth of the amorphous phase is replaced by formation of a Ni-Zr intermetallic compound. It will also be shown that formation of the amorphous NiZr is critically dependent on the nature of the initial Ni/Zr interface present. Our results suggest that nucleation plays an important role in controlling the phase formation sequence in Ni/Zr diffusion couples.

4.1 Specimen Preparation

In addition to sputter-deposited Ni/Zr multilayers where both elemental Ni and Zr layers are polycrystalline with typical grain sizes of a few hundred angstroms, we have also fabricated bilayer diffusion couples of Ni and Zr where one

element (Ni or Zr) consists of a mosaic of large single crystals with typical grain sizes on the order of 5-20 μm. Since we are dealing with metal-metal diffusion couples, these large, single crystal mosaics are obtained by recrystallizing commercially available metal foils (Zr foil 25μm, t3N8; Ni foil 100μm, t3N+) in vacuum at high temperatures.

A special heating stage was constructed for this purpose. Two copper pipes were welded to a Conflat vacuum flange through a ceramic-to-metal feedthrough (Ceramaseal Inc.), which isolates the flange from the copper pipes electrically. The two copper pipes are joined by another ceramic-to-metal sealed tube (Ceramaseal Inc.), which electrically isolates them from each other. A metal foil with two ends clamped on a hollow copper block connected with each copper pipe forms the only electrical link between the two. By passing current through the terminals outside the vacuum and also water through the copper pipe, the metal foil can be heated to above 1000°C, while the rest of the assembly stays close to room temperature by water cooling. The temperature of the metal foil (at high temperatures, $> 700°$C) can be measured by an optical pyrometer. A pure metal foil (Zr or Ni) is first rolled between two stainless steel sheaths to a thickness of around 5 μm; this rolled foil is cleaned in acetone and ethanol and immediately loaded into the vacuum system. Surface cleaning as well as recrystallization is accomplished by current heating the foil to around 800°C for a period of 2 - 12 hours. Such modest mechanical deformation of the initial foil along with subsequent high temperature heat treatment for an extended peroid is ideal for growth of large single crystals[1]. The base pressure in the chamber during recrystallization is kept below 3×10^{-8} Torr with oxygen, nitrogen and hydrogen partial pressures of less

than 2×10^{-9} Torr as sampled continuously by the residual gas analyzer. At such residual gas levels, the impingement rate of reactive gases onto the surface of the metal foil amounts to about one monolayer per hour; thus, negligible foil surface contamination results from the impurity gas background in the vacuum chamber. The oxygen in the original surface oxide layer will diffuse into the metal foil at such a high temperature, resulting in negligible oxygen contamination of the metal foil surface after high-temperature recrystallization. The metal foil (Zr or Ni) can be cooled to room temperature within a few seconds and a second layer of pure metal (Ni or Zr) is immediately sputtered onto this fresh foil without breaking the vacuum, creating a bilayer diffusion couple between one polycrystalline metal (denoted poly-Ni or poly-Zr) and another metal in the form of large single crystal mosaics (denoted s-Zr or s-Ni). A schematic of the resultant morphology of such a bilayered diffusion couple is shown in Fig. 1. It is to be noted that the concentration of defects in a single crystal mosaic such as the density of dislocations is drastically reduced by the high temperature heat treatment; the subsequent reaction may be influenced as a result.

Specimens were examined both in plane-view and in cross-section with a Philips EM 430 transmission electron microscope operated at 300 kV. Cross-sectional specimens of sputtered Ni/Zr multilayers were made from multilayers sputter deposited onto oxidized silicon wafers. After deposition and heat treatment, the silicon wafer together with the deposited multilayer was cut by a diamond scribe to squares approximately $3mm \times 3mm$. Two such squares were bonded together with the multilayers face to face by epoxy (M-Bond 610 Adhesive, Vishay Intertechnology Inc.). Cross-sectional specimens of bilayered polycrystal/single crystal diffu-

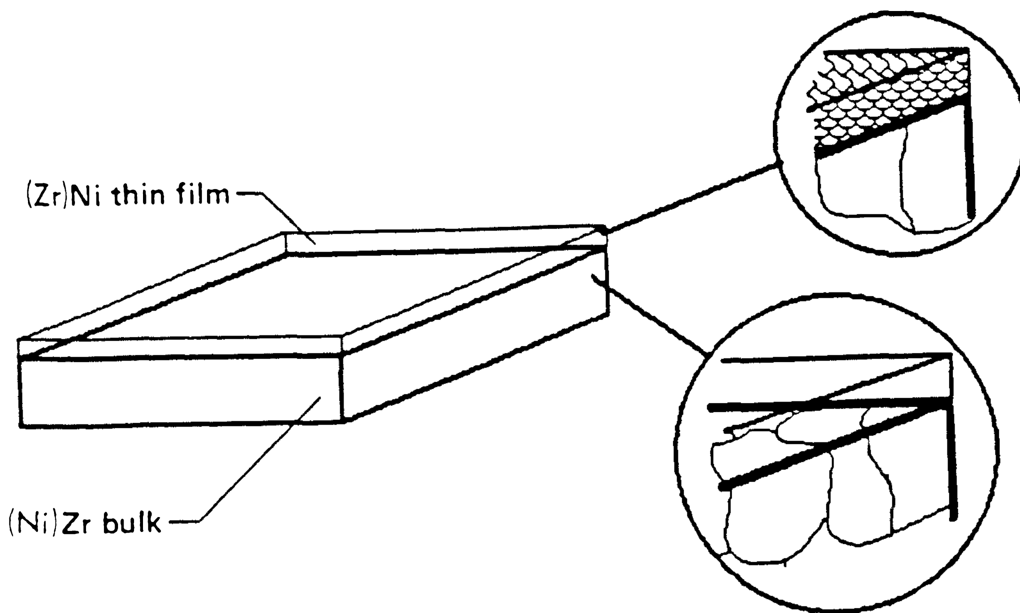

Fig. 4.1 Schematic of the morphology of bilayered elemental Ni/Zr diffusion couples where one element (Ni or Zr) is sputtered polycrystals and the other (Zr or Ni) consists of a mosaic of large single crystals on the order of 10 μm in size.

sion couples were prepared similarly. After deposition and heat treatment, the free standing metal foil was again cut to 3×3 mm squares, and two blank Si wafers (3×3 mm squares) were used to sandwich two such metal foils face to face for protection. Constant pressure is applied to such an assembly by a special clamping device during the epoxy curing. Curing of the epoxy takes about one to two hours at around 100°C. The curing temperature is low enough to avoid interdiffusion in the curing stage. After curing, the specimen is mounted vertically onto a flat platform by crystal bond and polished mechanically (600 grade SiCpaper) to a thickness around 100 μm. This mounting necessarily heats the specimen to the melting temperature of the crystal bond, which is greater than 100°C. The specimen temperature during such mounting is usually kept under 150°C, and brief heating to this temperature does not induce great change in the sample. In certain cases, a limited amount of interdiffusion is observed at the original interface of the diffusion couple. The polished surface is then smoothed by a final polishing with 1 μm diamond paste. A 3 mm Cu ring is then glued onto the smoothed side of the specimen by fast-setting epoxy for integrity of the specimen and ease of handling. This specimen is then mechanically polished from the other side by a rotating wheel (the Dimpler, VCR Inc.) with 1 or 0.3 μm diamond pastes applied. The specimen is so polished to a thickness of less than 5 μm and finally ion-milled in the center region by Ar ion bombardment (ion mill, VCR Inc.) until it is electron-transparent. Typical pressure in the sample chamber during ion milling ranges between 1 to 8×10^{-5}Torr. Typical ion gun settings are 5kV and 1mA. The sample stage is usually cooled to liquid nitrogen temperature during ion milling. However, no significant differences between samples milled at liquid nitrogen temperature or at room temperature have been observed. Some multilayers were deposited onto NaCl substrates and can be examined directly in plane-view by floating the deposited multilayer off the

substrate in de-ionized water and capturing the foils on Cu TEM grid.

4.2 How Thick Can Amorphous Interlayers Grow?

In Chapter 3, the enthalpy of mixing of pure Ni and pure Zr upon formation of amorphous NiZr alloys of various concentrations has been directly measured. In the relevant composition range, the heat of mixing of the amorphous phase averages about 30 kJ/mole. A large thermodynamic driving force thus exists for the reaction

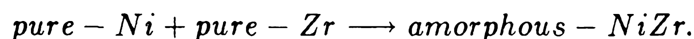

$$pure - Ni + pure - Zr \longrightarrow amorphous - NiZr.$$

The rate at which the amorphous NiZr alloy forms, however, diminishes with reaction time as "$t^{-1/2}$" since the amorphous interlayer growth is diffusion-controlled. It is thus appropriate to ask whether an amorphous interlayer, once formed, can grow to arbitrary thickness, given a sufficient supply of both elemental materials and sufficient time.

To answer this question, we have examined Ni/Zr diffusion couples heat-treated under various conditions by cross-sectional transmission electron microscopy (XTEM). Fig. 2 shows a XTEM bright-field micrograph of a sputter-deposited multilayered Ni/Zr diffusion couple. The specimen has not been subjected to heat treatment except during sample preparation, which amounts to a brief heat treatment around 150°C. The as-deposited microstructure of both the pure Ni and the pure Zr layers as well as the amorphous NiZr interlayers originating at each Ni/Zr interface, which formed as a result of heating during the sample preparation

Fig. 4.2 XTEM bright-field micrograph of a Ni/Zr multilayered thin-film annealed briefly around 150°C (see text).

process, are clearly evident. This multilayer consists of three Zr and two Ni layers, individual Zr and Ni layer thicknesses are 2500Å and 1700Å, respectively. The Zr layers are made up of columnar Zr grains around 200Å in diameter, and many of those grains extend across an entire whole Zr layer. The Ni layers are made up of a multitude of Ni grains that are not as uniform in size, but range typically from 200 to 500Å. The initially formed amorphous NiZr interlayers are about 50Å thick and are very uniform laterally, a point deserving further discussion later. From Fig. 2 we see that the first phase in such polycrystalline Ni/Zr diffusion couples is indeed the amorphous phase.

Fig. 3 shows a XTEM bright-field micrograph of a Ni/Zr multilayer from the same deposition annealed at 320°C for 8 hours. A section of the original sample is shown in the micrograph. In addition to the amorphous NiZr interlayers, which are now about 1000Å in thickness, one additional compound interlayer about 1000Å in thickness can be seen to have formed between every amorphous interlayer and its adjacent remaining Zr layer. Microdiffraction information from the compound layer shows that the compound is orthorombic equiatomic NiZr. Energy dispersive x- ray analysis (EDX) was performed. The standardless method for thin specimens[2] was used to calculate the atomic compositions from collected x-ray characteristic line intensities. EDX analysis on this cross-sectional specimen indicates that the average composition of the amorphous layers is about $Ni_{60}Zr_{40}$, whereas that of the compound layers is close to $Ni_{50}Zr_{50}$. Thus, the compound NiZr is the second phase during evolution of polycrystalline Ni/Zr diffusion couples, which succeeds the amorphous phase.

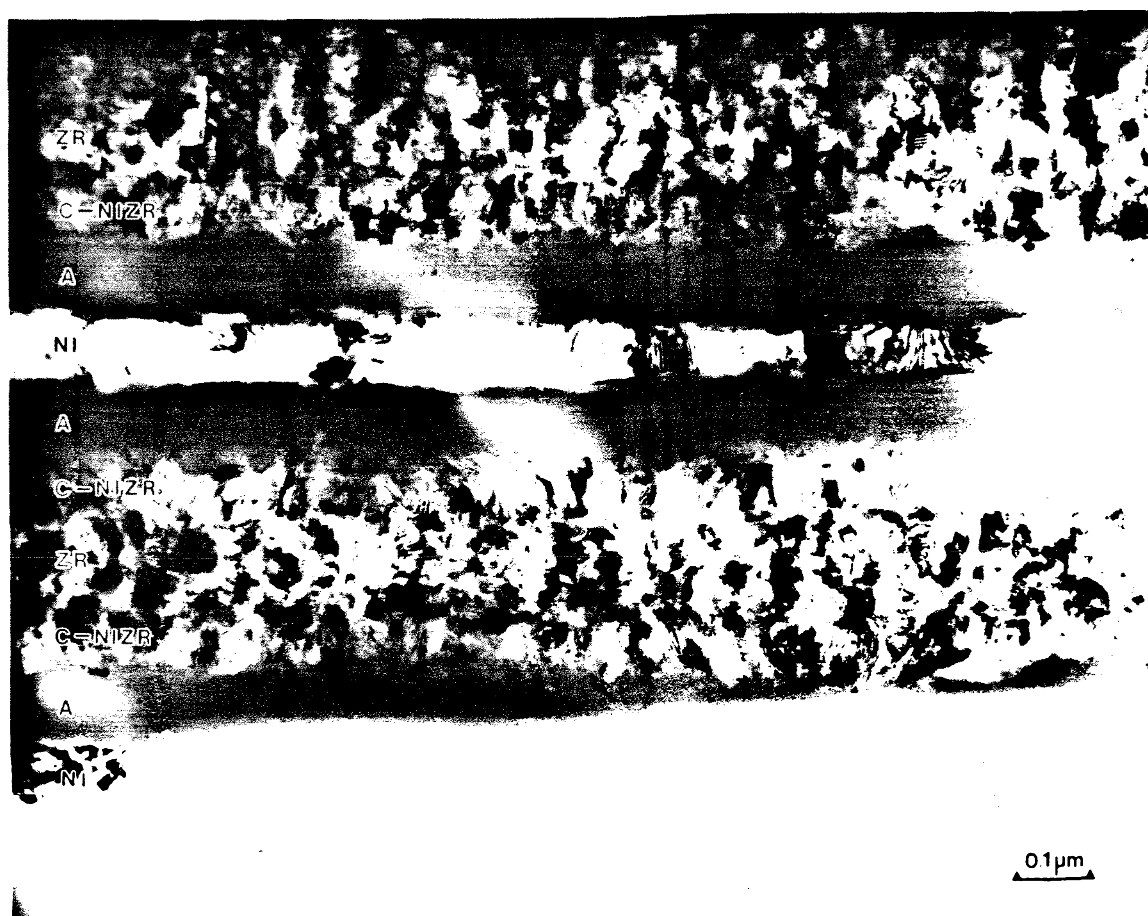

Fig. 4.3 XTEM bright-field micrograph of a Ni/Zr multilayered thin-film annealed at 320°C for 8 hours. Both amorphous and compound interlayers are clearly evident. Amorphous interlayers are close to 1000Å in thickness.

It is of interest to know in more detail how this compound formed. One possible scenario would be that the amorphous interlayer actually grew to a thickness of about 2000Å and the compound subsequently crystallized from the already formed amorphous material. Fig. 4 shows two XTEM bright field micrographs of another Ni/Zr diffusion couple annealed at 300°C for 6 and 18 hours, respectively. At the end of 6 hours, the amorphous interlayer has grown to about 1000Å in thickness. Additional annealing to 18 hours resulted in the formation of the NiZr compound instead of further growth of the amorphous NiZr interlayer, in agreement with other measurements[3]. It is worth noting that, according to Fig. 4, the extent of back growth of the compound into the amorphous material already formed is very little at 300°C; this has been commonly observed in many areas of the specimen. Thus, the hypothesis that the compound interlayer formed by crystallization of the already formed amorphous interlayer is invalidated by these results. Fig. 5 shows two XTEM bright-field micrographs of a Ni/Zr diffusion couple reacted at 360°C for 10 and 45 minutes, respectively. The amorphous NiZr interlayer grew to a thickness of about 850Å in 10 minutes. Further annealing to 45 minutes resulted in the formation of the compound NiZr, starting at the amorphous NiZr/Zr interface, and the compound grew backward at the expense of the amorphous material, in contrast to the result shown in Fig. 4 obtained for heat treatment at 300°C. It should be noted that in this case the backward growth of the compound into the already formed amorphous material is much faster than the forward growth of the compound into the pure Zr.

The following scenario is suggested based upon the above observations. The compound NiZr forms at the moving amorphous NiZr/Zr interface after

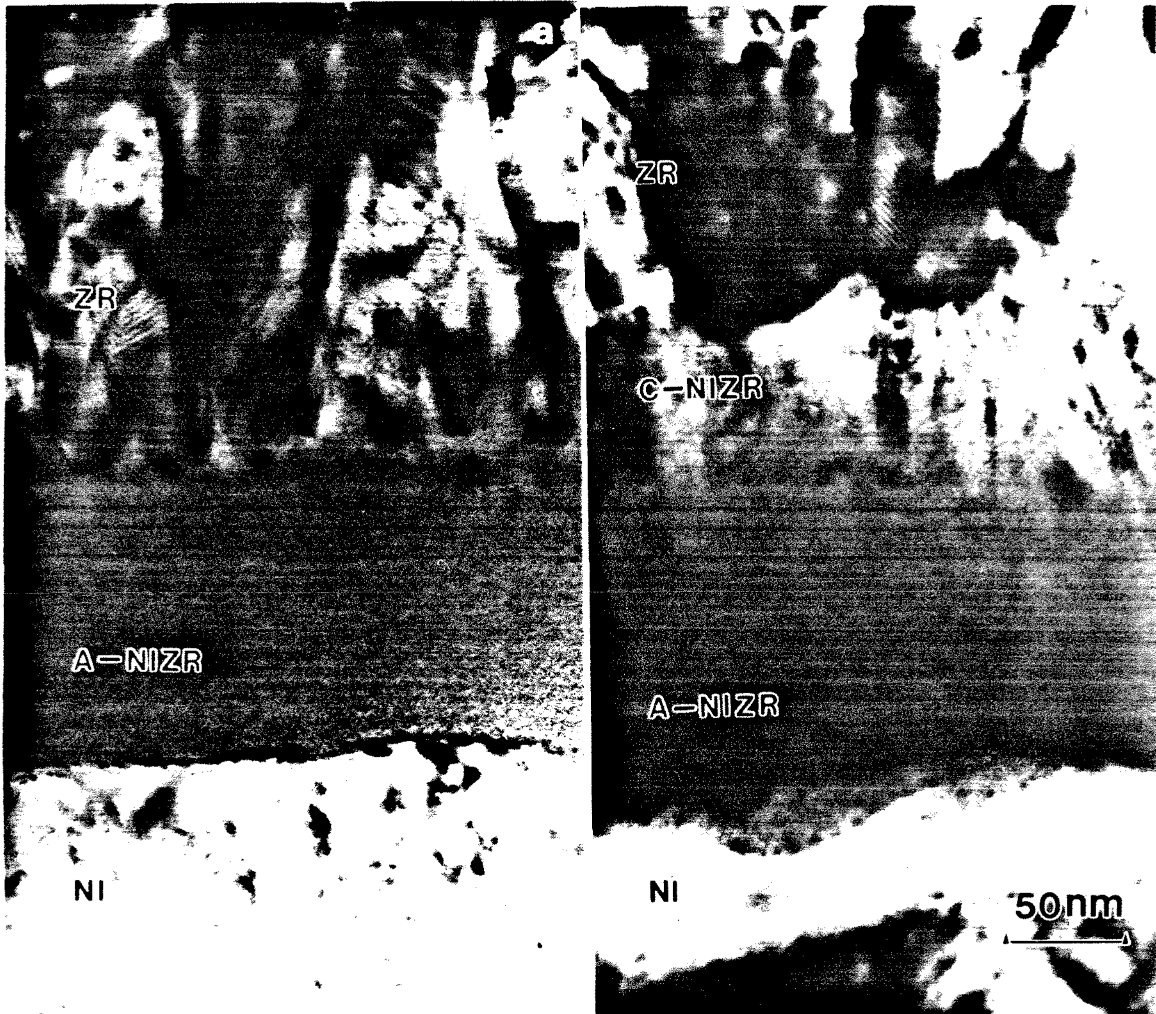

Fig. 4.4 XTEM of a Ni/Zr diffusion couple reacted at 300°C: (a) for 6 hours; (b) for 18 hours. This diffusion couple is of the bilayered s-Ni/poly-Zr type (see Section 4.3).

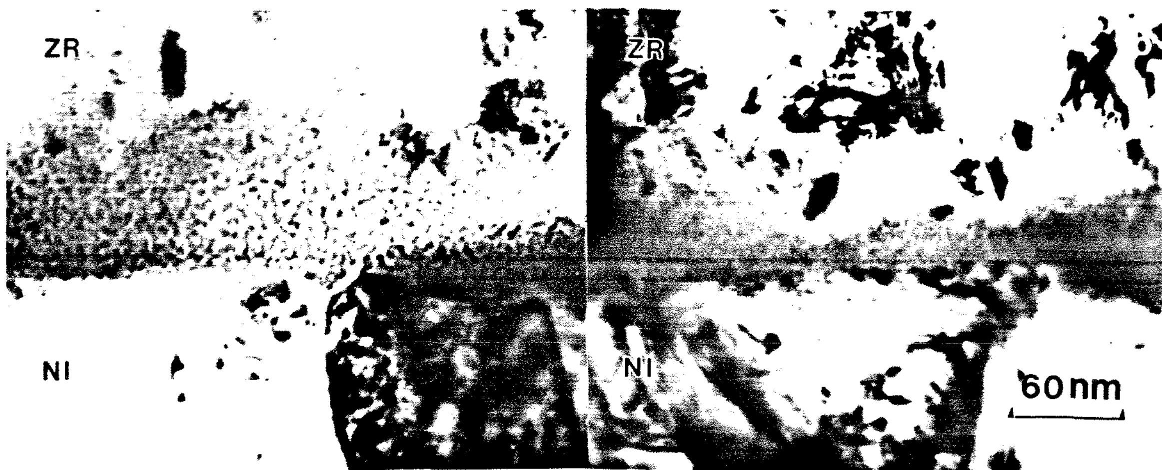

Fig. 4.5 XTEM bright-field micrographs of a sputtered Ni/Zr multilayered thin-film annealed at 360°C: (a) for 10 min; (b) for 45 min. Backgrowth of the compound into the amorphous material at 45 min is clearly evident.

the amorphous interlayer reaches a certain thickness. Formation of this compound creates two additional interfaces, namely, the compound/amorphous interface and the compound/Zr interface. The compound/amorphous interface is relatively immobile at low temperatures ($< 320°C$) but mobile at high temperatures ($> 360°C$). The composition of the amorphous NiZr alloy at the the original amorphous/Zr interface is close to $Ni_{50}Zr_{50}$ as determined by previous RBS measurement[4], also in agreement with our EDX analysis. The local situation at the amorphous/compound interface is thus rather analogous to that found during polymorphic crystallization of an amorphous $Ni_{50}Zr_{50}$ alloy to the orthorombic NiZr compound[5]. The fact that the amorphous/compound interface goes from being relatively immobile to mobile in a temperature interval of 40 to 60 degrees signifies a rather high activation energy for moving this interface, in agreement with previous crystallization studies, which showed an activation energy around 2.5 eV for crystallization of amorphous $Ni_{50}Zr_{50}$ alloy[6]. The compound/Zr interface is mobile even at 300°C, but its motion is limited by the diffusional transport of Ni through the amorphous interlayer plus the compound interlayer and can thus be rather slow. Since the compound NiZr is lower in free energy than the amorphous NiZr alloy, the amorphous/compound interface can not move into the compound phase. The growth of the amorphous NiZr interlayer is limited by the formation of the compound NiZr. Once the compound NiZr forms at the amorphous/Zr interface, the growth of the amorphous interlayer will cease. Thus, a maximum thickness exists for growth of the amorphous NiZr interlayer. This would not be the case if the second compound phase formed instead at the Ni/amorphous interface; it would then be possible for the amorphous interlayer to grow simultaneously with the compound phase by growing into the pure Zr layer.

We have measured the maximum thickness of amorphous NiZr interlayers as a function of isothermal annealing temperature by direct cross-sectional observation; the result is displayed in Fig. 6 in an Arrhenius form. The temperature dependence of this maximum thickness is quite weak, the apparent activation energy of which is only 0.1 eV by linear regression of the observed data. The maximum thickness an amorphous NiZr interlayer can grow is about 1000Å.

4.3 Is Nucleation Important?

In sputter-deposited polycrystalline Ni/Zr diffusion couples, the observation of lateral uniformness of the amorphous NiZr interlayer during its early stage of growth is important (see Fig. 2). Formation of the amorphous phase requires nucleation. The fact that an amorphous interlayer around 50Å in thickness is laterally uniform suggests that nucleation centers for the amorphous phase exist in abundance at the original Ni/Zr interface, since islandlike amorphous clusters would probably be found in the early growth stage if very few nucleation centers were present. It is natural to connect such observations to the well-known Walser and Bene conjecture, which effectively states that a glass interlayer always exists first in an elemental diffusion couple prior to the appearance of any intermetallic compound, which can essentially be viewed as the crystallization product of this glass interlayer[7]. This glass interlayer can be a result of either the particular vapor deposition process or the interdiffusion at very small distances. Our observations on sputtered polycrystalline Ni/Zr diffusion couples seem to support such a conjecture.

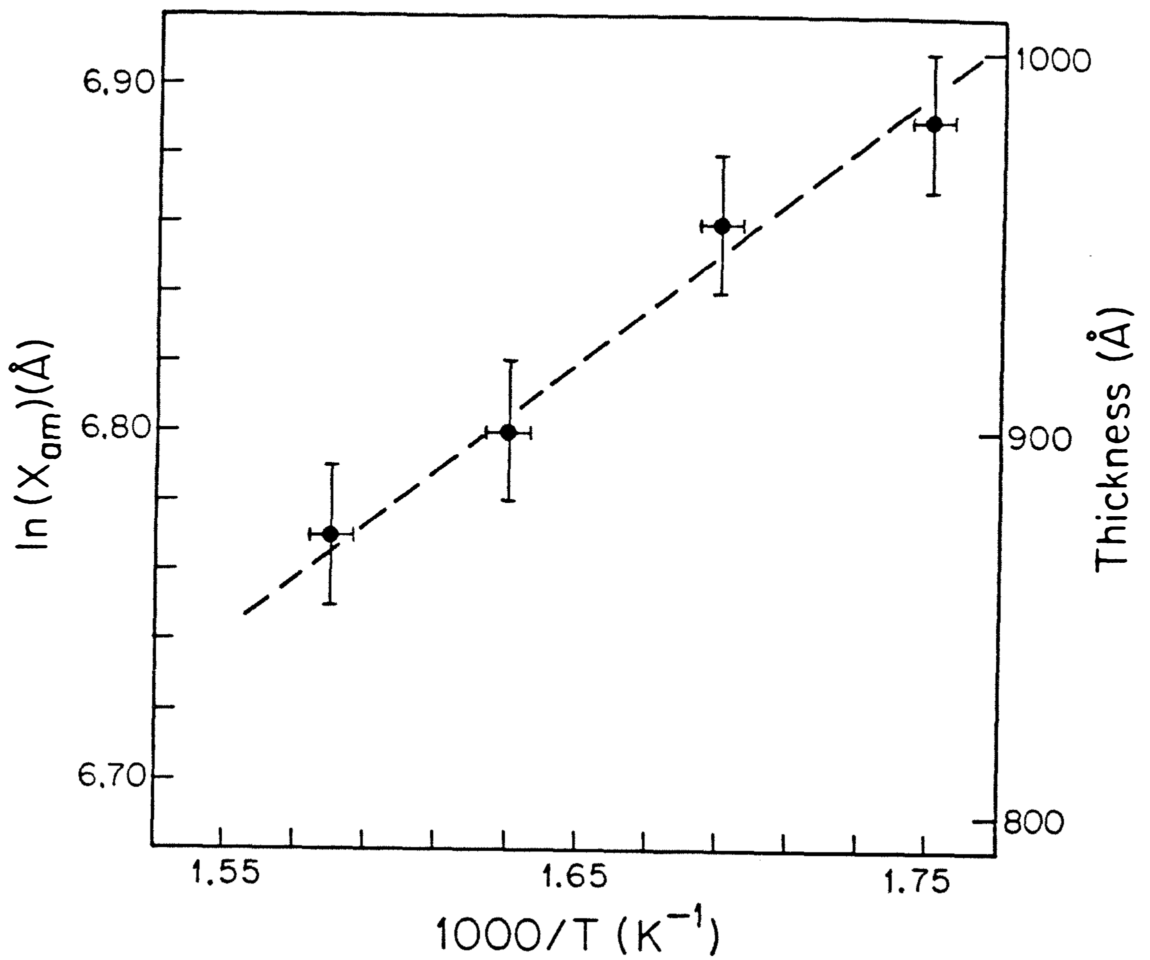

Fig. 4.6 Plot of the critical thickness of the amorphous NiZr interlayer vs. reaction temperature.

The present experiment aims at clarifying whether an interfacial glass interlayer is always present by creating interfaces of polycrystalline Ni with single crystal Zr or vice versa and by observing the evolution of such interfaces under heat treatment. Fig. 7(a) shows a XTEM bright field micrograph of Zr foil recrystallized at about 800°C. Resulting individual Zr grains are as thick as the foil with grain boundaries running through the entire foil. Little additional grain growth results from further heating beyond this point. The recrystallized Zr foil has a strong (002) texture with the c-axis perpendicular to the foil, the same as the sputtered polycrystalline Zr. A diffusion couple between sputtered polycrystalline Ni and recrystallized Zr foil is fabricated as described in Section 4.1. Shown in Fig. 7(b) is a XTEM bright-field micrograph of such a diffusion couple annealed at 300°C for 6 hours. Although reaction at this temperature for the above duration would have produced a fairly thick amorphous NiZr interlayer in polycrystalline sputtered diffusion couples, it is evident from this micrograph that no reaction is initiated at this interface between polycrystalline Ni (poly-Ni) and single crystalline Zr (s-Zr). A more detailed examination is shown in Fig. 7(c), which shows a high-resolution lattice image XTEM micrograph of the poly-Ni/s-Zr interface of a similarly reacted specimen. The specimen was tilted so that the poly-Ni/s-Zr interface was parallel to the electron beam direction. Lattice fringes of pure Ni and pure Zr extend to and meet at this interface, showing that the interface was originally atomically sharp and remained sharp after prolonged heat treatment with no indication of other phases, amorphous or crystalline, present. The apparent inertness of such a Ni/Zr interface when single crystal Zr is used is in agreement with previous RBS analysis on the same type of poly- Ni/s-Zr diffusion couples[8].

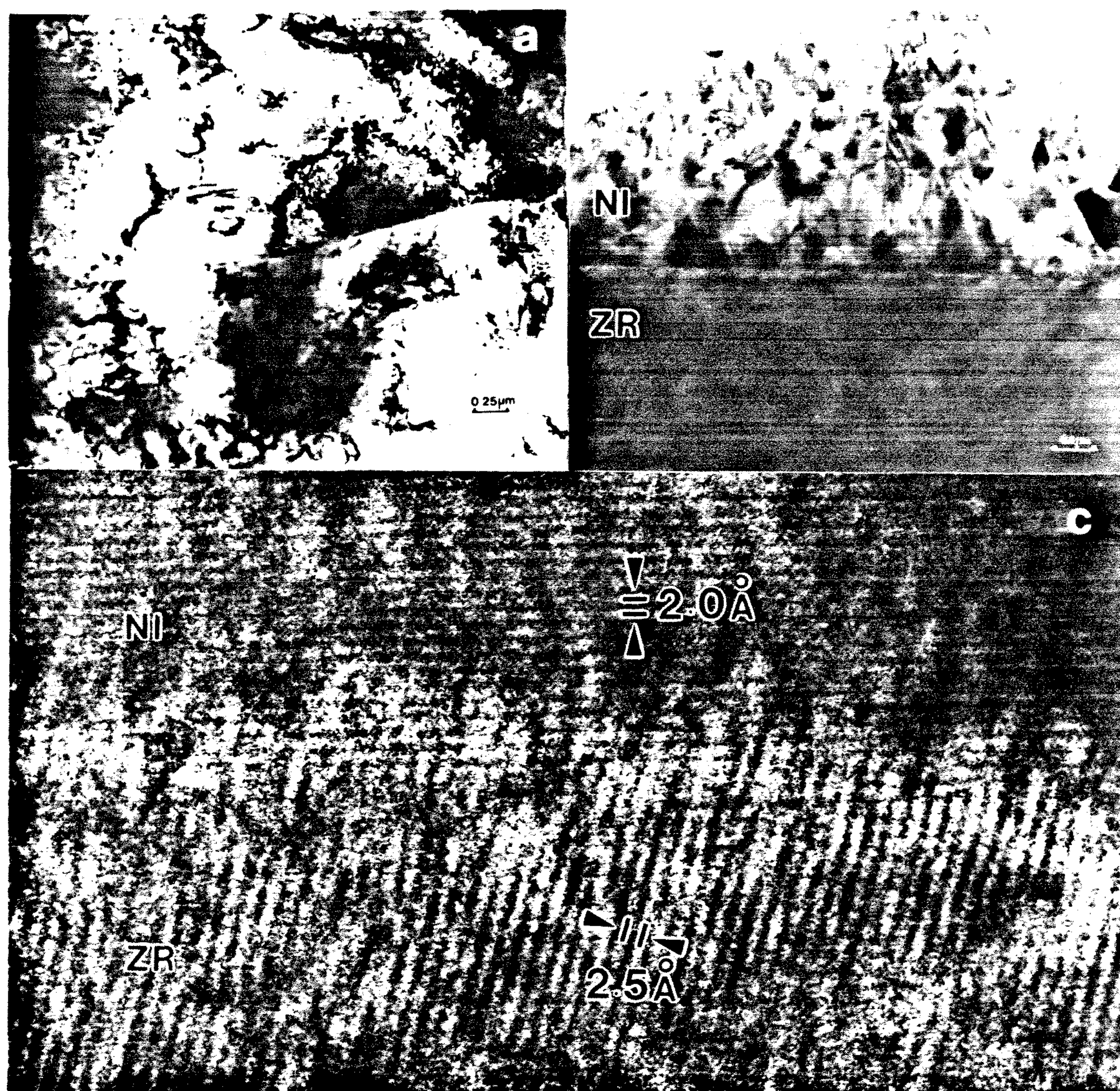

Fig. 4.7 Reaction of a poly-Ni/s-Zr bilayer diffusion couple: (a) typical microstructure of recrystallized Zr foil; (b) bright-field micrograph showing no reaction after annealing at 300°C for 6 hours; (c) high-resolution micrograph of the poly-Ni/s-Zr interface, showing the Ni (111) ande Zr (101) lattice fringes.

Our result indicates the existence of a nucleation barrier for amorphous phase formation when polycrystalline Ni is placed in contact with a Zr single crystal at 300°C. Thus, the formation of an amorphous NiZr alloy in sputtered polycrystalline Ni/Zr diffusion couples must be due to the presence of nucleation centers at the original poly-Ni/poly-Zr interface, which are absent when polycrystalline Zr is replaced by Zr single crystal. Grain boundaries are known to catalyze many precipitation reactions. The Zr grain boundaries may provide the neccessary nucleation centers for the amorphous phase. Since grain boundaries are indeed present in our recrystallized Zr foil, their influence on the formation of the amorphous phase is pursued. Fig. 8 shows in plane-view a bright-field micrograph of the same poly-Ni/s-Zr diffusion couple after annealing. One can see the Zr grains few microns to tens of microns in size as well as the few hundred angstrom Ni polycrystals on top of them. Some Ni grains are over one thousand angstroms in size because of grain growth during heat treatment. Electron diffraction revealed no sign of new phase formation. This micrograph shows that these remaining low-energy Zr grain boundaries do not catalyze the formation of the amorphous phase. To examine the influence of Ni grain boundaries at the Ni/Zr interface on the reaction process, we have similarly fabricated s-Ni/poly-Zr diffusion couples, where Ni consists of a mosaic of single crystals, again as described in Section 4.1. Fig. 9 shows a XTEM bright-field micrograph of a s-Ni/poly-Zr diffusion couple annealed at 300°C for 6 hours. No nucleation barrier seems to exist in this case and, as the result of this reaction, the amorphous NiZr interlayer has been grown to around 1000Å in thickness[9]. This shows that the absence of Ni grain boundaries at the Ni/Zr interface in such s-Ni/poly-Zr diffusion couples is immaterial for forming the amorphous phase.

Fig. 4.8 Plane-view, bright-field micrograph showing a poly-Ni/s-Zr diffusion couple after annealing at around 250°C for 4 hours. No reaction is observed at Zr grain boundaries.

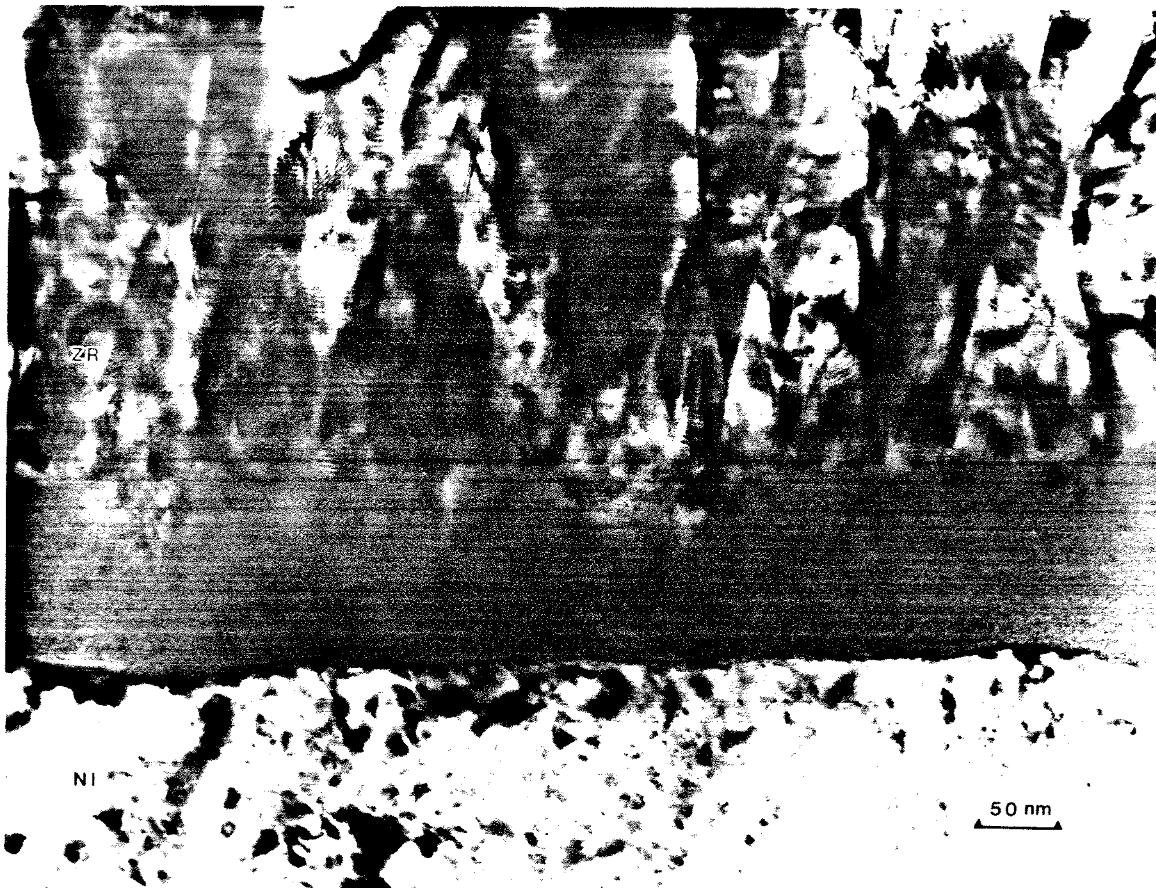

Fig. 4.9 XTEM bright-field micrograph of a s- Ni/poly-Zr bilayered diffusion couple annealed at 300° for 6 hours. An amorphous NiZr interlayer around 1000Å thick formed as a result of the reaction.

In addition, the behavior of such s-Ni/poly-Zr diffusion couples should also be contrasted with that of sputter-deposited polycrystalline Ni/Zr diffusion couples. Ni has been shown to be the dominant moving species during amorphization of Ni/Zr diffusion couples[10]. The predominant movement of Ni atoms across the Ni/amorphous interface into the amorphous interlayer is expected to generate excess vacancies on the Ni side of the Ni/amorphous interface. These vacancies may condense and form voids. We have observed large voids in the elemental Ni layers in sputter-deposited polycrystalline Ni/Zr diffusion couples after reaction (e.g., annealing at 320°C for 8 hours), in agreement with previously reported work[2]. One needs to keep in mind that existing voids may be enlarged by the ion milling process. However, the existence of voids exclusively on the Ni side confirms that Ni is the dominant moving species during interdiffusion of Ni and Zr. One notice that no void exists in the poly-Ni layer during the early stage of amorphous NiZr formation (see Fig. 2); thus, we speculate that void formation in the Ni layer by condensation of excess vacancies takes place only after a certain vacancy concentration level is reached. In Ni/Zr diffusion couples where Ni consists of a single crystal (see Fig. 9), no voids are observed anywhere in the Ni layer. We suggest that condensation of vacancies into voids in the Ni layer requires the presence of certain void nucleation sites. Apparently, Ni grain boundaries serve as such sites. With such sites absent when a single crystal of Ni is used, the vacancies diffuse into the Ni layer and eventually annihilate at the nearest sink. In our case of a bilayered s-Ni/poly-Zr diffusion couple, this nearest vacancy sink is apparently the Ni free surface. In addition, the same maximum thickness of amorphous NiZr interlayer was observed at 300°C, using either sputtered polycrystalline Ni/Zr multilayers or s-Ni/poly-Zr diffusion couple, suggesting that the presence of voids does not influence the formation of the compound NiZr in any significant way.

The phase formation behavior of Ni/Zr diffusion couples of the polycrystalline/single-crystalline type is essentially asymmetric, and we are led to believe that the formation of amorphous NiZr alloy in sputtered Ni/Zr diffusion couples is controlled by the presence of high-energy Zr grain boundaries that act as nucleation centers for the amorphous phase.

4.4 Models for Evolution of Diffusion Couples

The behavior of sequential phase formation in planar diffusion couples is experimentally demonstrated in the above sections for Ni/Zr diffusion couples. The first formation of an amorphous phase in this system indicates the need to include metastable phases in a complete description of diffusion couple evolution. Any theoretical attempt to describe the evolution of diffusion couples must face the problem of predicting the first phase, the critical thickness of the first phase prior to formation of the second phase, etc. Because of the complexity of the problem, experimental determination of a complete set of parameters that appear in any model is hard if not impossible. Thus, various phenomenological models are most often used to rationalize the general behavior of many systems instead of giving concrete predictions regarding any one system. In what follows, we will briefly present one model by Gosele and Tu, which rationalizes the phase sequencing in planar diffusion couples by focusing entirely on the relevant, one-dimensional growth kinetics[11]. We will also suggest a simple, phenomenological model that focuses on the nucleation kinetics[12]. Relevance of these models to experimental observations will be discussed.

The Gosele and Tu model sidesteps the question of nucleation by assuming that two compound interlayers β and γ exist at the beginning together with the two pure elements (saturated terminal solutions α and δ). The hypothetical concentration profile is shown in Fig. 10, and correspondence is easily made to the case of growth of a single compound interlayer, as shown in Section 3.2. Steady-state approximation is again used to simplify the problem so that analytical solutions are possible. One key assumption in this model is that the motion of every interface is assumed to be driven by diffusional fluxes into and out of this interface, and every interface is free to move in both directions depending on the relevant fluxes. A simple derivation completely parallel to the one given in Section 3.2 gives

$$\frac{dx_\beta}{dt} = G_\beta J_\beta^A - G_c J_\gamma^A \tag{1.1}$$

$$\frac{dx_\gamma}{dt} = G_\gamma J_\gamma^A - G_c J_\beta^A, \tag{1.2}$$

where J_β^A and J_γ^A are the A atom fluxes through the β and γ compound interlayers, given respectively by

$$J_\beta^A = \Delta C_\beta^{eq} \tilde{D}_\beta \frac{1}{x_\beta + \tilde{D}_\beta / \kappa_\beta^{eff}} \tag{2.1}$$

$$J_\gamma^A = \Delta C_\gamma^{eq} \tilde{D}_\gamma \frac{1}{x_\gamma + \tilde{D}_\gamma / \kappa_\gamma^{eff}}, \tag{2.2}$$

where the equilibrium concentration differences, interdiffusion constants and effective interfacial reaction barriers refer to those of the β or γ compound layers by their respective subscripts. The constants G_β, G_γ and G_c account for the change in concentration at the interfaces and they depend only on concentration of the respective compounds. Thus, the ratios of these constants, specifically $r_1 \equiv G_c/G_\beta$ and $r_2 \equiv G_\gamma/G_c$, are time-independent. It can be proved that $r_1 < r_2$. The ratio of A atom fluxes through the β and γ compound interlayers $r \equiv J_\beta^A / J_\gamma^A$ is, however,

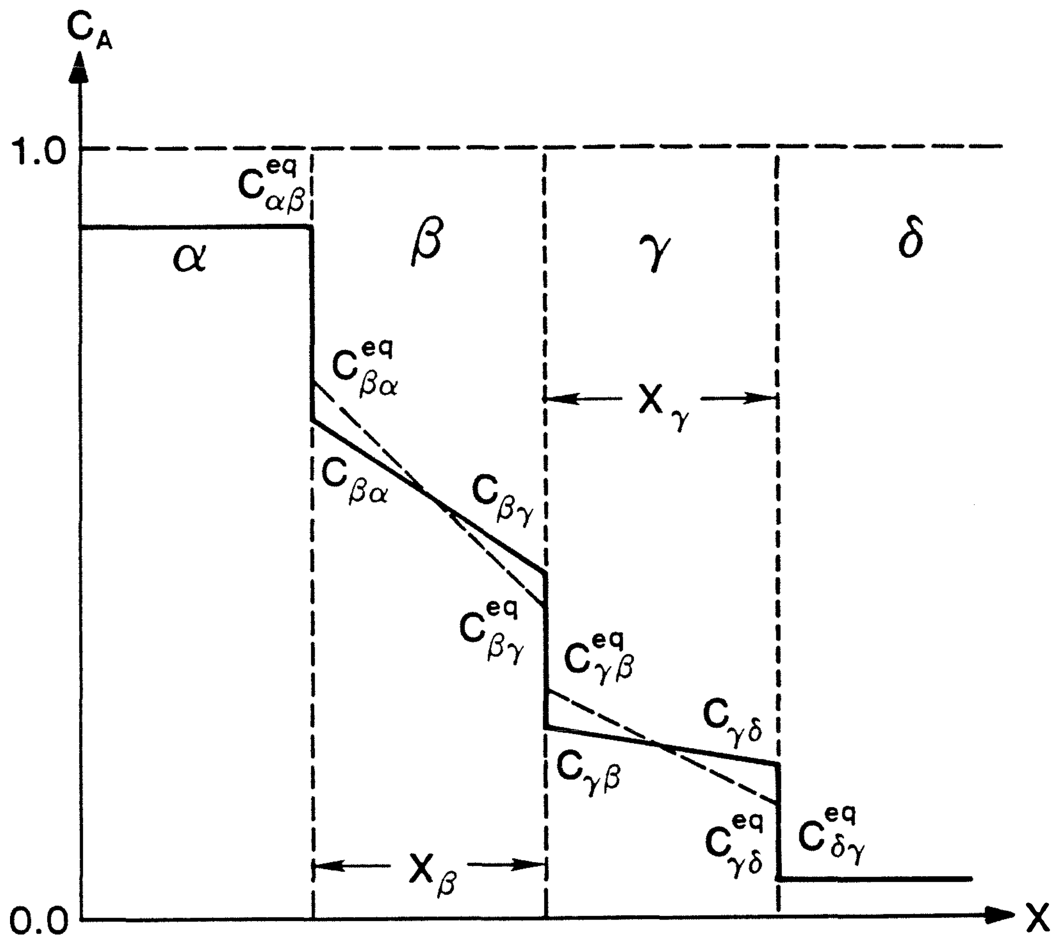

Fig. 4.10 Hypothetical concentration profile in a A-B diffusion couple during parallel growth of two compound interlayers β and γ (see text).

time-dependent. From Equation (1), we see the condition for the growth of β and γ is $r > r_1$ and $r < r_2$, respectively. A variety of growth behaviors can in principle be generated from this model, given suitable combination of parameters. Let us consider the following scenario. Let the two compound β and γ interlayers be very thin initially, such that transport across both layers are interface-controlled. This situation might simulate the very early stage of evolution of a binary diffusion couple when two compounds nucleated simultaneously. The flux ratio in this case can be obtained from Equation (2), $r = \Delta C_{\beta}^{eq} \kappa_{\beta}^{eff} / \Delta C_{\gamma}^{eq} \kappa_{\gamma}^{eff}$. If r falls in between r_1 and r_2, then both interlayers will grow. However, if the mobility of γ interfaces are much higher than that of the β interfaces such that $\kappa_{\gamma}^{eff} \gg \kappa_{\beta}^{eff}$, then the flux ratio will be less than r_1 and the γ interlayer will grow but the β interlayer will shrink. Thus, this model predicts that the first phase appearing in a binary diffusion couple is the one with the highest interface mobility. Eventually, the growth of the γ interlayer will become diffusion-controlled. In this case, the flux ratio will be given by $r = (\Delta C_{\beta}^{eq} \kappa_{\beta}^{eff} / \Delta C_{\gamma}^{eq} \tilde{D}_{\gamma}) x_{\gamma}$, and it will be dependent on the thickness of the γ interlayer. Suppose that r initially lies below r_1; then as the γ compound interlayer grows thicker, the flux ratio will increase and will eventually reach r_1, allowing the β compound to grow. The critical thickness of the γ compound in this model is thus given by $x_{\gamma}^{crit} = r_1 (\Delta C_{\gamma}^{eq} / \Delta C_{\beta}^{eq})(\tilde{D}_{\gamma} / \kappa_{\beta}^{eff})$. Thus, given suitable choice of parameters, this model is suggestive of some general features found during the evolution of many diffusion couples.

How pertinent is this model when applied to the particular case of Ni-Zr system which we have investigated experimentally in some detail? We have to qualify first that no experimental data for the interface mobility parameters exist

for either the amorphous or the compound phase. One may justify the first appearance of the amorphous NiZr alloy in sputtered Ni/Zr diffusion couples by assuming a higher interface mobility for the amorphous phase than for the compound, since it may be argued that less topological arrangement at the interface is required to form the amorphous phase than the compound. However, this hardly explains the observed asymmetric phase formation behavior when single crystals of either Ni or Zr are placed in contact with the other element, which is polycrytalline (see Section 4.2). Since a higher interface mobility for the amorphous phase, according to this model, would seem to predict that the amorphous phase would form first in both cases regardless of which side is a single crystal. Thus, the sensitivity of phase formation to the initial state of the interface as indicated by our experiments seems to suggest the need for considering nucleation kinetics in addition to growth kinetics. Furthermore, our observation that, at 360°C, the compound NiZr forms at the amorphous/Zr interface after the amorphous NiZr interlayer grows to a certain thickness and then grows back at the expense of the amorphous material, provides strong evidence that the formation of the compound NiZr is rate-limited by nucleation. With a mobile compound/amorphous interface, it would be impossible for the amorphous interlayer to grow to any thickness if the compound were to exist at the initial interface. Therefore, we believe that our experiments suggest that, at least in the Ni-Zr system, the kinetics of nucleation has to be considered in order to understand the formation of both the first and the second phase. In what follows, we present a simple phenomenological model based on the premise of interfacial heterogeneous nucleation, and we show how the evolution of Ni/Zr diffusion couples can be understood in this context[12].

Growth of an amorphous NiZr phase in Ni/Zr diffusion couples occurs at rather low temperatures ($\sim 300^\circ$C). The collective atomic rearrangements required for crystallization within the already formed amorphous interlayer do not occur until much higher temperatures are reached. The transition from growth of an amorphous phase to a compound phase occurs *heterogeneously* at the moving amorphous/Zr interface, as suggested by experiments outlined in the previous sections. Formation of any Ni-Zr compound phase at the amorphous/Zr interface requires formation of a heterogeneous nucleus. Assuming this to be the rate-limiting step in compound formation, we can analyze this transition from the growth of an amorphous phase to a compound. Since the growth of the amorphous interlayer is one- dimensional, the relevant dimension of this compound critical nucleus is its thickness in the growth direction, denoted by L. Denote further the velocity of the amorphous/Zr interface during growth of the amorphous interlayer as v_{int}. These parameters define a natural time scale τ_{int} required for the necessary atomic rearrangements taking place at the amorphous/Zr interface to form a Ni-Zr compound nucleus

$$\tau_{int} = \frac{L}{v_{int}}. \quad (3)$$

In time τ_{int}, the amorphous interlayer would advance a distance of L, leaving behind the interface an immobile glassy atomic comfiguration. The competing time scale τ_{nuc} for nucleating the Ni-Zr compound at the amorphous/Zr interface can be taken as the inverse of the heterogeneous nucleation rate I. According to the classical steady-state nucleation theory, this nucleation rate I is given by

$$I = K\nu exp(-\frac{\Delta G^* + Q}{k_B T}), \quad (4)$$

where K is a dimensionless constant, ν is an attempt frequency, Q is an activation energy for atomic transport in the interface region, and ΔG^* is the heterogeneous

nucleation barrier[13]. The condition for the continued growth of the amorphous interlayer can be stated simply as an inequality between these two time scales

$$\tau_{int} \leq \tau_{nuc}, \tag{5}$$

where the equality denotes the critical condition when the formation of the particular compound becomes possible. Equation (5) dictates a lower critical amorphous/Zr interface velocity L/τ_{nuc} below which the growth of the amorphous phase cannot be sustained against nucleation of the intermetallic compound. Equation (5) originates from general considerations of the two competing kinetics of amorphous phase growth and compound nucleation. Since the growth of the amorphous interlayer is diffusion-controlled, the amorphous/Zr interface velocity can be related to the thickness of the amorphous interlayer x_{am} by

$$v_{int} = K' \frac{\tilde{D}_{am}}{x_{am}}, \tag{6}$$

where K' is a dimensionless constant and $\tilde{D}_{am} = D_{\circ} exp(-Q'/k_B T)$ is the interdiffusivity through the amorphous interlayer. An explicit expression limiting the thickness of the growing amorphous interlayer can be reached in this case

$$x_{am} \leq (\frac{K' D_{\circ}}{LK\nu}) exp(\frac{(\Delta G^* + Q) - Q'}{k_B T}), \tag{7}$$

where the equality yields our prediction for the amorphous interlayer critical thickness X_{am}. It is to be emphasized that Equation (7) is obtained under the assumption that the diffusion constant is time-independent up to the transition between amorphous phase growth and compound nucleation.

4.5 Summary

We have monitored the formation of amorphous alloys and the subsequent formation of crystalline compound phases in planar thin-film diffusion couples by the technique of plane-view and cross-sectional transmission electron microscopy. Direct microstructural observations provided valuable detailed information that is not available from other techniques such as x-ray diffraction, backscattering spectrometry, or thermal analysis. These experimental observations suggest that, in addition to thermodynamic considerations, it is the combined nucleation and growth kinetics that determines the evolution of a thin-film diffusion couple.

4.6 References

1. R. W. Cahn, in *Physical Metallurgy*, edited by R. W. Cahn and P. Haasen, Ch. 25 (North-Holland Physics Publishing, Amsterdam, 1983).
2. L. Reimer, *Transmission Electron Microscopy*, Ch. 9 (Springer-Verlag, Berlin, 1984).
3. S. B. Newcomb, K. N. Tu, Appl. Phys. Lett. **48**, 1436 (1986).
4. J. C. Barbour, Phys. Rev. Lett. **55**, 2872 (1985).
5. U. Koster and U. Herold, in *Glassy Metals I*, edited by H. J. Guntherodt and H. Beck, Ch. 10 (Springer-Verlag, Berlin, 1981).
6. Z. Althounian, Tu Guo-hua, J. O. Strom-Olsen, J. Appl. Phys. **54**, 3111 (1983).
7. R. M. Walser, R. W. Bene, Appl. Phys. Lett. **28**, 624 (1976).
8. A. M. Vredenberg, J. F. M. Westendorp, F. W. Saris, N. M. van der Pers, Th. H. de Keijser, J. Mater. Res. **1**, 774 (1986).
9. K. Pampus, K. Samwer, J. Bottiger, Europhys. Lett. **3**, 581 (1987).
10. Y. T. Cheng, W. L. Johnson, M.-A. Nicolet, Appl. Phys. Lett. **47**, 800 (1985).
11. U. Gosele, K. N. Tu, J. Appl. Phys. **53**, 3252 (1982).
12. W. J. Meng, C. W. Nieh, W. L. Johnson, Appl. Phys. Lett. **51**, 1693 (1987).
13. J. W. Christian, *The Theory of Transformations in Metals and Alloys* (Pergamon Press, Oxford, 1975).

Conclusion

It has been almost five years since the publication of the first paper on solid-state amorphization reactions by Schwarz and Johnson. Since then, the synthesis of metastable materials, including amorphous materials, from the solid state has gained wide attention. We have concentrated our efforts on the experimental study of the solid state reaction processes in Ni-Zr thin-film diffusion couples in this thesis. It is our approach to obtain as much understanding as possible by attacking this problem from a variety of angles using a variety of experimental techniques. Among the issues to be investigated, the study of the growth kinetics of the amorphous interlayer is a relatively easy task and results obtained from various independent studies, including our own, are consistent. We have demonstrated that the dominant thermodynamic driving force for the amorphization reaction in Ni-Zr system arises from a large negative heat of mixing between the two elements. Our results are in agreement with other available thermodynamic data. Studies on both problems mentioned above are fairly complete at present and a general consensus exists on the conclusions derived. We have also demonstrated that the nucleation of the amorphous phase is sensitively dependent on the nature of the interfaces present. However, the study of nucleation of various phase, stable or metastable, at interphase interfaces, with or without heterogeneities such as grain boundaries or dislocations, of which our investigation serves as but one example, is only at its beginning. Well-designed experiments carried out with exquisite techniques are desperately needed in order to further our understanding on this subject.